Direct Numerical Simulation of Salt Fingering Gravity Currents and Double-Diffusive Rayleigh-Taylor Instabilities

by

Jared Penney

A thesis
presented to the University of Waterloo
in fulfillment of the
thesis requirement for the degree of
Doctor of Philosophy
in
Applied Mathematics

Waterloo, Ontario, Canada, 2017

I hereby declare that I am the sole author of this thesis. This is a true copy of the thesis, including any required final revisions, as accepted by my examiners.

I understand that my thesis may be made electronically available to the public.

Abstract

Double-diffusion refers to a class of instabilities that develops when the density of a fluid depends on two components with different diffusivities. For example, when warm, salty water is layered over cool, fresh water, there is relatively rapid diffusive transfer of heat from the upper layer to the lower layer, while there is negligible diffusive transfer of salt. This loss of heat results in localized parcels of fluid of increased density above the thermohaline interface, which sink out in the form of long, thin, convective cells called salt fingers. In parts of the ocean, salt fingers are known to be an important mechanism of heat and salt transport. However, they range from a few millimetres to centimetres wide, and are much smaller in scale than many oceanographic processes. The fine scale of these structures can also make their direct measurement in the environment using typical devices difficult. This thesis employs high-resolution direct numerical simulation for detailed examination of fine-scale double-diffusive features. An advantage of numerical simulation is the straightforward computation of quantities that cannot be measured directly through experiment, such as dissipation, stirring, and mixing. Two distinct types of flow are investigated. First, simulations of salt fingering gravity currents are examined, and the effect of different vertical boundary conditions and current volumes are analyzed. Second, a three-layer system resulting in double-diffusive Rayleigh-Taylor (RT) instabilities that transitions to double-diffusive turbulence in the absence of shear is presented. The flows are governed by the incompressible Navier-Stokes equations under the Boussinesq approximation, with salinity and temperature coupled to the equations of motion using a nonlinear approximation to the UNESCO equation of state. Flow dynamics are characterized using high-quality three-dimensional visualization techniques. In the gravity current simulations, it was observed that no-slip boundaries cause the current head to take the standard lobe-and-cleft shape, and encourage both a greater degree and an earlier onset of three-dimensionalization when compared to free-slip boundary cases. Additionally, numerical simulations with no-slip boundary conditions experience greater viscous dissipation, stirring, and mixing when compared to similar configurations using free-slip conditions. The Rayleigh-Taylor instabilities were observed to dominate the length scales of kinetic energy, while the length scales associated with the density field were dominated by double-diffusion. This was confirmed through spectral analysis, which also showed similarity between the dominant salinity and density scales. The standard eddy viscosity formulation was determined to be inappropriate for the salinity and temperature fluxes of this simulation. Due to the effects of double-diffusion, densities greater than the initial maximum value were observed in the RT instability simulations.

Acknowledgements

Dedication

To Rebekah.

Table of Contents

List of Tables

List of Figures

Chapter 1

Introduction

1.1 Double-Diffusion and Salt Fingers

Double-diffusion refers to a type of instability that is driven by a difference in active tracer diffusivities. As a result, the fluid may be stably-stratified in density, but unstably-stratified in one of its constituent tracers. A difference in tracer diffusivities can result in local density anomalies. For example, when salinity, the less diffusive tracer, and density are stably-stratified, but temperature, the more diffusive tracer, is unstably stratified (i.e., lighter, cool, fresh water above heavier, warm, salty water), if a small parcel of fluid from the lower layer is slightly perturbed upwards, it will lose heat to the fresh layer, while retaining its salinity. This causes the parcel to increase in density and sink back towards its initial state, resulting in an oscillation. This type of instability is often referred to as an oscillatory instability, or diffusive convection. In the opposite configuration, when a layer of lighter, hot, salty water rests over top of a layer of heavier, cool, fresh water, heat from the upper layer diffuses into the lower layer much more quickly than salt. As parcels of fluid just above the interface decrease in temperature, they increase in density, resulting in locally unstable density gradients. This causes the heavier, salty parcels to sink, forming long, thin convective cells called salt fingers. These fingers experience an additional lateral loss of heat to the fresh water, further increasing their density. This process is illustrated in Fig. 1.1. In the laboratory, salt fingers tend to be only millimetres wide, and are significantly longer in the vertical direction, with bulbs forming at their tips that spread into wider mushroom-like shapes, as shown in photographs presented in Fig. 1.2. These fingers were created by slowly pouring hot, salty water tagged with blue dye along a plastic dowel onto the surface of cool, fresh water to limit the lateral motion

1
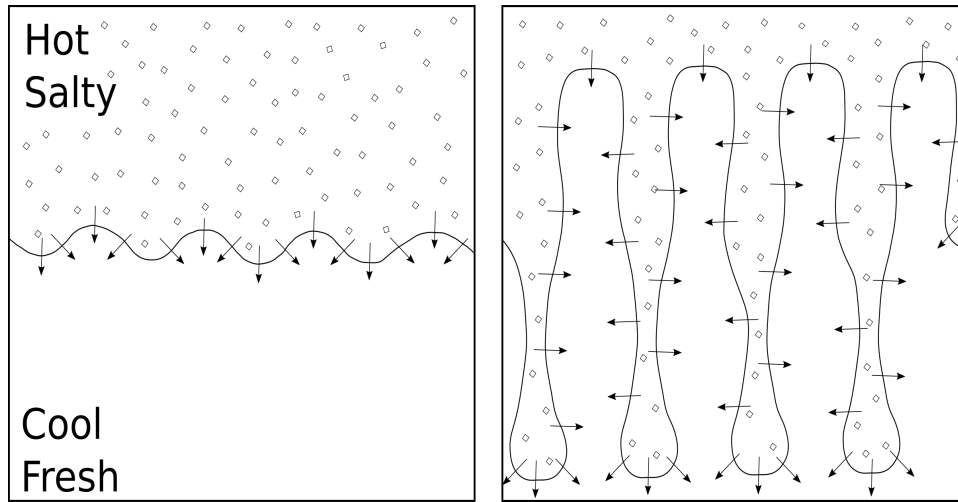
Figure 1.1: Diagram of (a) the initial stages of perturbation to the thermohaline interface and (b) the development of salt fingers at a later time. The arrows indicate the direction of heat and salt flux.

of the hot water and the number of fingers formed.

Double-diffusion was first reported by Jevons [37], who attempted to explain the mechanism behind the formation of cirrus clouds by creating finger instabilities using a heat-sugar system. Using a long-stemmed funnel, he introduced a layer of room temperature water below a layer of heated sugar water in a beaker, and observed the formation of "minute, thread–like streams." Though he briefly appears to elucidate the role of the difference in heat and sugar diffusivities as the mechanism behind the formation of these streams, he later asserts that the only function of the temperature difference is to allow the layering of heavier fluid over light when the two layers reach the same temperature, thereby missing the true nature of the mechanism behind double-diffusion. The historical context and an analysis of Jevons's discovery was provided by Schmitt [85], as well as an examination of the influence it had on subsequent work by Lord Rayleigh.

Double-diffusion is known to be an important mechanism governing heat and tracer transport for a number of different systems. Circulation and water masses in the ocean are thought to be strongly influenced by double-diffusion [83, 74]. Double-diffusion also appears in a variety of chemistry applications, such as thermosolutal convection for crystal growth [40] or at the interface between two dissolved reactants [117]. In astrophysics, there is a double-diffusive process involving heat and helium in stars known as semi-convection

2
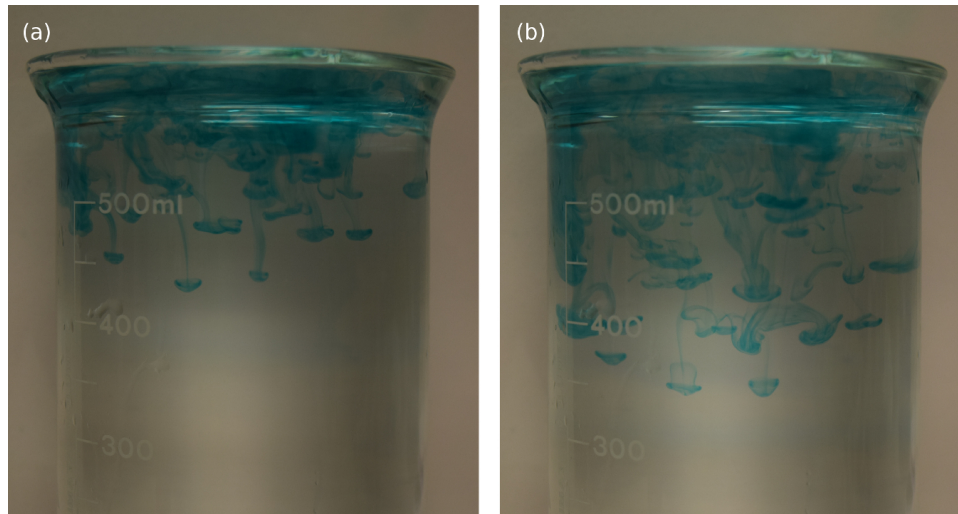
Figure 1.2: Photograph of (a) the early stages of salt fingers and (b) the same fingers, seconds later. Hot, salty water (in blue) is slowly introduced to the surface of the cool, fresh water by pouring it along a plastic rod.

[72].

1.2 Double-Diffusion in Nature

Observations of double-diffusive processes have been recorded throughout a number of regions of the Earth's oceans. Salt fingering has been observed at the Mediterranean Outflow [114, 115], in the Tyrrhenian Sea [115], in the Caribbean Sea [115], and in the Central Waters of the Eastern North Pacific [21]. Evidence suggests that salt fingers are responsible for the observed thermohaline stratification in the Central Waters, where the sun heats the surface of the water, causing both an increase in temperature and an increase in salinity due to evaporation [35, 86, 84].

Oceanic salinity and temperature profiles are often observed to decrease with depth in a step-like fashion. Numerous instances of these "thermohaline staircases" have been reported, such as in the Mediterranean outflow in the northeast Atlantic [98, 17], in the Canadian Basin in the Arctic Ocean [102], and in the tropical North Atlantic east of Barbados [87]. Staircase profiles are typically indicative of regions of salt fingering [87, 54].

3

Several mechanisms have been proposed for staircase formation [58]. Laboratory experiments [96] and numerical simulations [71] have shown that when smooth thermohaline profiles can result in fingering, this can give way to step-like profiles. It has been observed, however, that the steps in the temperature profiles may not be isothermal, but may in fact consist of long horizontal regions of temperature inversions made stable by the salinity stratification [54, 53]. These features are referred to as thermohaline intrusions, which typically develop when the vertical thermohaline distribution is favourable to the formation of salt fingers, but there are also lateral gradients of heat and salinity [95, 106, 75]. In alternating intrusions of warm, salty water and cool, fresh water, the interfaces display tendencies towards salt fingering or diffusive convection depending on the stratification at the interface [106]. A method of thermohaline staircase formation due to the evolution of thermohaline intrusions was proposed by Merryfield [58].

Double-diffusive properties have also been observed in various lakes. Thermohaline staircases have been detected in Lake Nyos [81], Lake Kivu [82], and Lake Vanda [29]. Meromictic lakes (i.e., lakes with layers that do not intermix) often display conditions favourable to diffusive convection [109]. The destabilizing temperature profile responsible for diffusive convection is often due to geothermal heating [34, 80].

The relatively low diffusivity of suspended particles presents the possibility of double-diffusive instabilities when involved in a system with heat or salt. Though quantitatively different, there are strong qualitative similarities between thermohaline double-diffusive flows and flows involving suspended sediment and another tracer. Houk and Green [31] present early experiments of suspension fingers, where a layer of warm, turbid water overlies cold, clear water. A later paper by Green [23] examined experiments of sediment fingering from a warm, turbid surface gravity current above cool, clear water. In nature, double-diffusive sedimentation may manifest as rivers eject sediment-laden (or turbid) fresh water into the clear, salty ocean [66, 67]. This double-diffusion has been proposed as a mechanism responsible for enhanced sedimentation near river mouths [13].

1.3 Double-Diffusion in Laboratory Experiments

As with many field investigations, measurements of double-diffusion in nature can often be cost-prohibitive and labor-intensive. Laboratory experiments have played an important role in elucidating various mechanisms involving double-diffusion. Turner is responsible for early experiments of two-layer heat-salt systems resulting in diffusive convection [103] and salt fingers [104]. A possible mechanism for the formation of thermohaline staircases due to salt fingering from linear vertical thermohaline gradients was proposed based on

experiments by Stern and Turner [96]. Experiments by Linden [50] were responsible for discovering the organization of salt fingers into sheet-like structures arranged in the direction of imposed shear. Other experimental studies have examined various phenomena, including intrusions [106, 78, 73], salt fingers under the influence of shear [112, 19], and measuring various buoyancy fluxes and eddy diffusivity parameterizations [57, 111, 110], among others.

For comparison of different flows, the relationships between the kinematic viscosity ν, the diffusivity of heat κ_T, and the diffusivity of salinity κ_s are parameterized by three dimensionless numbers: the Prandtl number, $Pr = \nu/\kappa_T$, the Schmidt number, $Sc = \nu/\kappa_s$, and the diffusivity ratio, $\tau = \kappa_s/\kappa_T$. In the ocean, these parameters typically take values of $Pr = 7$, $Sc = 700$, and $\tau = 0.01$. An advantage of laboratory experiments over numerical simulations is that they can achieve these physical diffusive scales without much difficulty. However, the use of heat-salt systems can be complicated by the loss of heat through uninsulated boundaries. As a result, salt-sugar systems are commonly used as substitutes [55, 96, 121, 78]. In salt-sugar systems, the dimensionless values are typically reported as $Pr = 1000$, $Sc = 3000$, and $\tau = 1/3$ [65], with the higher diffusivity tracer (salt) taking the place of heat. Stability analysis shows that for any two tracers with different diffusivities, if the higher diffusivity tracer is stably-stratified, and the lower diffusivity tracer is unstably-stratified, a fingering instability may form [105]. For example, to create sugar fingers, one would arrange stable density and salinity distributions, and an unstable sugar distribution. Though past results displayed qualitative similarities between salt-sugar and heat-salt double-diffusive experiments, there is a quantitative dependence on the values of the diffusivities [55].

1.4   Numerical Simulations of Double-Diffusion

Direct numerical simulation (DNS) allows for a more detailed analysis of flows that is not afforded by laboratory experiments. Laboratory tank experiments can be difficult to analyze visually, due to the typical limitation of viewing the tank from the outside. DNS can allow for detailed examination of interior flow features. Additionally, measured values of variables are not limited to the location and number of available measuring devices, and instead are distributed throughout the domain at each grid point. Numerical simulation also affords a greater degree of control on experimental parameters and initial conditions. However, certain concessions must be made depending on the scale and primary concerns of the simulations. Small-scale features require sufficiently fine grid spacings to ensure adequate resolution, which necessitates a large number of grid points. The resulting

Reference	Phenomenon Simulated	Pr	Sc	τ
Piacsek and Toomre [69]	salt fingers layer of hot, salty over cool fresh water	6.8	680	1/100
Piacsek et al. [70]	two- and three-layer systems to simulate intrusions	NR	NR	NR
Shen and Veronis [88]	salt fingers layer of hot, salty over cool fresh water	NR	NR	1/80
Özgökmen et al. [65]	fingering with initially linear stratification	100	3000	1/30
Özgökmen and Esenkov [64]	fingering in two-layer system with nonlinear equation of state	7	700	1/100
Radko [71]	layer formation due to fingering in initially linear stratification	7	21	1/3
Konopliv and Meiburg [45]	lock-exchange double-diffusive gravity currents	1	$1-8$	$1/8-1$

Table 1.1: Prandtl number, Schmidt number, and diffusivity ratio used in past two-dimensional numerical studies of double-diffusion. NR indicates that the values were not reported.

computational requirements limit the size of the domain that can be simulated and still capture these features. Larger computational domains may accurately capture the size of limnological or oceanographic domains of interest, however, the resulting resolution will not adequately capture subgrid-scale features, requiring these phenomena to be parameterized in some way. As such, it can be difficult to scale double-diffusive instabilities to larger domains. Since the length scale of salt fingers is set by molecular diffusion, salt fingers do not increase in size as the scale of the flow increases. Therefore, simulation of salt fingers on larger domains requires either a large number of grid points, which may not be computationally feasible, or some type of subgrid-scale parameterization.

The small length scales associated with double-diffusion are part of the reason for the difficulty involved in simulating double-diffusive instabilities. Simulation is also complicated by the need to resolve the different diffusive length scales of the tracers. Because the diffusivity of salinity is so small (typically on the order of $10^{-9}\,\mathrm{m^2/s}$ [18]), it can result in sharp interfaces that require a high number of grid points to be adequately resolved. In earlier numerical studies of double-diffusive instabilities, this typically meant limiting simulations to two-dimensions [69, 70, 88, 65, 64, 71]. Table 1.1 lists several two-dimensional numerical simulations of double-diffusive flows, and the corresponding Prandtl numbers, Schmidt numbers, and diffusivity ratios. However, with advances in computational power, salt fingers and other double-diffusive processes have been the subject of several high-resolution three-dimensional simulations in recent years (a summary of recent three-dimensional double-diffusive simulations is presented in Table 1.2). One approach to reduce the resulting memory constraints has been to use a finer grid for the salinity field than for the temperature and velocity fields [43, 11, 93, 92]. While three-dimensional simulations are currently typically capable of resolving physical thermal diffusion scales, as shown in Table 1.2, it is still difficult to resolve physical saline diffusivity scales using

Reference	Phenomenon Simulated	Pr	Sc	τ
Smyth et al. [93]	double-diffusive Kelvin-Helmholtz billows	7	50	0.14
Kimura and Smyth [43]	shear-induced salt sheets	7	$43.75 - 700$	$0.01 - 0.16$
Carpenter et al. [11]	double-diffusive interface	6.25	$18.94 - 625$	$0.01 - 0.33$
Kimura et al. [44]	double-diffusive shear layer (leading to salt sheets)	7	175	0.04
Smyth and Kimura [92]	double-diffusive shear layer (leading to Kelvin-Helmholtz billows)	7	175	0.04
Konopliv and Meiburg [45]	lock-exchange double-diffusive gravity currents	NR	NR	$1/8 - 1$

Table 1.2: Prandtl number, Schmidt number, and diffusivity ratio used in past three-dimensional numerical studies of double-diffusion. NR indicates that the values were not reported.

current computational resources. As a result, many DNS still use Schmidt numbers smaller than the reported value of the ocean. Though salt-sugar systems may facilitate laboratory experiments, the resultant diffusive scales are too small to accurately resolve numerically with current computational resources. Consequently, comparison between many laboratory experiments and numerical simulations will be primarily qualitative.

1.5 Objective and Outline

This thesis endeavors to examine fine-scale double-diffusive flows at high resolution using direct numerical simulation. Adequate resolution of the small-scale features and sharp diffusive interfaces requires a relatively large number of grid points. Due to current restraints on computational power, this necessitates the use of small computational domains. While other references [43, 11] present results that, due to simulation design, may be more readily applicable to oceanographic or limnological studies, the domains of the simulations presented here are on the scale of laboratory tanks. Since the scales of these flows are not much larger than the scales of the resulting instabilities, direct scaling to larger environmental currents would not be possible. Hence, the results presented here may be more readily applicable to experimental or small-scale industrial applications.

The focus of this research is the development of double-diffusive instabilities in two different types of flows initiated by buoyancy effects. The first set of simulations examines surface double-diffusive gravity currents resulting from density differences due to lateral salt and temperature gradients. The currents indirectly result in shear along the thermohaline interfaces. The second set of simulations examines primarily vertical flows due to unstable density gradients resulting in double-diffusive Rayleigh-Taylor instabilities. The remainder of this thesis is organized as follows: Chapter 2 details the numerical methods

used for simulations, as well as the mathematical techniques used in flow analysis. Chapter 3 discusses several simulations of double-diffusive gravity currents, and analyzes the effect of current volume and boundary conditions on flow structure. Chapter 4 examines a high resolution direct numerical simulation of double-diffusive Rayleigh-Taylor instabilities in order to characterize double-diffusive turbulence in the absence of imposed shear. In Chapter 5, the main results of the paper are summarized, and possible future work, including preliminary results of one concrete direction, is discussed.

Chapter 2

Methodology and Analysis Techniques

In this chapter, the equations of motion that govern the flows described in subsequent chapters are defined, and the DNS code used is briefly described. Relevant results of stability analysis are presented, and some of the techniques used for flow analysis and visualization are outlined.

2.1 Governing Equations and Numerical Methods

2.1.1 Governing Equations

The flows discussed here are governed by the incompressible Navier-Stokes equations subject to the Boussinesq approximation. The momentum equations are given by

$$\frac{\partial \boldsymbol{u}}{\partial t} + \boldsymbol{u} \cdot \boldsymbol{\nabla} \boldsymbol{u} = -\frac{1}{\rho_0} \boldsymbol{\nabla} p - g \frac{\rho}{\rho_0} \delta_{i3} + \nu \nabla^2 \boldsymbol{u}, \tag{2.1}$$

while conservation of mass is expressed as

$$\boldsymbol{\nabla} \cdot \boldsymbol{u} = 0, \tag{2.2}$$

where $\boldsymbol{u} = (u, v, w)$ is the velocity in the x-, y-, and z-directions, respectively, p is the pressure, $g = 9.81 \, \text{m/s}^2$ is the gravitational acceleration constant, $\rho_0 = 1000 \, \text{kg/m}^3$ is the

9

reference value for density, and $\nu = 2 \times 10^{-6}\,\mathrm{m^2/s}$ is the kinematic viscosity, which is assumed constant for these simulations. δ_{i3} is the Kronecker delta, which indicates in this case that buoyancy acts only in the vertical direction. The density ρ is defined by the nonlinear approximation to the UNESCO equation of state in terms of temperature T (in °C) and salinity s (in practical salinity units, or psu), as determined by Brydon et al. [8],

$$\rho\left(T, s\right) - \rho_0 = c_1 + c_2 T + c_3 s + c_4 T^2 + c_5 s T + c_6 T^3 + c_7 s T^2, \tag{2.3}$$

the coefficients of which are presented in Table 2.1. Equation (2.3) couples the Navier-Stokes equations to the equations of conservation for temperature and salinity,

$$\frac{\partial T}{\partial t} + \boldsymbol{u} \cdot \boldsymbol{\nabla} T = \kappa_T \nabla^2 T, \tag{2.4}$$

and

$$\frac{\partial s}{\partial t} + \boldsymbol{u} \cdot \boldsymbol{\nabla} s = \kappa_s \nabla^2 s, \tag{2.5}$$

where κ_T is the thermal diffusion coefficient, and $\kappa_s = 2 \times 10^{-8}\,\mathrm{m^2/s}$ is the salinity diffusion coefficient, which are set to $3.4 \times 10^{-7}\,\mathrm{m^2/s}$ and $\kappa_s = 2 \times 10^{-8}\,\mathrm{m^2/s}$, respectively.

2.1.2 Numerical Methods

Simulations were computed using the Spectral Parallel Incompressible Navier-Stokes Solver (SPINS) model [97], which performs DNS of the incompressible Navier-Stokes equations. Pseudospectral methods are used to calculate spatial derivatives, while time-stepping is done using a variable step third-order Adams-Bashforth method. Sine/cosine transforms and the Chebyshev method are used to calculate spatial derivatives in directions with free-slip and no-slip boundaries, respectively. The fastest growing mode of instability is excited by adding a small perturbation of white noise to the temperature field.

c_1	-9.20601×10^{-2}	$\mathrm{kg/m^3}$
c_2	5.10768×10^{-2}	$\mathrm{°C^{-1}\,kg/m^3}$
c_3	8.05999×10^{-1}	$\mathrm{psu^{-1}\,kg/m^3}$
c_4	-7.40849×10^{-3}	$\mathrm{°C^{-2}\,kg/m^3}$
c_5	-3.01036×10^{-3}	$\mathrm{°C^{-1}psu^{-1}\,kg/m^3}$
c_6	3.32267×10^{-5}	$\mathrm{°C^{-3}\,kg/m^3}$
c_7	3.21931×10^{-5}	$\mathrm{°C^{-2}psu^{-1}\,kg/m^3}$

Table 2.1: Coefficients of the nonlinear equation of state (2.3).

2.1.3 Linearization of the Equation of State

It is common practice in many simulations of double-diffusion (e.g.,[93, 43, 11]) to use an equation of state that is linear in both temperature and salinity,

$$\rho = \rho_0 \left(1 - \alpha(T - T_0) + \beta(s - s_0)\right), \tag{2.6}$$

with reference values of density, temperature, and salinity of ρ_0, T_0, and s_0. α and β are the coefficients of thermal expansion and haline contraction, respectively, defined as

$$\alpha = -\frac{1}{\rho}\frac{\partial \rho}{\partial T}, \tag{2.7}$$

and

$$\beta = \frac{1}{\rho}\frac{\partial \rho}{\partial s}. \tag{2.8}$$

For equation (2.3), this gives

$$\alpha = -\frac{1}{\rho}(c_2 + 2c_4 T + c_5 s + 3c_6 T^2 + 2c_7 sT), \tag{2.9}$$

and

$$\beta = \frac{1}{\rho}(c_3 + c_5 T + c_7 T^2). \tag{2.10}$$

Equation (2.6) is equivalent to expanding a general equation for ρ as a Taylor series about some reference temperature and salinity (T_0, s_0),

$$\rho(T, s) = \rho(T_0, s_0) + \left[\rho_T(T_0, s_0)(T - T_0) + \rho_s(T_0, s_0)(s - s_0)\right]$$
$$+ \frac{1}{2}\left[\rho_{TT}(T_0, s_0)(T - T_0)^2 + 2\rho_{Ts}(T_0, s_0)(T - T_0)(s - s_0) + \rho_{ss}(T_0, s_0)(s - s_0)^2\right] + \dots, \tag{2.11}$$

and truncating at the first-order terms,

$$\rho_{\text{lin}}^{(T_0, s_0)}(T, s) = \rho(T_0, s_0) + \rho_T(T_0, s_0)(T - T_0) + \rho_s(T_0, s_0)(s - s_0). \tag{2.12}$$

Though the linear equation of state is convenient for comparison with results of linear stability analysis, the formulation does have some issues regarding temperature. First, density does not decrease monotonically with temperature. In fact, the density of fresh liquid water is a maximum at 3.98°C [24]. As ice melts at 0°C, it gains enough thermal energy to

11

begin breaking the hydrogen bonds that are responsible for the molecular separation that causes solid water to be less dense than liquid water. The breaking of the hydrogen bonds allows for closer packing in its liquid form above 0°C, which increases the density until its maximum at 3.98°C. Above this temperature, the thermal motion dominates, causing greater separation of the water molecules, and thus lowering the density with temperature. Linear equations of state are incapable of representing the non-monotonicity and the density maximum. Second, Özgökmen and Esenkov [64] determined that for an equation of state that is quadratic in temperature and linear in salinity, the nonlinearity of the temperature term causes a greater buoyancy force to be applied to the downward-moving fingers when compared to the upward-moving fingers. This results in the faster growth of the descending fingers. It was also observed that while a linear equation of state causes symmetric development of upward and downward-moving fingers, increasing the strength of the nonlinearity coefficient decreases the width of the descending fingers relative to the ascending fingers.

In the thermohaline regime examined of the simulations presented here ($15°C \leq T \leq 40°C$, $0 \leq s \leq 5\,\text{psu}$), the density maximum is not a concern. However, a linear equation of state would inaccurately reflect the effect of temperature. The behaviour of the linearization varies significantly depending on the state around which ρ is linearized. For example, in these simulations, the initial stratifications along which salt fingering occurs are expressed by hyperbolic tangent functions, resulting in a two-layer system,

$$T\left(\boldsymbol{x}, t = 0\right) = T_0 + \frac{\Delta T}{2}\left(1 + \tanh\left(\frac{z_0 - z}{\Delta z}\right)\right), \tag{2.13}$$

$$s\left(\boldsymbol{x}, t = 0\right) = \frac{\Delta s}{2}\left(1 + \tanh\left(\frac{z_0 - z}{\Delta z}\right)\right), \tag{2.14}$$

where z_0 sets the stratification midpoint, and Δz is the half-width of the pycnocline. T_0, ΔT, and Δs are chosen so that there is an upper layer of hot, salty water (40°C, 5 psu), and a lower layer of cool, fresh water (15°C, 0 psu), with densities of 995.91 kg/m³ and 999.12 kg/m³, respectively. Along the stratification midpoint, $(T_0, s_0) = (27.5°C, 2.5\,\text{psu})$, giving a density of 998.27 kg/m³. Linearizing around the cool, fresh state, the midpoint state, and the hot, salty state yields

$$\rho_{\text{lin}}^{(15°C, 0\,\text{psu})}(T, s) = (999.12 - 0.15°C^{-1}(T - 15°C) + 0.77\,\text{psu}^{-1}s)\,\text{kg/m}^3, \tag{2.15}$$

12

	Density / kg/m³				
Equation	$(15°\text{C}, 0\,\text{psu})$	$(27.5°\text{C}, 2.5\,\text{psu})$	$(40°\text{C}, 5\,\text{psu})$	$\alpha\,/\,°\text{C}^{-1}$	$\beta\,/\,\text{psu}^{-1}$
(2.3)	999.12	998.27	995.91		
$\rho_{\text{lin}}^{(15°\text{C},0\,\text{psu})}$	999.12	999.18	999.24	1.5×10^{-4}	7.7×10^{-4}
$\rho_{\text{lin}}^{(27.5°\text{C},2.5\,\text{psu})}$	999.95	998.27	996.59	2.8×10^{-4}	7.5×10^{-4}
$\rho_{\text{lin}}^{(40°\text{C},5\,\text{psu})}$	1001.83	998.87	995.91	3.8×10^{-4}	7.4×10^{-4}

Table 2.2: Estimates of density at different values of temperature and salinity using the nonlinear equation (2.3), and three linear approximations (2.15), (2.16), and (2.17), with associated coefficients of thermal expansion and haline contraction.

$$\rho_{\text{lin}}^{(27.5°\text{C},2.5\,\text{psu})}(T, s) = (998.27 - 0.28°\text{C}^{-1}(T - 27.5°\text{C})$$
$$+ 0.75\,\text{psu}^{-1}(s - 2.5\,\text{psu}))\,\text{kg/m}^3, \qquad (2.16)$$

and

$$\rho_{\text{lin}}^{(40°\text{C},5\,\text{psu})}(T, s) = (995.91 - 0.38°\text{C}^{-1}(T - 40°\text{C})$$
$$+ 0.74\,\text{psu}^{-1}(s - 5\,\text{psu}))\,\text{kg/m}^3. \qquad (2.17)$$

The densities at each state given by each of the linearizations, and the corresponding thermal expansion and haline contraction coefficients are presented in Table 2.2. Although the haline contraction coefficient is similar for all three states, when linearized around the hot, salty state, the thermal expansion coefficient is about 2.5 times greater than when linearized about the cool, fresh state, and about 1.4 times greater than when linearized about the interfacial state. Equation (2.15) (equation (2.17)) overestimates the density of the hot, salty state $\rho_{\text{lin}}^{(15°\text{C},0\,\text{psu})}(40°\text{C}, 5\,\text{psu}) = 999.24\,\text{kg/m}^3$ (cool, state $\rho_{\text{lin}}^{(40°\text{C},5\,\text{psu})}(15°\text{C}, 0\,\text{psu}) = 1001.83\,\text{kg/m}^3$), compared to the value obtained by equation (2.3) of $\rho(40°\text{C}, 5\,\text{psu}) = 995.91\,\text{kg/m}^3$ ($\rho(15°\text{C}, 0\,\text{psu}) = 999.12\,\text{kg/m}^3$). Additionally, the density difference between the hot, salty state and the cool, fresh state, which equation (2.3) gives as $3.21\,\text{kg/m}^3$, is misrepresented by both linearizations. Equation (2.15) underestimates the density difference as $0.12\,\text{kg/m}^3$, while (2.17) overestimates it as $5.92\,\text{kg/m}^3$, which are 3.8% and 184.5% of the actual difference, respectively. This indicates that though a linear equation of state may be a reasonable approximation near the state about which it is linearized, the density approximation away from that state has the potential to be fairly inaccurate.

2.1.4   Dimensionless Parameters and Stability Analysis

Double-diffusive flows can be described using a number of dimensionless parameters. As mentioned in Chapter 1, the Prandtl number

$$\mathrm{Pr} = \frac{\nu}{\kappa_T}, \tag{2.18}$$

and the Schmidt number

$$\mathrm{Sc} = \frac{\nu}{\kappa_s}, \tag{2.19}$$

relate the diffusivities of heat and salinity to the kinematic viscosity. The relative strengths of the diffusivities are related to one another through the diffusivity ratio,

$$\tau = \frac{\kappa_s}{\kappa_T}. \tag{2.20}$$

In the ocean, typical values for each of these parameters are $\mathrm{Pr} = 7$, $\mathrm{Sc} = 700$, and $\tau = 10^{-2}$, while in salt-sugar systems, $\mathrm{Pr} = 1000$, $\mathrm{Sc} = 3000$, and $\tau = 1/3$. In the double-diffusive simulations presented in this thesis, $\mathrm{Pr} = 5.88$, $\mathrm{Sc} = 100$, and $\tau = 5.88 \times 10^{-2}$. Both the Prandtl and Schmidt numbers examined here are lower than the typical oceanic values, while the diffusivity ratio is greater than the typical oceanic value. The use of values lower than those in the ocean is due to the high number of grid points required to resolve the resulting diffusive interfaces, and the computational constraints that result from modelling such a large grid. For comparison purposes, a list of dimensionless parameters used in past 3D numerical studies can be found in Table 1.2. Prandtl numbers were typically chosen in those simulations to reflect the value in the ocean, though the value used by Carpenter et al. [11] was chosen to reflect the value measured in Lake Kivu. While Kimura and Smyth [43] and Carpenter et al. [11] were able to use a physical value of τ, it was set to be greater than 10^{-2} in the majority of simulations.

Salt Finger Growth Rate

In linear stability analysis, the buoyancy ratio is defined as

$$R_\rho = \frac{\alpha T_z}{\beta s_z}. \tag{2.21}$$

Applying both (2.9) and (2.10) to equation (2.21) gives a nonlinear buoyancy ratio of

$$R_\rho = \frac{-(c_2 + 2c_4 T + c_5 s + 3c_6 T^2 + 2c_7 sT)T_z}{(c_3 + c_4 T^2 + c_5 T + c_7 T^2)s_z}. \tag{2.22}$$

14

Huppert and Manins [33] determined that in order for salt fingers to develop along a thermohaline interface, the inequality

$$R_\rho < \frac{1}{\tau^{3/2}} \tag{2.23}$$

must be satisfied. This inequality can also be limited from below as $1 < R_\rho < \tau^{-3/2}$, since $R_\rho < 1$ implies that based on the linear equation of state (2.6), the fluid is initially unstably-stratified

$$\frac{\partial \rho}{\partial z} = -\alpha T_z + \beta s_z = (1 - R_\rho)\beta s_z = \left(\frac{1}{R_\rho} - 1\right)\alpha T_z > 0, \tag{2.24}$$

provided either $s_z > 0$ or $T_z > 0$, both of which are necessary conditions for salt fingers. Kunze [47] estimated the wavelength of the fastest-growing salt fingers as

$$\lambda_{\mathrm{SF}} = 2\pi \left(\frac{\nu\kappa_T}{g\beta s_z (R_\rho - 1)}\right)^{\frac{1}{4}}, \tag{2.25}$$

with a corresponding initial growth rate of

$$\sigma_{\mathrm{SF}} = \frac{1}{2}\sqrt{\frac{(\kappa_T - R_\rho\kappa_s)\,g\beta s_z}{\nu}}\left(\sqrt{R_\rho} - \sqrt{R_\rho - 1}\right), \tag{2.26}$$

where s_z is the initial linear salinity gradient. Using the definition of the thermal expansion coefficient (2.7) and the haline contraction coefficient (2.8), equation (2.26) can be written as

$$\sigma_{\mathrm{SF}} = \frac{1}{2}\sqrt{\frac{\left(\kappa_T \frac{\partial \rho}{\partial s}\beta s_z + \kappa_s \frac{\partial \rho}{\partial T}T_z\right)g}{\rho\nu}}\left(\sqrt{R_\rho} - \sqrt{R_\rho - 1}\right). \tag{2.27}$$

Standard linear stability analysis of the equations governing salt fingers assumes that the initial heat and salt distributions are linear

$$T(\boldsymbol{x}, t = 0) = T_0 + \frac{\Delta T}{H}z, \tag{2.28}$$

$$s(\boldsymbol{x}, t = 0) = s_0 + \frac{\Delta s}{H}z, \tag{2.29}$$

where H gives the height of the domain, implying that $T_z = \Delta T/H$ and $s_z = \Delta s/H$. Though the initial temperature and salinity stratifications (equations (2.13) and (2.14)) are not linear over the vertical domain in this simulation, the hyperbolic tangent functions

15

are nearly linear about $z = z_0$, where salt fingers are expected to develop. In this region, the stratifications can be approximated as

$$T_{\text{Lin}}(z) = T_0 + \frac{\Delta T}{2} + \frac{\Delta T}{2\Delta z}(z - z_0), \tag{2.30}$$

and

$$s_{\text{Lin}}(z) = s_0 + \frac{\Delta s}{2} + \frac{\Delta s}{2\Delta z}(z - z_0), \tag{2.31}$$

which implies that, near $z = z_0$,

$$\frac{\partial T_{\text{Lin}}}{\partial z}(z) = \frac{\Delta T}{2\Delta z}, \tag{2.32}$$

$$\frac{\partial s_{\text{Lin}}}{\partial z}(z) = \frac{\Delta s}{2\Delta z}. \tag{2.33}$$

The wavelength of the fastest-growing fingers and the associated initial growth rate can be estimated by evaluating R_ρ at $(T(z_0), s(z_0)) = \left(T_0 + \frac{\Delta T}{2}, s_0 + \frac{\Delta s}{2}\right)$, and approximating T_z and s_z with equations (2.32) and (2.33). Using these estimates, R_ρ can be simplified to

$$R_\rho = \frac{-(c_2 + 2c_4 T + c_5 s + 3c_6 T^2 + 2c_7 sT)\Delta T}{(c_3 + c_5 T + c_7 T^2)\Delta s}. \tag{2.34}$$

Evaluating at the midpoint of the salt fingering pycnoclines presented in this thesis, $(T_0, s_0) = (27.5°\text{C}, 2.5\,\text{psu})$, and using the temperature and salinity changes across the layers of $\Delta T = 25°\text{C}$ and $\Delta s = 5\,\text{psu}$, gives a density ratio of $R_\rho = 1.9$. This satisfies the inequality condition for salt fingers, since $\tau^{-3/2} = 70$.

Growth Rate of Rayleigh-Taylor Instabilities

The Atwood number,

$$A = \frac{\rho_H - \rho_L}{\rho_H + \rho_L}, \tag{2.35}$$

is a measure of the density difference between layers of stratified flows, where ρ_H is the density of the heavy fluid, and ρ_L is the density of the light fluid. In a typical configuration resulting in Rayleigh-Taylor instabilities, ρ_H would be the density of the upper fluid, ρ_L would be the density of the lower fluid. Rising and falling Rayleigh-Taylor instabilities are referred to as bubbles and spikes, respectively. For smaller values of the Atwood number $(A \ll 1)$, for which the Boussinesq approximation is valid, the penetration (that is, the

height (depth) that the bubbles (spikes) rise (fall) from the original pycnocline) should be nearly equal for the bubbles and spikes [3]. For larger values of the Atwood number ($A \lesssim 1$), the penetration of the bubbles is much lower than the penetration of the spikes. According to Youngs [122], the most unstable wavelength for Rayleigh-Taylor instabilities under the effects of viscosity can be approximated as

$$\lambda_{\mathrm{RT}} \approx 4\pi \left(\frac{\nu^2}{g\, A} \right)^{\frac{1}{3}}, \tag{2.36}$$

and a corresponding growth rate of

$$\sigma_{\mathrm{RT}} = \left(\frac{\pi g\, A}{\lambda_{\mathrm{RT}}} \right)^{\frac{1}{2}}. \tag{2.37}$$

2.2 Dissipation, Stirring, and Mixing

An advantage of numerical simulation is that it is straightforward to compute diagnostic values and geometric patterns of quantities like dissipation, stirring, and mixing, variables that cannot be directly measured through experiment. The rate of viscous dissipation of an incompressible fluid is defined as

$$\phi = 2\nu\rho_0 e_{ij} e_{ij}, \tag{2.38}$$

where $e_{ij} = \frac{1}{2} \left(\frac{\partial u_i}{\partial x_j} + \frac{\partial u_j}{\partial x_i} \right)$ is the rate of strain tensor for an incompressible fluid. It is a measure of the irreversible conversion of mechanical energy to heat (or internal energy) due to viscosity. Though the terms stirring and mixing are often used interchangeably in casual conversation, their technical definitions are more distinct. Stirring refers to the reversible mechanical process which increases the variability of a tracer by increasing the surface area between regions of high and low tracer concentration, increasing the gradient along these interfaces. Mixing is the process that irreversibly decreases variability due to molecular diffusion. A metric of the total variability of a scalar tracer field θ can be defined [15, 79] as

$$C \equiv \frac{1}{2} \iiint\limits_V \boldsymbol{\nabla}\theta \cdot \boldsymbol{\nabla}\theta \, dx \, dy \, dz. \tag{2.39}$$

If the tracer flow is governed by a conservation equation in the form of (2.4) and (2.5), the rate of change of the total variability can be computed as

$$\frac{dC}{dt} = \iiint\limits_V \left(\boldsymbol{u} \cdot \boldsymbol{\nabla}\theta \right) \nabla^2\theta - \kappa \left(\nabla^2\theta \right)^2 \, dx \, dy \, dz, \tag{2.40}$$

where κ is the diffusivity of the tracer. The first and second terms on the right-hand side of this relationship give measures of the stirring and mixing, respectively. The stirring term can have either sign, while the mixing term is always negative, as variability is decreased by mixing. Positive stirring can also lead to an indirect increase in the mixing, since it increases the spatial variability of the tracer. This will lead to an overall decrease in total variability.

2.3 Fourier Analysis

For a general function $f(x)$, where x is the position in physical space, the Fourier transform is given by

$$\hat{f}(k) = \int_{-\infty}^{\infty} f(x) e^{-ikx} dx, \tag{2.41}$$

where $\hat{f}(k)$ is the Fourier transform of f, and k is the wave number, equal to $2\pi/\lambda_x$, where λ_x is the corresponding physical wavelength. In this manuscript, the Fourier transform of a variable will be indicated by a hat. To convert from Fourier space back into physical space, the inverse Fourier transform is defined as

$$f(x) = \frac{1}{2\pi} \int_{-\infty}^{\infty} \hat{f}(k) e^{ikx} dx. \tag{2.42}$$

Since the Fourier transform is complex in general, it is customary to examine its magnitude, $\left|\hat{f}\right|$, which provides the strength of each wave number's (or wavelength's) contribution to the physical variable. For example, consider a simple sine curve with period 2π, as presented in Fig. 2.1(a). The Fourier spectrum, $\left|\hat{f}\right|$, given in Fig. 2.1(c), indicates that the component wave number of this function is $k = 1$. For a function that is the sum of multiple sines and cosines, such as in Fig. 2.1(b), the spectrum Fig. 2.1(d) indicates the contributions from both of its component wave numbers, 2 and 3.

The Fourier transform can also be extended to two dimensions. For physical variables x and z, the Fourier transform becomes

$$\hat{f}(k, m) = \int_{-\infty}^{\infty} \int_{-\infty}^{\infty} f(x, y) e^{-ikx} e^{-imz} dx dz, \tag{2.43}$$
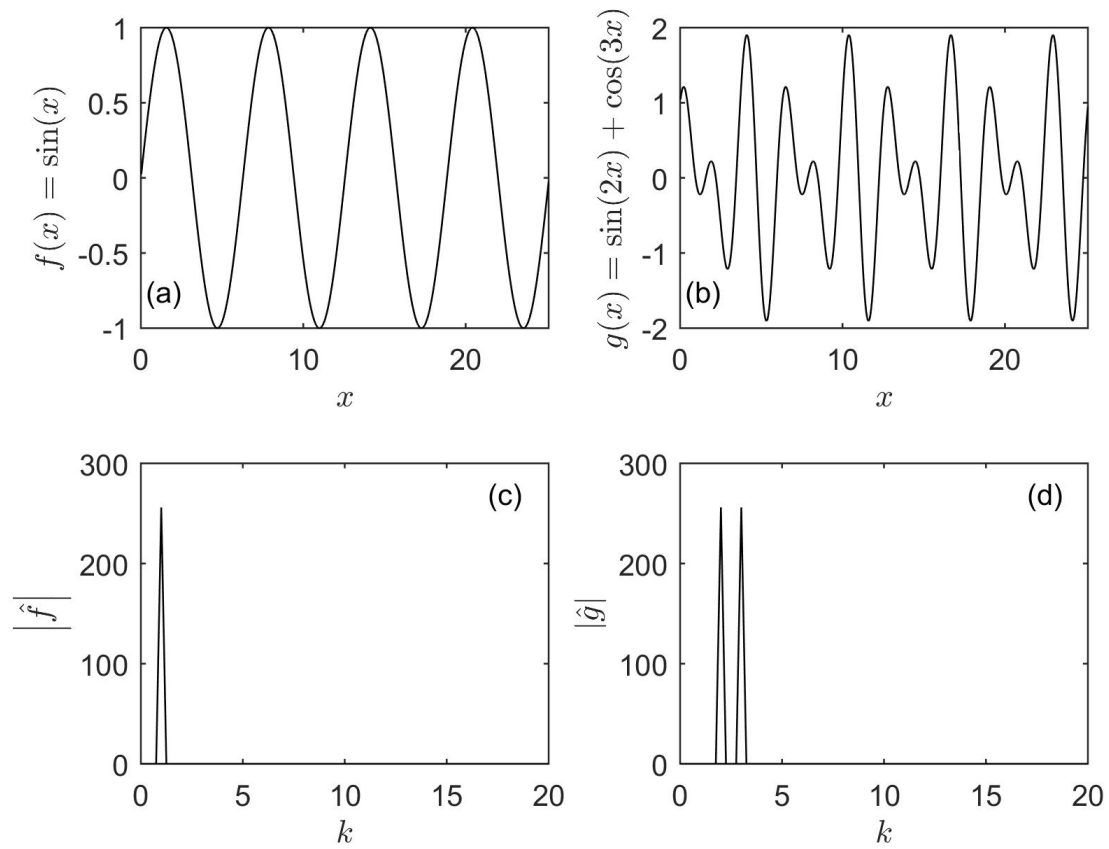
Figure 2.1: Line plots of (a) $f(x) = \sin(x)$ and (b) $g(x) = \sin(2x) + \cos(3x)$, with Fourier spectra in (c) and (d), respectively.

with corresponding inverse Fourier transform,

$$f(x, z) = \frac{1}{(2\pi)^2} \int\limits_{-\infty}^{\infty} \int\limits_{-\infty}^{\infty} \hat{f}(k, m) e^{ikx} e^{imz} dk dm, \qquad (2.44)$$

where k and m are the wave numbers corresponding to x and z, respectively. In this thesis for a given three-dimensional position vector $\boldsymbol{x} = (x, y, z)$, the corresponding wave number vector is written as $\boldsymbol{k} = (k, l, m)$. Two-dimensional Fourier transforms produce signals that indicate the strength of the component wave numbers, with some directional information included. For example, Fig. 2.2(a) shows a contour plot of the function $f(x, z) = \sin(4x)$, which oscillates only in the x-direction with wave number $k = 4$ and period $\pi/2$. The resulting two-dimensional spectrum in Fig. 2.2(c) (presented as a contour plot of $\log_{10} |\hat{f}|$), shows peaks at $\boldsymbol{k} = (4, 0)$ and $\boldsymbol{k} = (-4, 0)$, indicating only horizontal variation in the data. Fig. 2.2(b) shows a contour plot of the function $g(x, z) = \sin(2x + 2z)$, which is a sine curve that oscillates diagonally across the xz-plane. Its spectrum (Fig. 2.2(d)), indicates peaks at $\boldsymbol{k} = (2, 2)$ and $\boldsymbol{k} = (-2, -2)$, representing the diagonal structure in the positive x- and z-directions (or equivalently, the negative x- and z-directions). Since Fourier transforms treat the data as if it exists on an infinite domain with an infinite number of copies of the data extending in both directions, the functions and domain presented in Fig. 2.2 were chosen so that a replication of the data in both directions would be continuous and smooth.

In the event that two-dimensional data does not smoothly transition at the boundaries when replicated, a feature arises in the spectrum known as the edge effect. This results in exaggerated signals at the lowest wave number corresponding to the length of the domain which can pollute the spectra. For example, consider a slice of a three-dimensional density field after the flow has become well-developed, with no-flux boundary conditions on all sides, as presented in Fig. 2.3(a). This is a slice of the density field from the double-diffusive Rayleigh-Taylor simulation analyzed in Chapter 4. The field shows clearly distinct features at opposite sides of the domain, and as a result the corresponding two-dimensional spectrum in Fig. 2.3(b) shows exaggerated contributions from smaller wave numbers along the vertical and horizontal wave number axes.

One approach to curtail this behaviour is to apply a windowing function to the data, which tapers the data toward zero at the boundaries. A second approach is to extend the data with reflected copies at each of the boundaries, and take the transform of a field that is four times the size of the original. The reflected extension ensures the data is periodic in both directions, with a horizontal and vertical periods of twice the initial horizontal and vertical lengths. This second approach is relatively straightforward in the
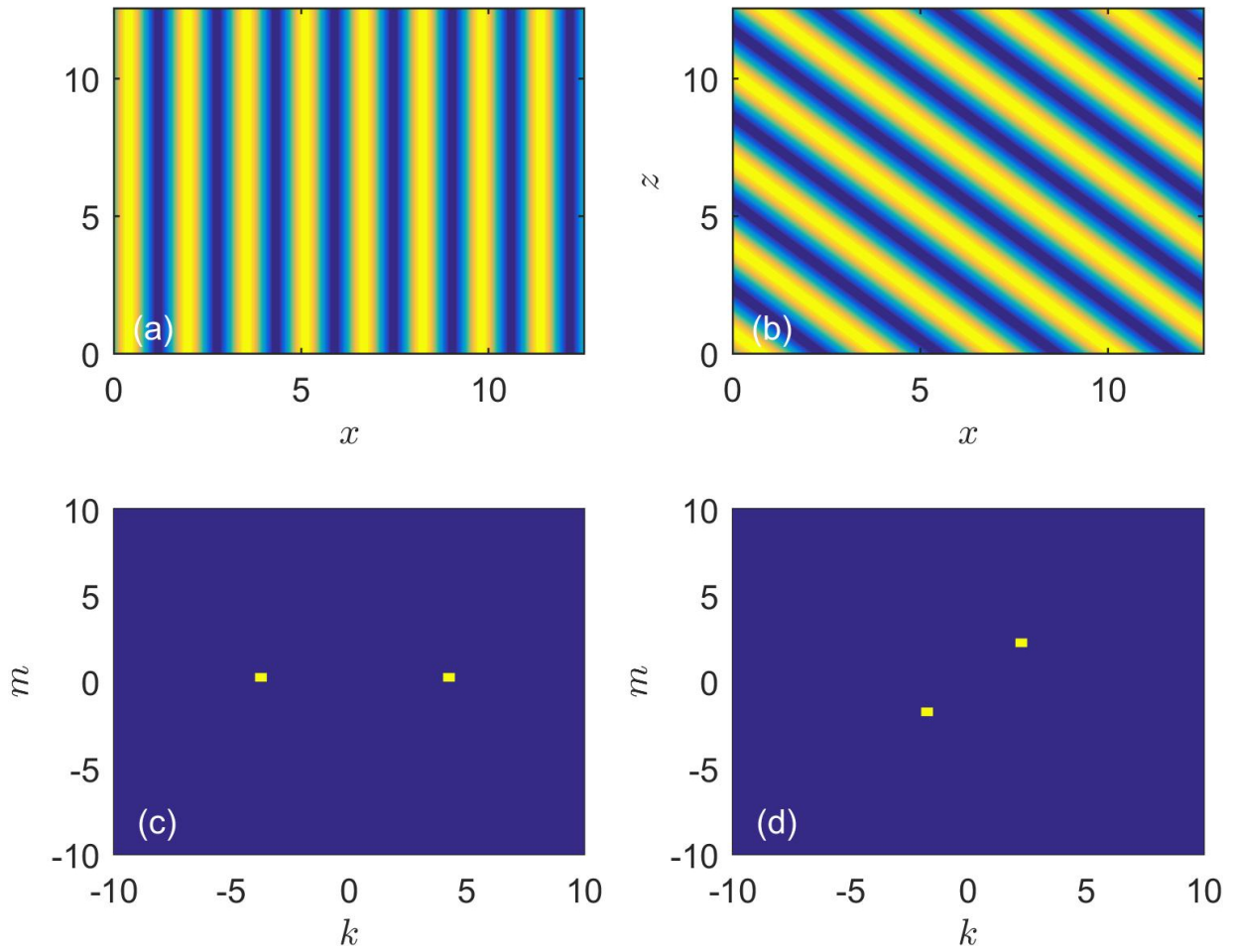
Figure 2.2:   Contour plots of (a) $f(x,z) = \sin(4x)$ and (b) $g(x,z) = \sin(2x+2z)$, with the base 10 logarithm of the corresponding two-dimensional spectra in (c) and (d), respectively.
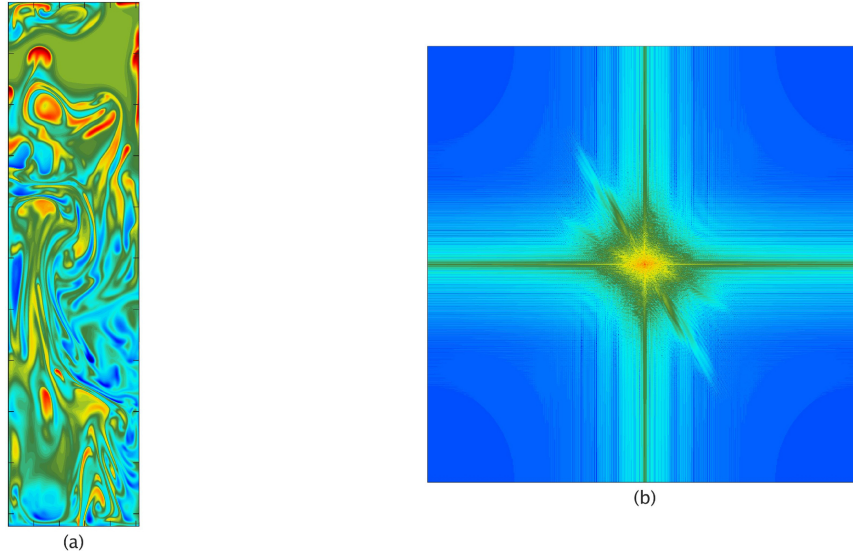
Figure 2.3: (a) Density contour plot and (b) the resulting 2D spectrum.

current investigation, since the boundary conditions of the flow variables dictate the type of extension that should be used.

Numerically, the code treats variables with Neumann boundary conditions (such as the tracers or velocities parallel to the boundary in the case of free-slip conditions) using cosine expansions, which implies an even extension at each of the boundaries. For fields with Dirichlet boundary conditions (e.g., free-slip conditions where the direction of the velocity is normal to the boundary, $\boldsymbol{u} \cdot \hat{n} = 0$), SPINS uses sine expansions, implying an odd extension at the boundary. The former amounts to a reflection of the data field across the appropriate boundary, while the latter is the negative of the reflection.

Returning to the density field in Fig. 2.3(a), even extensions can be applied to the field in both directions, giving the extended field presented in Fig. 2.4(a). The resulting spectrum is presented in Fig. 2.4(b). The contamination at lower wave numbers is not present in this spectrum, however, there is a loss of directional information because the extended density field is symmetric in horizontal and vertical direction, giving a spectrum that is symmetric across both axes. This is not a significant concern for this research, since the primary interest is to estimate the dominant length scales of the different variables.
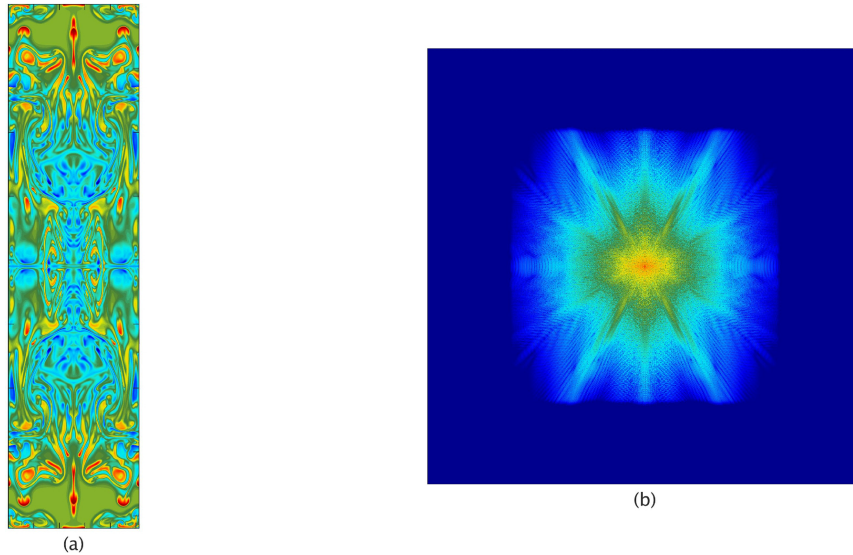
Figure 2.4: (a) Density contour plot with evenly extended copies and (b) the resulting 2D spectrum.

2.4 Flow Visualization

One of the primary benefits of numerical simulation is that it allows detailed analysis of physical flow features through the use of visualization software that is not afforded by laboratory experiments. The challenge is then to be able create visualizations that capture important details of the flow without overwhelming the reader with extraneous or overrepresented features. Throughout this thesis, VisIt, an open source visualization software [12], was used to create most three-dimensional figures. In this section, a brief overview of some the features of VisIt is provided, with a focus on software manipulation for efficient production of high-quality publication-ready images. It is written to serve as an informal guide for future students in the Environmental and Geophysical Fluid Dynamics Group, with a focus on creating volume plots. Further details can be found in the VisIt User's Manual [1].

The Expression Window

The Expression Window allows for the simple arithmetic combination of multiple data fields for plotting purposes without the need for external calculation of additional fields,
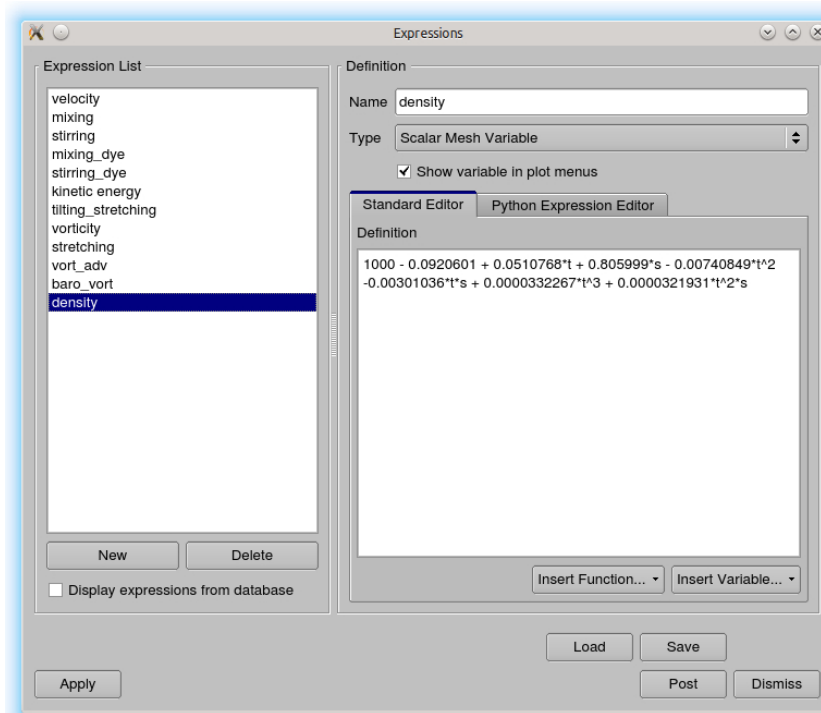
Figure 2.5: The Expression Window, with equation of state (2.3) defined for computation of the density field inside VisIt when the temperature and salinity fields are opened.

and expresses them as different types of mesh variables, including scalars (e.g., density) and vectors (e.g., velocity). For example, Fig. 2.5 presents the definition of density as determined by equation (2.3) saved in the Expression Window. When the temperature, t, and salinity, s, fields are opened as active sources, VisIt makes the density field available for plotting, without the need for an externally stored file. This saves on the overall memory needed to store simulation data.

2.4.1 Creating Volume Plots

An important feature of any visualization software is the ability to manipulate images in real time in order to view features from different orientations. Unfortunately, as the object becomes more complicated, for example, by increasing the degree of transparency, manipulation may take longer due to the additional computational power required to render

the object. Therefore, an operation that should occur smoothly and instantaneously, such as rotation, can instead become staggered and take significantly longer. It is advised that orientation of the graphical object is best done early in processing, for example, prior to increasing the transparency or changing to a more complex rendering method.

The Transfer Function

Volume plots are drawn using a "volume transfer function," which applies both colour and opacity values to a given value of the data. The transfer function can be defined under the "1D Transfer Function" tab of the Volume Plot Attribute window. Under this tab, the colour and the opacity of the transfer function can be defined. The "Color Table" option contains a number of default options for the colour map. The extrema of the colour map, are set by default to the minimum and maximum of the data, and can be changed manually. Above the colour table are a number of arrows (colour control points) which can be used to reorder the colour map. The Opacity section sets the opacity of the data values, and can be defined in two ways. The first is Freeform, where by dragging the cursor over the opacity table while pressing the left mouse key allows freehand drawing of the opacity function. The second is Gaussian, where a number of editable Gaussian functions can be applied to the table. Additionally, the opacity spectrum displays the proportion of the data that would be displayed by a given colour using black bars. The taller the bar, the more of the volume plot would be filled by that colour. These bars can be used to determine the best way to determine the opacity function. For example, consider the density field of a double-diffusive Rayleigh-Taylor instability (from Chapter 4) presented in the visualization window in Fig. 2.6. The opacity spectrum shows that most of the plot contains either low density fluid in red, or high density fluid in blue. Using the default linear opacity function obscures the action above the upper pycnocline as low densities bubbles rise upwards into the high density fluid. To better show the action above the upper pycnocline, Fig. 2.7 uses a freehand opacity function to tag the regions of low and high densities regions with highly transparent red and blue, while the regions around the pycnoclines are made opaque. As a result, there is still an indication of the regions of high and low density fluid that dominate the domain, while also displaying the action above and below the upper pycnocline.

Rendering Methods

VisIt offers several different rendering options for volume plots. By default, it uses the "Splatting" method, where the transfer function defines the colours and opacities of a set of textured polygons that are plotted over a resampled mesh of the data. Though this
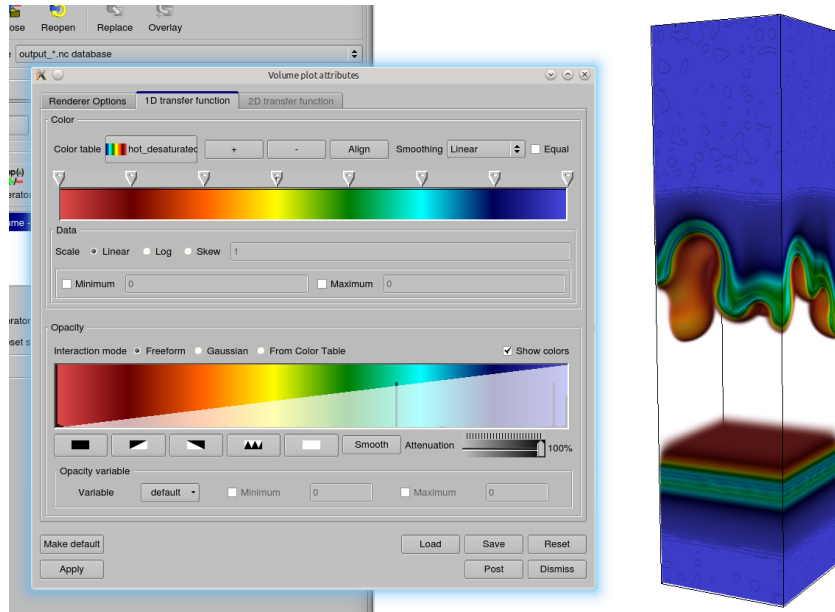
Figure 2.6: Volume plots of density using ray casting and a linear opacity function.

rendering method is quick, if too few points are used in the resampled mesh, the resulting image can be fuzzy and poorly represent the data. This is shown in Fig. 2.8(a), which uses the default settings of the Splatting method to create the volume plot. The "Ray Casting" method, which is used to create the volume plots presented in this thesis, takes longer to render using the default settings than Splatting, but with improved results. Instead of sampling the data on a new mesh, Ray Casting samples the data at various points along a ray traced from the computer screen through the data. The opacities and colours at each of these sampled points are then combined to determine the colour of the pixel displayed on the screen [1].

As a note, VisIt can only display a single volume plot at a time. In order to plot multiple variables at once (e.g., density and dissipation), a different plotting method, such as isosurfaces, would need to be used [1].

2.4.2 Python Scripting

In addition to using its GUI for graphical manipulation, VisIt can use Python scripting to create plots through its command line interface (CLI). The CLI is found under the
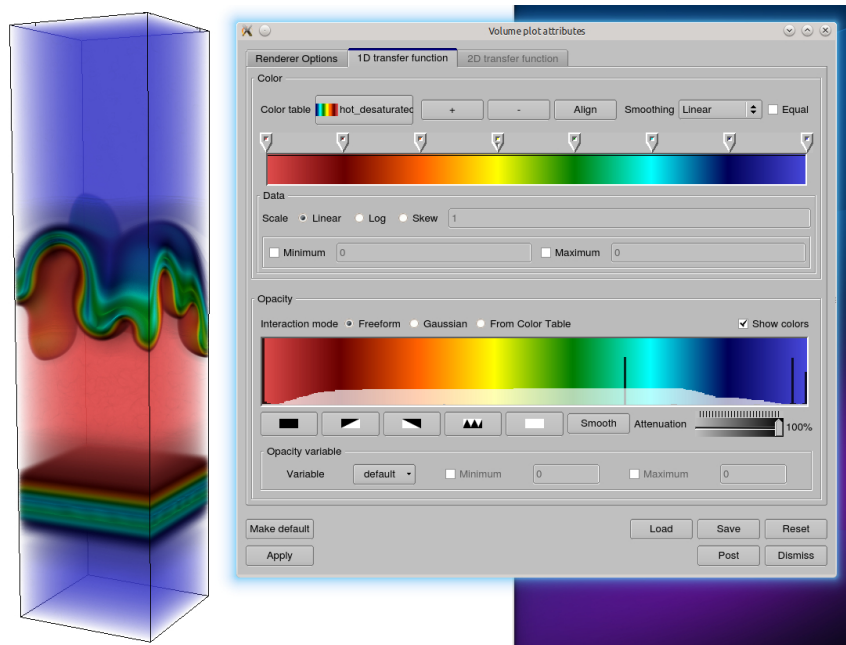
Figure 2.7:   Volume plots of density using ray casting and a hand-drawn opacity function.
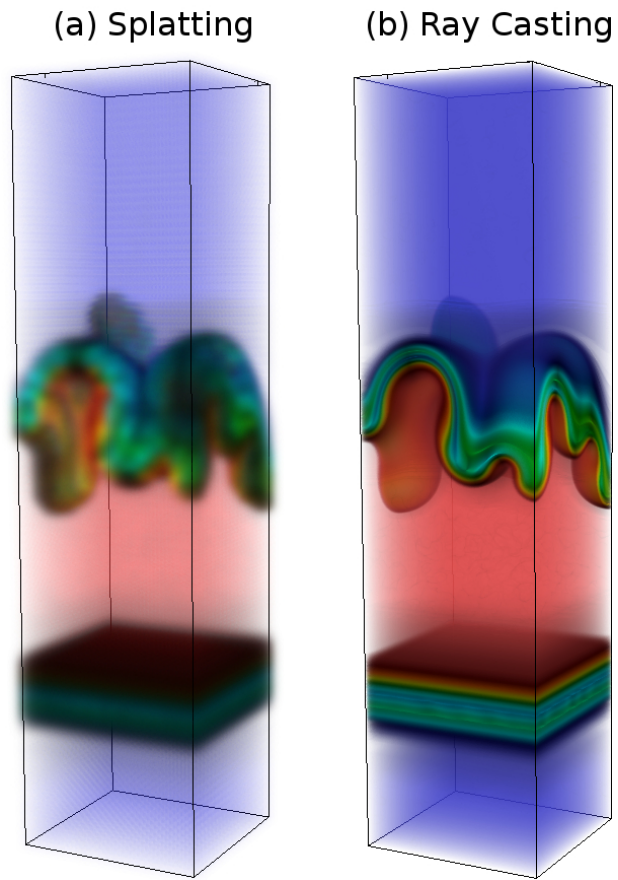
Figure 2.8: Volume plots of the same density field using VisIt's default settings for (a) splatting and (b) ray casting.

Controls tab in the menu bar. Though creating plots directly from a Python script does not offer the convenience of direct graphical manipulation, VisIt gives the option to record any manipulations in a Python script so the plot can easily be recreated later. After manipulating the plot to achieve the desired visualization, annotations, colours, etc., the sequence of commands

```
f=open(''script.py'',''wt'')

WriteScript(f)

f.close()
```

should be run in the CLI, as per the VisIt Python Manual [113]. This opens a file called `script.py` to which the script will be written, then the `WriteScript` function records every manual change made in the VisIt window to that file. It can be then run later in the CLI using the command

```
Source(''script.py'').
```

In practice, `WriteScript` may sometimes ignore certain commands and transformations, so repeated runs may be necessary to create different scripts with the desired commands. The desired attributes can then all be collected in a single script.

Chapter 3

Double-Diffusive Gravity Currents

Results from this chapter were initially published in

J. Penney and M. Stastna. Direct numerical simulation of double-diffusive gravity currents. *Physics of Fluids*, 28:086602, 2016.

3.1 Gravity Currents

Gravity currents are a well-documented naturally occurring and industrial phenomenon that develops because of a density gradient between interacting masses of fluids. In-depth overviews can be found in Simpson [90] and Simpson [91]. When two masses of fluids of different density distributed laterally come into contact, the heavier fluid will flow underneath the lighter fluid in order to create a stable density stratification, with the motion of the flow being primarily horizontal. Two primary factors may be the cause of this gradient: differences in temperature or differences in the amount of dissolved or suspended material. In the event that the density gradient is dependent on both of these properties, double-diffusive instabilities may develop.

Gravity current geometry is largely dependent on fluid properties and nearby boundary conditions. Inviscid theory analysis [108, 5] has been used to predict gravity current heads with shapes similar to the one presented in Fig. 3.1(a). When a gravity current flows along a solid no-slip boundary, a characteristic spanwise "lobe-and-cleft" instability is produced in the head, and a thin boundary layer tends to form, as in Fig. 3.1(b). Simpson [89] observed this instability along a no-slip bottom boundary in laboratory experiments, and was able to suppress it by moving the boundary with the gravity current speed to
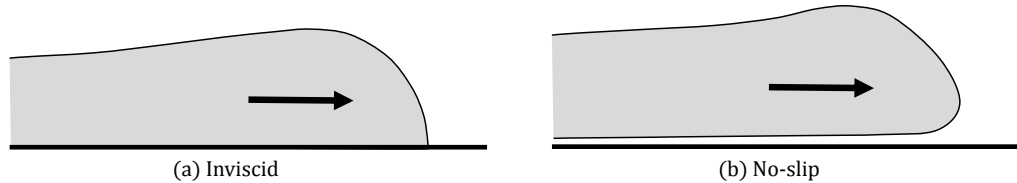
(a) Inviscid   (b) No-slip

Figure 3.1: (a) The shape of a gravity current head predicted using inviscid theory, and (b) the typical shape of gravity current heads observed along no-slip boundaries.

reduce the effects of viscosity, similar to the flow predicted by inviscid theory [5]. Härtel et al. [28] presented the first direct numerical simulation (DNS) characterizing the lobe-and-cleft structure in gravity currents arising from a lock-exchange configuration. The mechanism leading to the lobe-and-cleft instability was further examined through linear stability analysis in the companion paper [27], in which the authors determined that it is an effect of the combination of an unstable density stratification and the hyperbolic velocity profile near the stagnation point and nose of the current head.

For gravity currents that can give way to salt fingers, the shear along the current is likely to affect finger development. The presence of shear in regions of the ocean where double-diffusion may be important has led to a number of studies of salt fingering in the presence of shear. An early set of important experiments was performed by Linden [50], which examines salt fingers in a steady shear flow using both two-layer heat-salt and salt-sugar systems. The key result of this paper was the first observation of "salt sheets." It was observed that in the absence of shear, salt fingers developed as normal, though the length of heat-salt fingers were comparable to the tank depth, while the salt-sugar fingers were much shorter. However, the fingers aligned parallel to the direction of flow as shear was applied. As shear was increased, the streamwise variability of the fingers decreased until they formed two-dimensional sheets. It was noted that "[a]t no stage was it possible to inhibit the formation of these longitudinal sheets by the shear." In recent years, double-diffusive systems in the presence of shear have been the subject of several 3D DNS papers, particularly systems resulting in salt sheets [43, 44] and Kelvin-Helmholtz billows [93, 92].

The numerical simulations presented in this chapter are designed to simulate dam-break or lock-exchange flows that can be easily implemented in laboratory experiments. Fig. 3.2 presents the results of such an experimental setup, where a layer of lighter, warm, salty water (on the right, in blue) is separated from denser, cool, fresh water in the rest of the tank by an acrylic divider. The divider is slowly removed to reduce instabilities, allowing the

31

Figure 3.2: Photograph of a double-diffusive gravity current, with warm, salty water in blue moving leftward.

salty water to form a surface gravity current above the fresh water and flow leftward. This is analogous to, though obviously much smaller in scale than, two different cases of riverine outflow. The first is when cold fresh water is discharged from the mouth of a river into warmer salt water. The second is when sediment-laden water flows into denser, cool brine [67], although the details of the physics may differ due to the insoluble nature of sediment and the addition of settling velocities to the equations of motion. Sedimenting gravity currents have been the subject of a number of experimental [23, 56, 67] and numerical [10, 61, 62] studies. Despite a number of similarities between sedimenting and double-diffusive gravity currents (as observed by Maxworthy [56]), there has been less discussion of double-diffusive currents in scientific literature. Past studies have been primarily limited to laboratory experiments, such as heated saline jets along the surface of water [101], surface double-diffusive gravity currents [55], and lock-exchange experiments [121] using sugar-salt systems. Yoshida and Nagashima [120] provide a review of numerical and experimental research related to double-diffusive intrusions prior to 2003, and while some older examples of two-dimensional numerical models of double-diffusive gravity currents or intrusions are

cited [39, 60], to our knowledge, three-dimensional DNS has remained largely unexamined. Konopliv and Meiburg [45] presented a 3D simulation of a lock-exchange double-diffusive gravity current with free-slip conditions along all sides, though that paper was primarily a parametric study of two-dimensional lock-exchange double-diffusive gravity currents to examine the effects of varying diffusivity and buoyancy ratios. Overall, they observed a more rapid loss of heat and salt for strongly double-diffusive flows (lower τ) than for weakly double-diffusive flows (higher τ). Additionally, they noticed faster fingering in their 3D simulation than in their 2D simulations.

3.2 Mathematical Formulation

In order to simulate a dam-break situation, the temperature and salinity fields are initially distributed in the streamwise direction using hyperbolic tangent functions in terms of x,

$$T\left(\boldsymbol{x}, t=0\right) = T_0 + \frac{\Delta T}{2}\left(1 + \tanh\left(\frac{x_0 - x}{\Delta x}\right)\right),\tag{3.1}$$

$$s\left(\boldsymbol{x}, t=0\right) = \frac{\Delta s}{2}\left(1 + \tanh\left(\frac{x_0 - x}{\Delta x}\right)\right),\tag{3.2}$$

where x_0 sets the density distribution midpoint, and Δx defines the width of the pycnocline. For these simulations, the cool water temperature is set to $T_0 = 15\,°\mathrm{C}$, the change in temperature between layers is $\Delta T = 25\,°\mathrm{C}$, and the change in salinity is $\Delta s = 5\,\mathrm{psu}$. The stratification width is set by $\Delta x = 0.5\,\mathrm{cm}$. These values result in an initial layer of hot, salty water $(40,°\,\mathrm{C}, 5\,\mathrm{psu})$ on the left side of the domain, and cool, fresh water $(15,°\,\mathrm{C}, 0\,\mathrm{psu})$ on the right. Additionally, the initial density of the warm water is $995.91\,\mathrm{kg/m^3}$, while the initial density of the cool water is $999.12\,\mathrm{kg/m^3}$, giving a density difference of $3.21\,\mathrm{kg/m^3}$. These stratifications are designed to simulate lock-exchange or dam-break setups, which are common configurations in laboratory experiments. Along each boundary, no-flux conditions are assumed for both tracers.

The domain for each of the simulations is $L_y = 4\,\mathrm{cm}$ wide in the spanwise direction, $L_z = 4\,\mathrm{cm}$ high in the vertical direction, and either $L_x = 20\,\mathrm{cm}$ or $40\,\mathrm{cm}$ long in the streamwise direction (designated SD or LD in the naming convention for short domain or long domain, respectively). $N_x = 2048$ grid points are used in the x-direction for the short domain experiments (4096 in the long domain experiments) resulting in a streamwise grid spacing of $9.77 \times 10^{-3}\,\mathrm{cm}$. $N_y = 128$ grid points are used in the y-direction, for a spanwise grid spacing of $3.13 \times 10^{-2}\,\mathrm{cm}$. Across the small scale features, this gives 20-100 streamwise

Experiment	x_0	$L_x \times L_y \times L_z$	$N_x \times N_y \times N_z$	Boundary Conditions
SD-LSV-FS	2 cm	20 cm × 4 cm × 4 cm	2048 × 128 × 192	Free-slip
SD-LSV-NS	2 cm	20 cm × 4 cm × 4 cm	2048 × 128 × 192	No-slip
LD-LSV-FS	2 cm	40 cm × 4 cm × 4 cm	4096 × 128 × 192	Free-slip
LD-MSV-FS	5 cm	40 cm × 4 cm × 4 cm	4096 × 128 × 192	Free-slip
LD-MSV-NS	5 cm	40 cm × 4 cm × 4 cm	4096 × 128 × 192	No-slip
LD-HSV-FS	10 cm	40 cm × 4 cm × 4 cm	4096 × 128 × 192	Free-slip

Table 3.1: Case name, stratification midpoint, domain size, grid resolution, and boundary conditions for the experiments presented in this thesis.

grid points and 6-32 spanwise grid points per salt finger, depending on its size. $N_z = 192$ grid points are used in the z-direction, which for the no-slip cases gives a maximum vertical grid spacing of 3.29×10^{-2} cm, and a minimum vertical grid spacing of 2.71×10^{-4} cm. For the free-slip cases, this gives a grid spacing of 2.08×10^{-2} cm. In the case names, NS denotes no-slip vertical boundary conditions, while FS denotes free-slip vertical boundary conditions. The midpoint of the stratification, x_0, is set to 2 cm, 5 cm, or 10 cm to observe the effects of different volumes of gravity currents. These are designated LSV, MSV, and HSV in the naming convention for low salt volume, medium salt volume, and high salt volume, respectively. The differences in simulation configurations are summarized in Table 3.1.

3.3 Results

3.3.1 General Flow Development

In this section, salinity isosurfaces at various times are presented for each of the numerical simulations listed in Table 3.1, and the general flow properties of each are described. The similarities and differences between each of the cases are examined in detail in Sections 3.3.2 and 3.3.4.

SD-LSV-NS, $L_x = 20$ cm, $x_0 = 2$ cm

Fig. 3.3 presents isosurfaces of salinity for the 20 cm × 4 cm × 4 cm domain case with no-slip boundary conditions and a stratification midpoint of $x_0 = 2$ cm (experiment SD-LSV-NS).

Because the initially warm, salty water is the less dense of the two layers, it moves along the top of the cool, fresh layer in order to stabilize the density profile. This results in a surface gravity current that moves in the positive x-direction. As the hot, salty current travels the length of the channel, it loses heat to the surrounding fluid through diffusion, while mostly maintaining its salt concentration. The no-slip boundary condition along the top of the domain causes the current head to develop lobe-and-cleft instabilities (Fig. 3.3(b)). The growth of initially two-dimensional horizontal salt fingers is instigated by shear along the bottom of the gravity current (Fig. 3.3(a)). After 12 s, spanwise ripples begin to emerge along the bottom of the current, indicating the initial growth of the salt sheet instability that forms parallel to the primary direction of shear, as discussed by Linden [50] and Kimura and Smyth [43] (see Fig. 3.3(b)). These ripples are the beginning of fully three-dimensional fingers, both from the horizontal 2D fingers growing from the head and rear of the current, as well as rows of fingers sinking from the thin trailing layer of salty water that arises due to the no-slip conditions. As shown in Fig. 3.4, there is also a size disparity between the fingers that emerge closer to the front of the head and fingers that emerge from the wake. There are about four of the larger fingers in the spanwise direction in each of the sets below the head ranging from 0.5 cm to 1 cm wide, and about nine smaller fingers in each of the trailing sets, all roughly 0.2 cm wide. There appears to be some correspondence between the size and locations of the larger fingers and the size and locations of the lobes and clefts in the head, with clefts occurring in line with the separation between each of the fingers, and with each of the lobes being slightly wider than the finger behind it. Both sets of fingers eventually begin to slope down and away from the direction in which the current is travelling. At $t = 15$ s (Fig. 3.3(c)), the large fingers at the front of the current form an angle of about 22° with the top of the domain. By 21 s, this angle has reduced to about 18°.

SD-LSV-FS, $L_x = 20$ cm, $x_0 = 2$ cm

Fig. 3.5 presents isosurfaces of salinity for the 20 cm × 4 cm × 4 cm domain case with free-slip boundary conditions and a stratification midpoint of $x_0 = 2$ cm (experiment SD-LSV-FS). As in the no-slip cases, an initial intrusion of hot, salty water develops above the cool, fresh water. The current head takes the typical shape predicted by inviscid theory [5]. Key differences between this case and the no-slip cases are the lack of a cool, fresh boundary layer between the top boundary and the current, as well as no reduction in speed of the free-slip current front. A similar low salinity intrusion develops in the back of the current as a result of cool fresh water moving to occupy the space left by the warm, salty water. This intrusion experiences some overturning in the wake of the
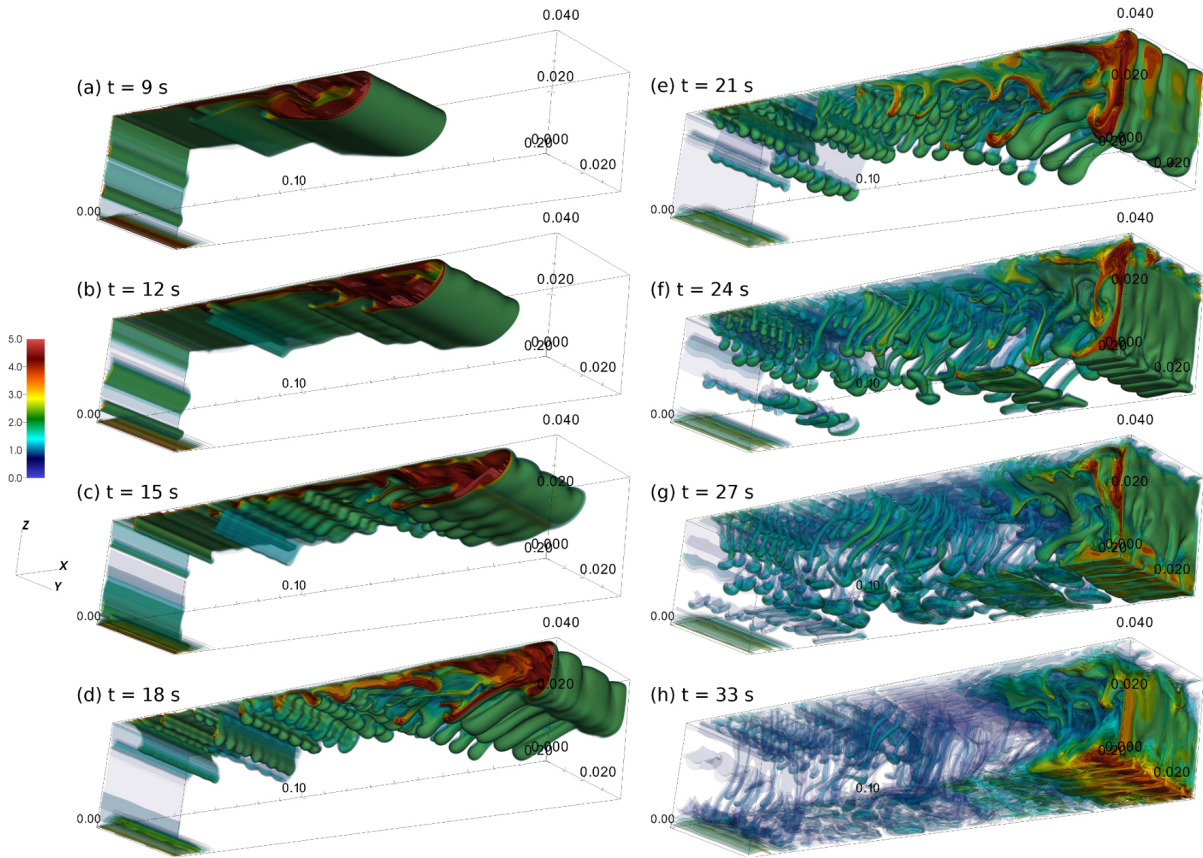
Figure 3.3: Salinity isosurfaces for the short domain simulation with no-slip boundary conditions (SD-LSV-NS) from $t = 9$ s to 33 s. The colour bar indicates the salinity in psu.

0.10 (a)   0.20 (b)
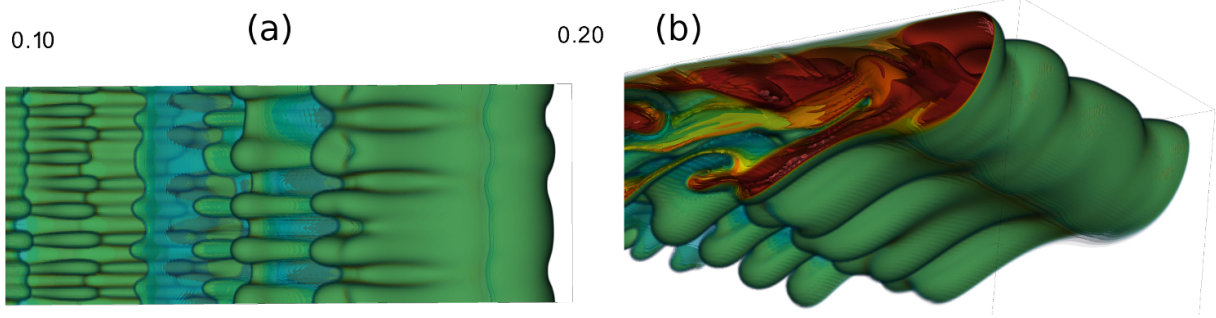
Figure 3.4: Magnified views of salinity isosurfaces for the short domain simulation with no-slip vertical boundary conditions (SD-LSV-NS) at time $t = 17\,\mathrm{s}$ from the bottom (a) and at the current head (b).

current, forming a medium salinity filament from which a horizontal two-dimensional finger eventually emerges (Fig. 3.5(b)). An additional horizontal 2D finger begins to develop from the bottom of the current in its wake. These fingers begin to slope down and to the left of the domain, opposite of the direction in which the current is travelling. The leftmost trailing salt finger displays the first instance of three-dimensionalization occurring around 15 s with the formation of spanwise ripples (Fig. 3.5(d)). These ripples begin to form along each two-dimensional salt finger that emerges from the current, which eventually causes separation into fully three-dimensional fingers (Fig. 3.5(e)). After collision with the right-hand wall, the current maintains enough coherence that it rebounds towards the left side of the tank and travels above any previously-formed fingers (Fig. 3.5(f)). The downward motion of the current at the wall encourages heat loss from the salty water, resulting in a large, two-dimensional, finger-like structure. Additionally, even upon overturning, the current head remains two-dimensional after it collides with the wall and moves leftward. Horizontal fingers stretch rightward from the wake of the current and exhibit spanwise ripples much earlier in their development than the initial fingers (Fig. 3.5(h)). As with previous fingers, these begin to slope down and away from the direction the current is travelling.

LD-LSV-FS, $L_x = 40\,\mathrm{cm}$, $x_0 = 2\,\mathrm{cm}$

Figs. 3.6 and 3.7 present isosurfaces of salinity for the $40\,\mathrm{cm} \times 4\,\mathrm{cm} \times 4\,\mathrm{cm}$ domain case with free-slip boundary conditions and a stratification midpoint of $x_0 = 2\,\mathrm{cm}$ (experiment LD-LSV-FS). This simulation uses an identical initial stratification to case SD-LSV-FS
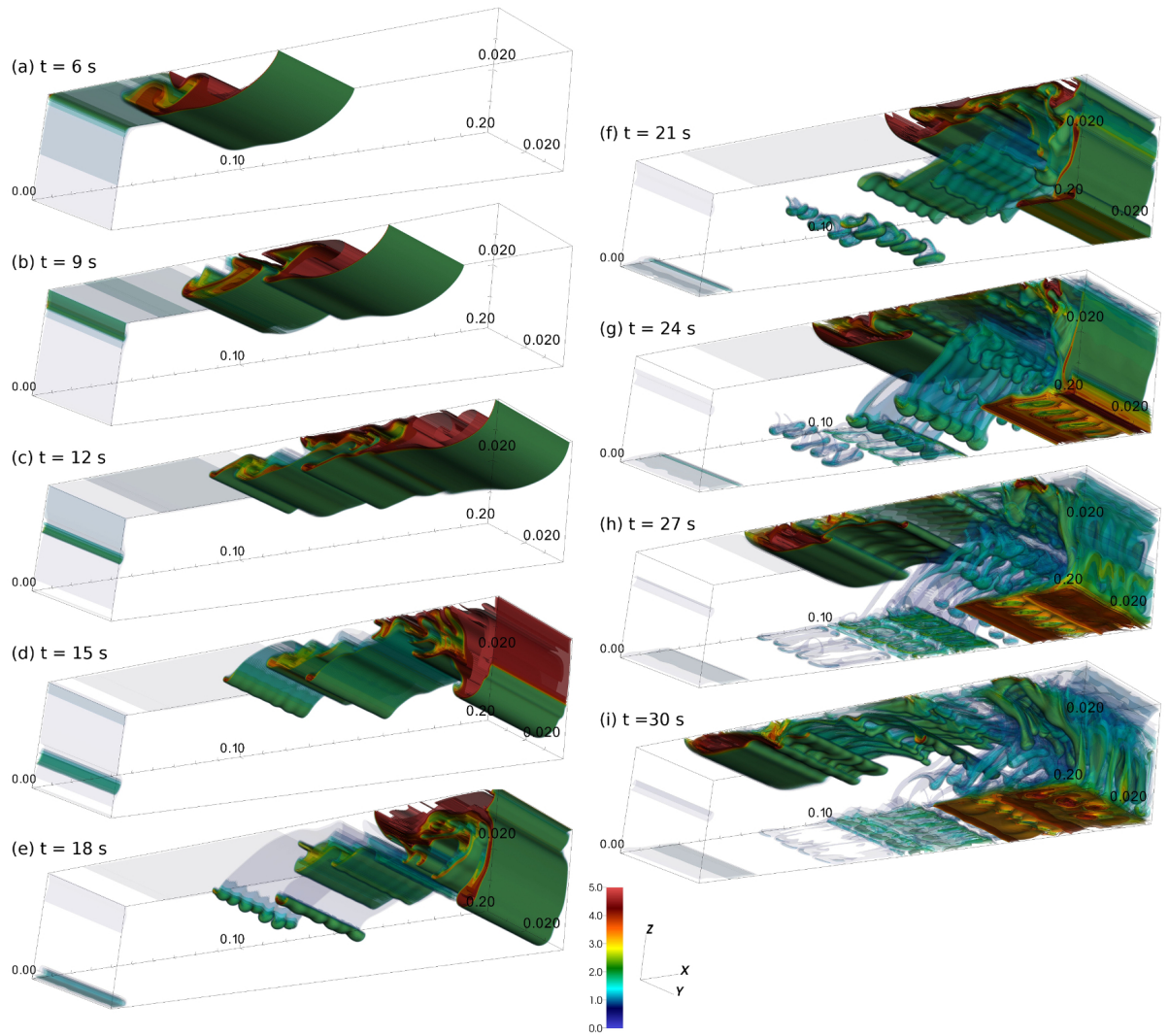
Figure 3.5: Salinity isosurfaces for the short domain experiment with free-slip boundary conditions (SD-LSV-FS) from $t = 6\,\text{s}$ to $30\,\text{s}$. The colour bar indicates the salinity in psu.

with a domain that is twice as long. The resulting flow patterns are identical prior to the encroachment of the short domain case current on the right hand wall around $t = 12$ s. Both the short domain and long domain cases begin to three-dimensionalize around the same time ($t = 15$ s, Fig. 3.6(c)), with spanwise ripples forming along the same leftmost trailing finger. As the current moves rightward, a number of two-dimensional, nearly horizontal fingers emerge from the bottom rear of the current, which all experience spanwise rippling before separating into fully three-dimensional fingers (Fig. 3.6(e)). In each set, there are typically 6 separate spanwise fingers. As the trailing fingers three-dimensionalize, the current head stays two-dimensional, even as it collides with the wall. Since this current has twice as far to travel as the corresponding short domain case, much more salt is lost due to fingering before it collides with the right side of the tank. Upon rebounding, the current has lost enough coherence that it completely breaks apart (Fig. 3.7(k,l)).

LD-MSV-FS, $L_x = 40$ cm, $x_0 = 5$ cm

Figs. 3.8 and 3.9 present isosurfaces of salinity for the 40 cm $\times 4$ cm $\times 4$ cm domain case with free-slip boundary conditions and a stratification midpoint of $x_0 = 5$ cm (experiment LD-MSV-FS). This current initially develops in the same way as the the other flows, with the warm, salty layer moving above the cool, fresh layer. The growth of a horizontal medium salinity finger is instigated by shear along the bottom of the gravity current (Fig. 3.8(a)). Above this finger, there is an intrusion of fresh water into the wake of the current, above which a layer of salty water remains. As the current moves to the right, more horizontal fingers grow from the bottom of the current at the rear (Fig. 3.8(b)). As these fingers begin to sink and slope down and to the left, they develop spanwise ripples which separate into 6 to 7 three-dimensional fingers per spanwise set (Fig. 3.8(c)). Similarly-sized fingers also begin to emerge from the salty layer above the freshwater intrusion, except sloping down and to the right (Fig. 3.8(d)). This is because the salty layer remains mostly stationary, while the fresh intrusion moves rightward. Around $t = 18$ s (Fig. 3.8(e)), larger, primarily spanwise, three-dimensional undulations begin to form near the back of the current. Unlike the smaller trailing fingers, these undulations grow into larger, fully three-dimensional fingers without first separating from a single broad two-dimensional finger. The current head remains two-dimensional during most of the flow, and retains enough coherence that after rebounding off the wall that it continue travelling leftward, despite losing a significant amount of salt. Enhanced development of finger-like structures occurs as the current turns over during its interaction with the wall, and a layer of salt has settled out in the bottom right corner of the domain.
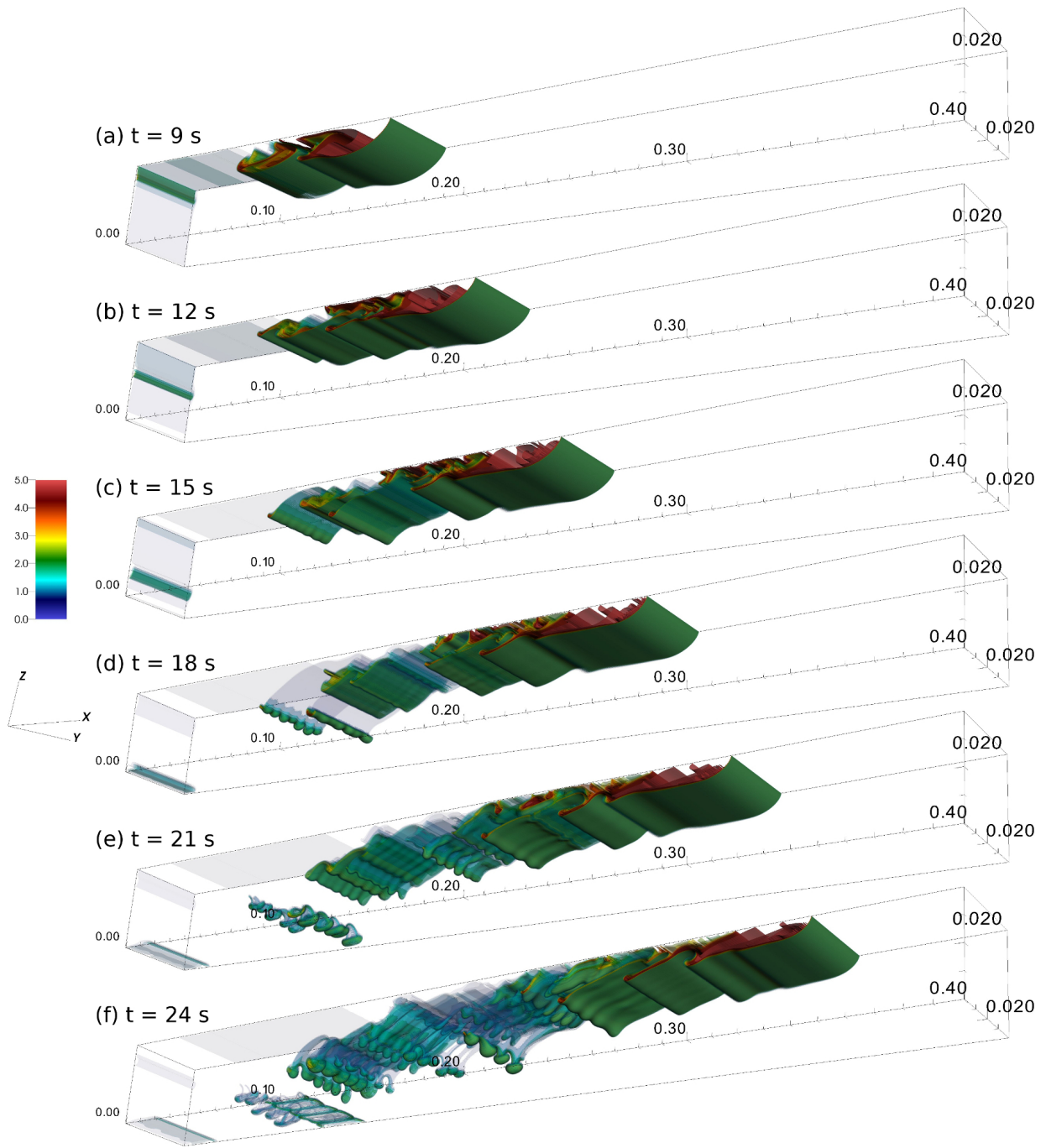
Figure 3.6: Salinity isosurfaces for the long domain experiment with a low initial volume of salty water with free-slip boundary conditions (LD-LSV-FS) from $t = 9\,\text{s}$ to $24\,\text{s}$. The colour bar indicates the salinity in psu.

40
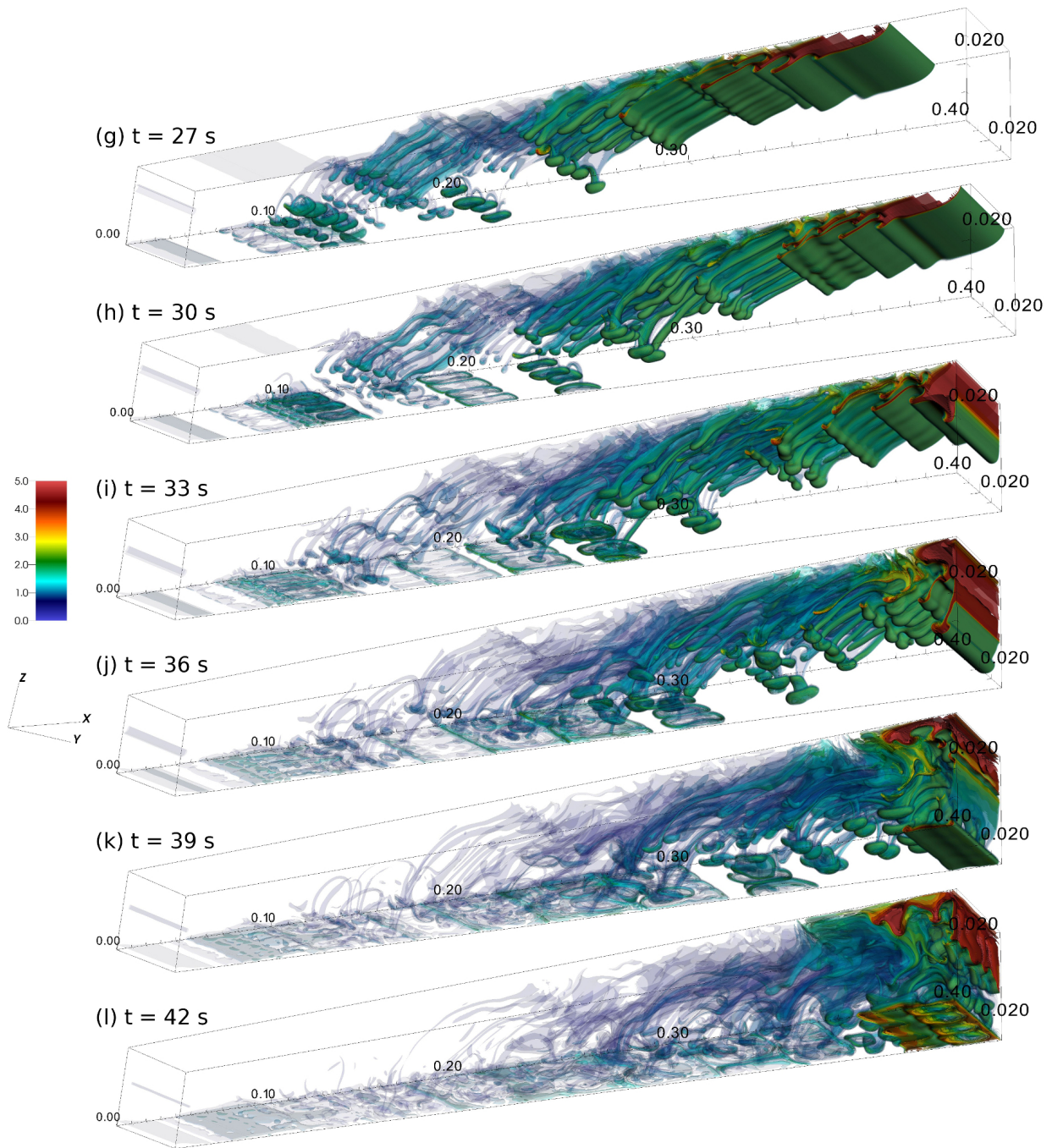
Figure 3.7: Salinity isosurfaces for the long domain experiment with a low initial volume of salty water with free-slip boundary conditions (LD-LSV-FS) from $t = 27\,\mathrm{s}$ to $42\,\mathrm{s}$. The colour bar indicates the salinity in psu.

41
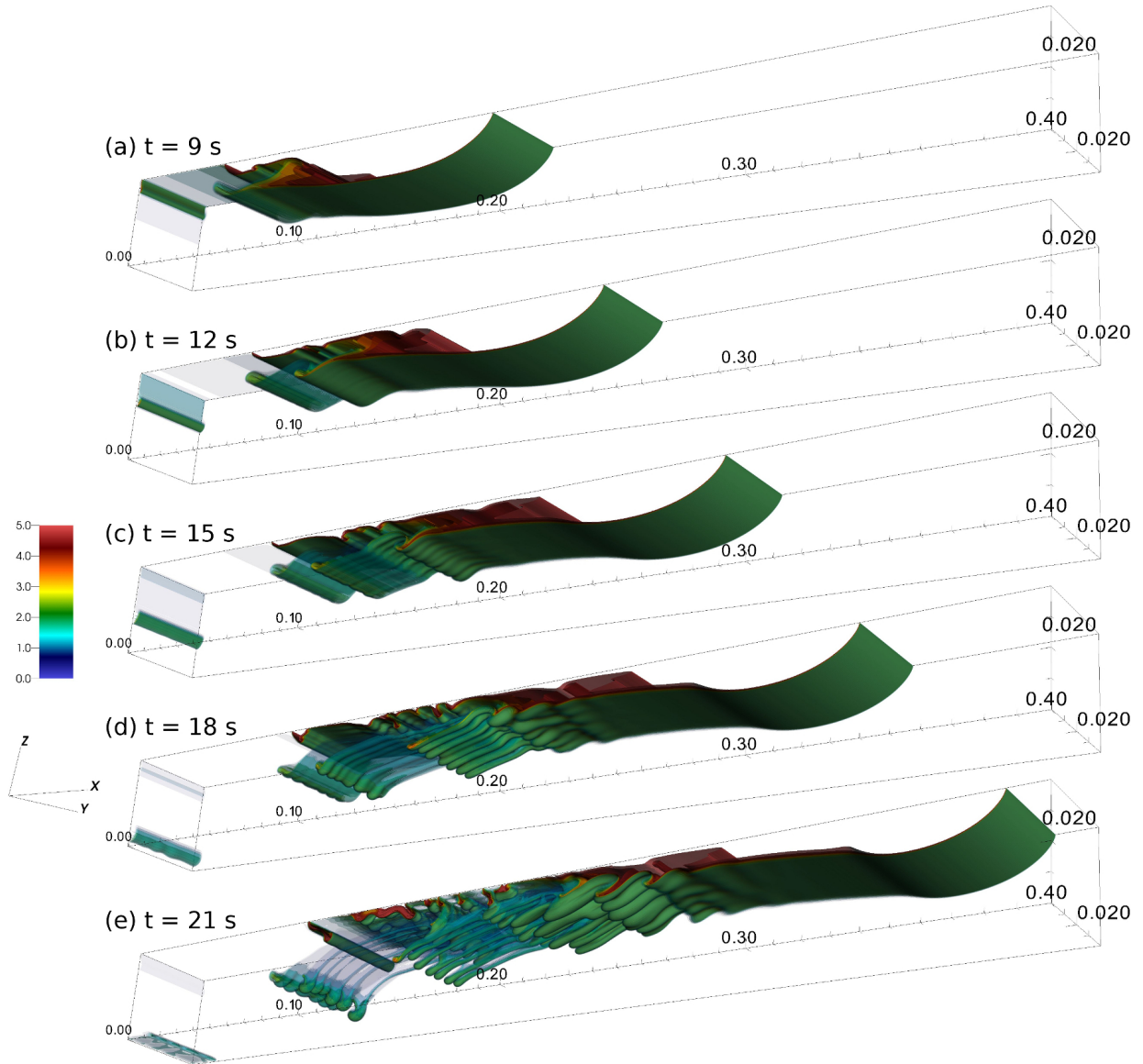
Figure 3.8: Salinity isosurfaces for the long domain experiment with a medium initial volume of salty water with free-slip boundary conditions (LD-MSV-FS) from $t = 9\,\mathrm{s}$ to $21\,\mathrm{s}$. The colour bar indicates the salinity in psu.
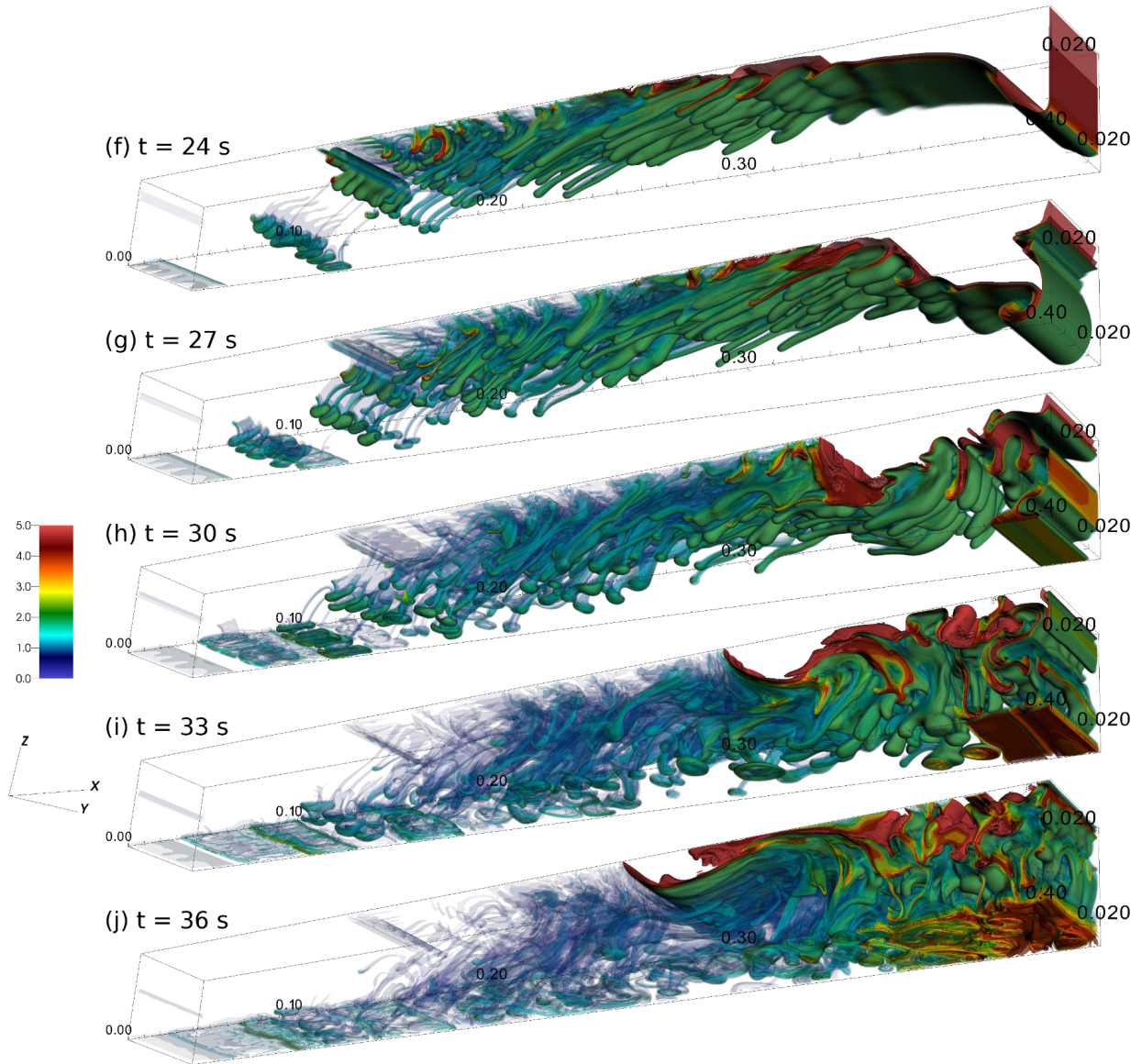
Figure 3.9: Salinity isosurfaces for the long domain experiment with a medium initial volume of salty water with free-slip boundary conditions (LD-MSV-FS) from $t = 24\,\mathrm{s}$ to $36\,\mathrm{s}$. The colour bar indicates the salinity in psu.

LD-HSV-FS, $L_x = 40\,\mathrm{cm}$, $x_0 = 10\,\mathrm{cm}$

Figs. 3.10 and 3.11 present isosurfaces of salinity for the $40\,\mathrm{cm} \times 4\,\mathrm{cm} \times 4\,\mathrm{cm}$ domain case with free-slip boundary conditions and a stratification midpoint of $x_0 = 10\,\mathrm{cm}$ (experiment LD-HSV-FS). This case uses the largest initial mass of salty water of the experiments presented in this section, resulting in the largest surface gravity current. As a result, the current remains largely coherent throughout most of the flow, and exhibits significant two-dimensionality throughout most of the current and towards the head. Again, the head shape resembles the geometry predicted by inviscid theory. As in the other free-slip cases, a horizontal finger that has been initialized by shear begins to peel off along the bottom rear of the current, although the finger takes longer to emerge than in the case LD-MSV-FS (Fig. 3.10(b)). As this finger slopes down and to the left of the domain, spanwise ripples develop that cause it to split into 7 fully three-dimensional fingers (Fig. 3.10(c)). There is also a fresh water intrusion at the back the current that results from cool fresh water moving to fill the space left by the hot, salty current. As the cool intrusion follows the salty current, a layer of salty water remains trapped along the top, causing the formation of salt fingers that slope down and to the right of the domain, in the opposite direction of the fingers forming off the bottom of the current (Fig. 3.10(d)). By $t = 18\,\mathrm{s}$, larger spanwise undulations have begun to develop near the back of the current, as in LD-MSV-FS. As in the previous case, these grow into a set of fingers larger than those that emerge from the initial trailing fingers without developing from an initially two-dimensional instability. Like the smaller trailing fingers, these larger fingers slope down and to the left. After rebounding off the wall, the current retains enough coherence that it manages to continue travelling leftward and reach the left-hand wall. Enough salty water has sunk to the bottom due to fingering and overturning near the right wall that a thin salty layer accumulates along the bottom of the domain.

LD-MSV-NS, $L_x = 40\,\mathrm{cm}$, $x_0 = 5\,\mathrm{cm}$

Fig. 3.12 presents isosurfaces of salinity for the $40\,\mathrm{cm} \times 4\,\mathrm{cm} \times 4\,\mathrm{cm}$ domain case with no-slip boundary conditions and a stratification midpoint of $x_0 = 5\,\mathrm{cm}$ (experiment LD-MSV-NS). As with the short domain no-slip simulation (SD-LSV-NS), this current sees a two-dimensional finger extend horizontally from the back of the current, as well as some of the salty fluid stay trapped along the top of the domain due to the no-slip condition (Fig. 3.12(b)). By $t = 12\,\mathrm{s}$, lobe-and-cleft instabilities have started to form, and there is spanwise rippling along the trailing horizontal finger and the bottom of the current (Fig. 3.12(c)). By $t = 15\,\mathrm{s}$, the rippling along the belly of the current has become quite
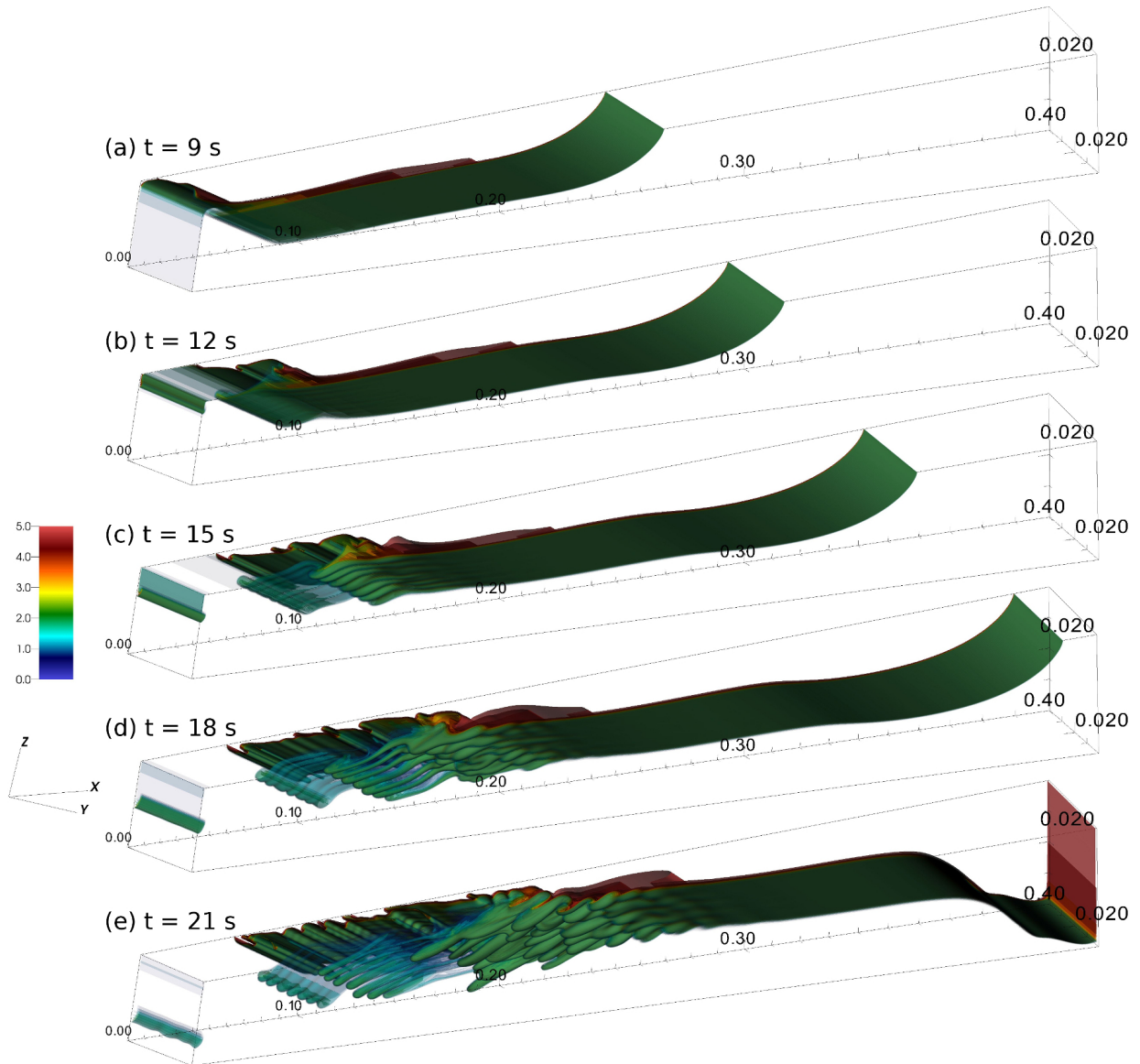
Figure 3.10: Salinity isosurfaces for the long domain experiment with a high initial volume of salty water with free-slip boundary conditions (LD-HSV-FS) from $t = 9\,\text{s}$ to $21\,\text{s}$. The colour bar indicates the salinity in psu.
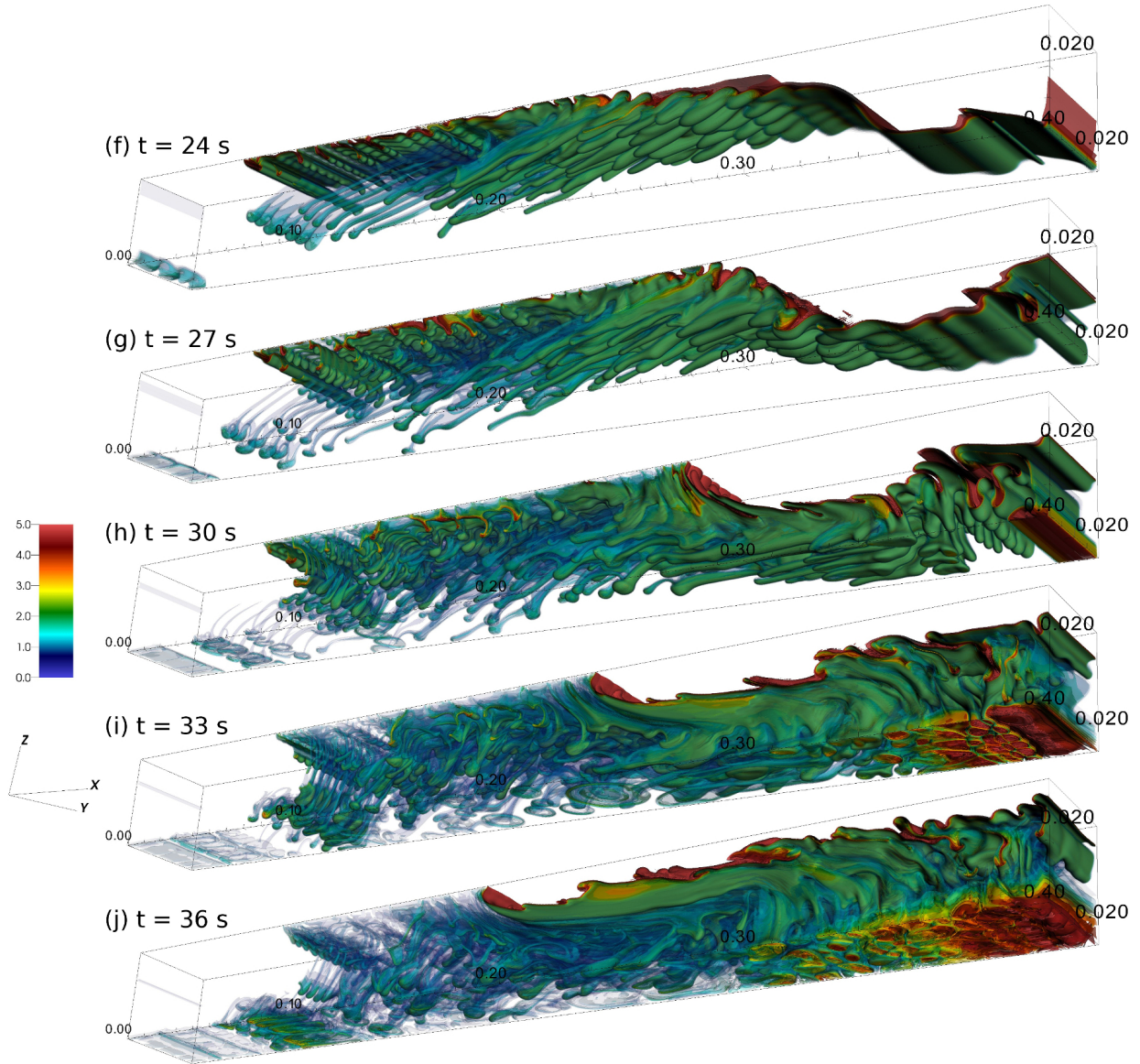
Figure 3.11: Salinity isosurfaces for the long domain experiment with a high initial volume of salty water with free-slip boundary conditions (LD-HSV-FS) from $t = 24\,\text{s}$ to $36\,\text{s}$. The colour bar indicates the salinity in psu.

pronounced, with two sets of fingers beginning to sink out between $x = 11$ cm and 18 cm (Fig. 3.12(d)). Each of these two sets contains about 6 to 7 fingers in the spanwise direction. After $t = 18$ s, the organization of the fingers into distinct sets is much less apparent, as a significant number have emerged between $x = 15$ cm and 21 cm, though it would still appear as if 6 of these fingers fit along the spanwise direction (Fig. 3.12(e)). The fingers emerging from the early 2D horizontal finger and the salty fluid trapped near the top left are smaller in scale, with about 8 to 10 along the spanwise direction. Near the head, the lobe-and-cleft instabilities seem to facilitate the growth of finger-like features, though the shape and size is much more irregular than the belly fingers. As the fingers slope down and away from the direction in which the current is travelling, they begin to stretch, and eventually form bulb-like shapes at their tips (Fig. 3.12(g)).

3.3.2   Vertical Boundary Conditions

Salinity profiles near the spanwise midpoint ($y = 1.98$ cm) are presented for the short domain free-slip case SD-LSV-FS (middle) and no-slip case SD-LSV-NS (right) in Fig. 3.13. The major difference between the two double-diffusive simulations is the shape of the current head. As discussed in Section 3.3.1, the current head in SD-LSV-NS takes on the classical lobe-and-cleft shape. The shape of the head in SD-LSV-FS, however, resembles the geometries predicted by inviscid theory [5] and produced by moving boundary experiments [89, 7]. The tracer profiles intersect the top boundary at right angles in the free-slip case, with no fresh water layer between the salty current and the upper boundary, or spreading of the salty current along the length of the channel. The free-slip case experiences more overturning in the rear of the current. Both double-diffusive cases display initial horizontal two-dimensional fingering from the back of the current. For comparison purposes, an additional simulation without double-diffusion (also called single-diffusive, achieved by setting $\kappa_T = \kappa_s = 3.4 \times 10^{-7} \, \mathrm{m^2/s}$) using the same initial density distribution as the short domain cases and free-slip vertical boundary conditions, is presented in the left column of Fig. 3.13. In the single-diffusive case, the early flow is similar to SD-LSV-FS, as the head takes the same shape, and a similar overturning pattern arises in the back of the current. However, since the tracer diffusivity scales are equal, the current cannot lose any volume due to fingering, and stays coherent as it travels the length of the domain. Additionally, the current stays primarily two-dimensional, with almost imperceptible three-dimensional effects occurring later in the flow.

The developing current is examined in greater detail at $t = 6$ s for the free-slip case SD-LSV-FS in Fig. 3.14, which compares salinity and temperature profiles. The white contour lines indicate regions of higher density ($999 \, \mathrm{kg/m^3}$) inside the sheet and throughout the
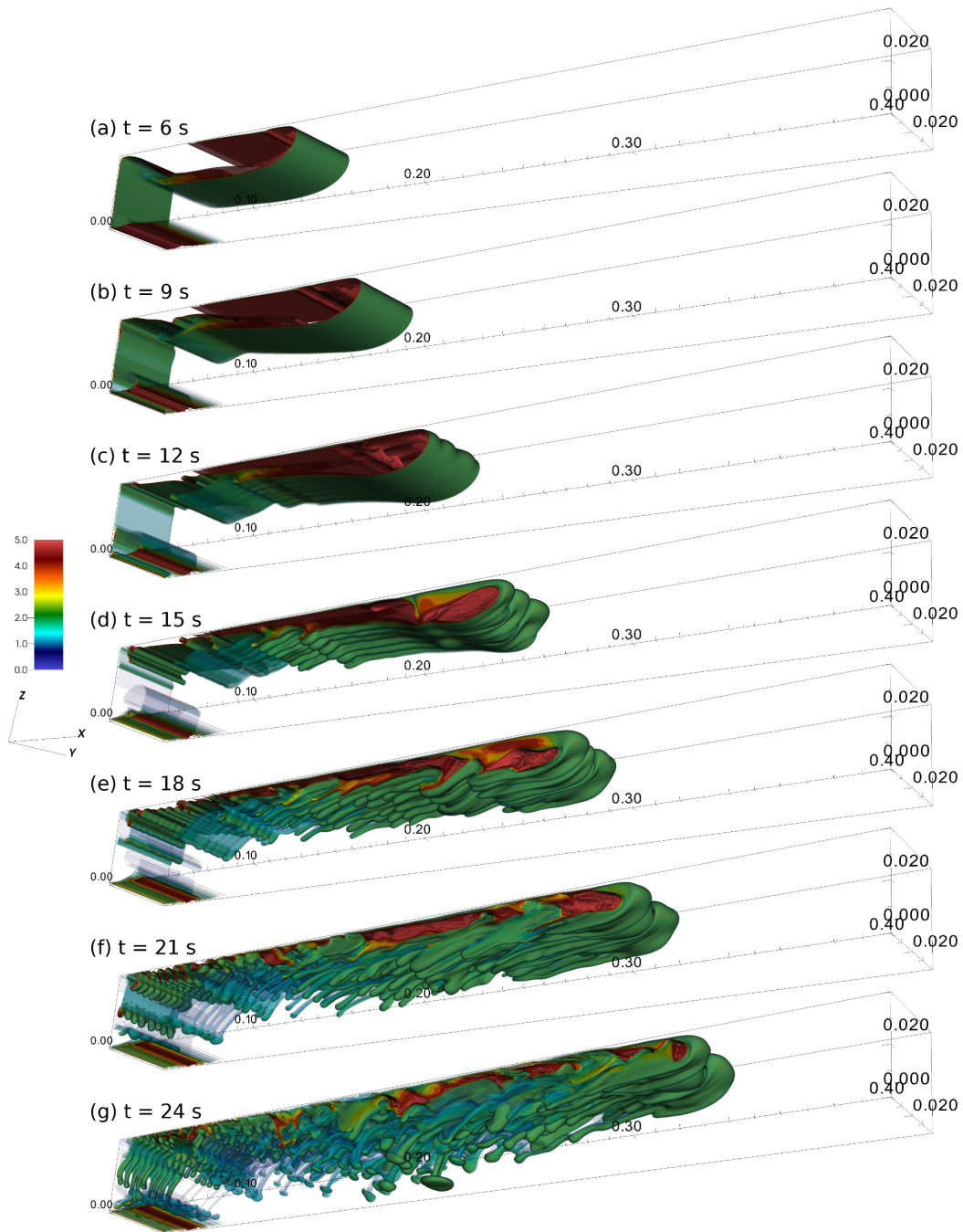
Figure 3.12: Salinity isosurfaces for the long domain experiment with a medium initial volume of salty water with no-slip boundary conditions (LD-MSV-NS) from $t = 6\,\text{s}$ to $24\,\text{s}$. The colour bar indicates the salinity in psu.

48
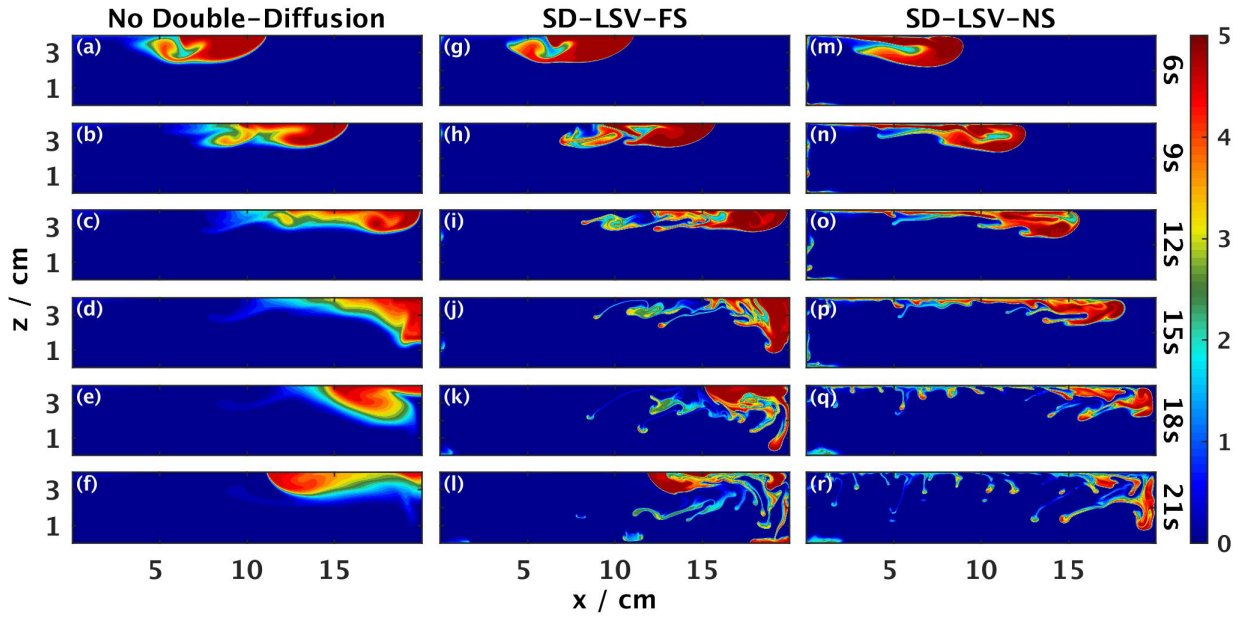
Figure 3.13: Two-dimensional salinity profiles near the spanwise midpoint ($y = 1.98\,\mathrm{cm}$) for the short domain numerical simulations. The left column ((a)-(f)) presents a flow with the same initial and boundary conditions as SD-LSV-FS in the absence of double-diffusive effects (by setting $\kappa_T = \kappa_s = 3.4 \times 10^{-7}\,\mathrm{m}^2/\mathrm{s}$). The middle column ((g)-(l)) presents the double-diffusive simulation with free-slip vertical boundary conditions (SD-LSV-FS), and the right column ((m)-(r)) presents the double-diffusive simulation with no-slip vertical boundary conditions (SD-LSV-NS). The colour bar indicates the salinity in psu.

49
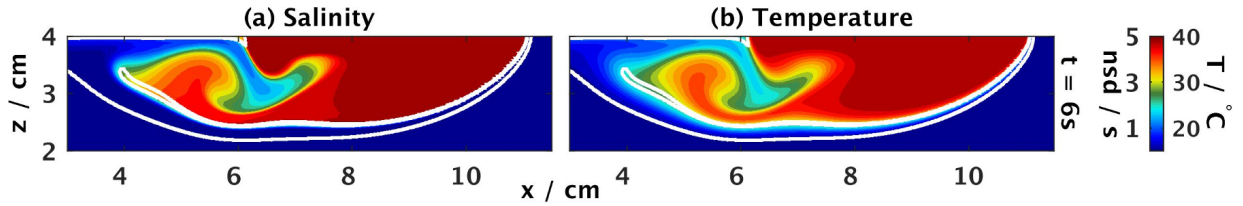
Figure 3.14: Two-dimensional salinity (a) and temperature (b) profiles along $y = 1.98\,\mathrm{cm}$ with density isolines for $\rho = 999\,\mathrm{kg/m^3}$ given in white at $t = 6\,\mathrm{s}$.
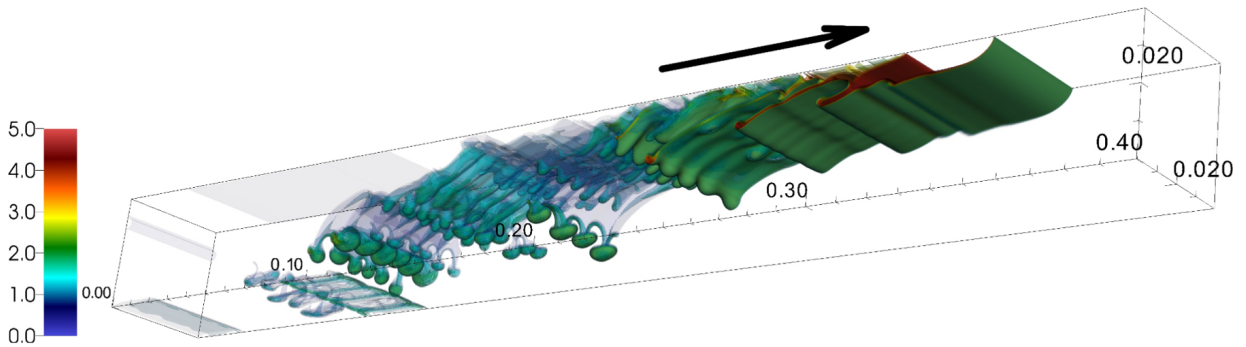
Figure 3.15: Salinity isosurfaces for the free-slip long domain case LD-LSV-FS after 25 s. The direction of flow is indicated by the arrow. The colour bar indicates the salinity in psu.

main mass of cold, fresh water. The relatively high thermal diffusivity causes an increase in temperature in the wake of the salty current, while the low diffusivity of salt prevents the salinity field from spreading. This causes a decrease in density in the surrounding fluid, resulting in the two-dimensional fingers. Over time, the fingers begin to sink and slope down and away from the direction of travel of the head. With time, the shear-induced salt sheets emerge as ripples along the two-dimensional fingers in the spanwise direction, eventually separating into fully three-dimensional fingers. As discussed in Section 3.3.1, larger fingers begin to develop near the front of the head of the no-slip case. These are absent prior to collision with the wall in the free-slip cases, with the current head remaining mostly two-dimensional, as presented by the salinity contours of case LD-LSV-FS in Fig. 3.15. Three-dimensionalization of the flow begins earlier for the no-slip cases than for the free-slip cases, and will be examined further in Section 3.3.5. Additional vertical fingers develop from the thin salty layer formed along the top of the channel by the no-slip conditions, which are not present in the free-slip case.

50

3.3.3 Current Volume

In this section, the effects of varying the initial volume of salty water, and thus the volume of the current, are examined. Simulation LD-LSV-FS (presented at $t = 25\,\mathrm{s}$ in Fig. 3.15) uses an identical density distribution to simulation SD-LSV-FS (discussed in the previous section) with a domain that is twice as long. The resulting flow patterns are identical prior to the encroachment of the SD-LSV-FS current on the right-hand wall around $t = 12\,\mathrm{s}$. Since the LD-LSV-FS current has twice as far to travel, it loses much more salt due to fingering before it collides with the right side of the tank. Unlike the short domain case, the current in the long domain case has lost enough coherence that upon rebounding from the wall, it completely breaks apart. The initial volume of salty water is large enough in cases LD-MSV-FS and LD-HSV-FS, however, that the gravity current maintains much more of its structure as it travels along the streamwise direction. Salinity profiles of these cases along $y = 1.98\,\mathrm{cm}$ are presented in Fig. 3.16. As with the previously-described short domain simulations, a horizontal two-dimensional salt finger emerges near the back of the gravity current, although this finger takes longer to develop as the initial volume of salty water is increased. The bulb of this finger eventually begins to sink, causing it to slope down and away from the direction in which the current is travelling. As the current moves to the right, more horizontal fingers emerge from its wake. Above the initial horizontal finger, there is an intrusion of fresh water into the wake of the current that results from cool, fresh water moving to fill the space left by the hot, salty water. In cases LD-MSV-FS and LD-HSV-FS, as the cool intrusion follows the salty current, a layer of salty water remains trapped along the top. Fingers begin to emerge from this layer that slope down and to the right of the domain. This is opposite to the direction of sloping of the fingers forming off the bottom of the current, due to the rightward moving freshwater intrusion inducing shear in the opposite direction. Both LD-MSV-FS and LD-HSV-FS exhibit a fingering mechanism not observed in the low current volume simulations. Along the bottom of the currents around $t = 18\,\mathrm{s}$ in both cases, three-dimensional undulations emerge that quickly give way to fully three-dimensional fingers. This is in contrast to the primary mechanism of fingering observed in the low volume cases, which involves the formation of two-dimensional fingers that form in the direction of the shear before separating into three-dimensional fingers. The fingers are also larger than those that develop from the initially 2D fingers. Similar large fingers develop along the bottom of the current in the no-slip case LD-MSV-NS.

Once the medium and high volume currents collide with the wall, they retain enough of their volume that they are able to rebound and begin travelling leftward, though both currents lose a significant amount of salt as they overturn due to enhanced development of larger finger-like structures. A layer of high salt concentration has settled in the bottom
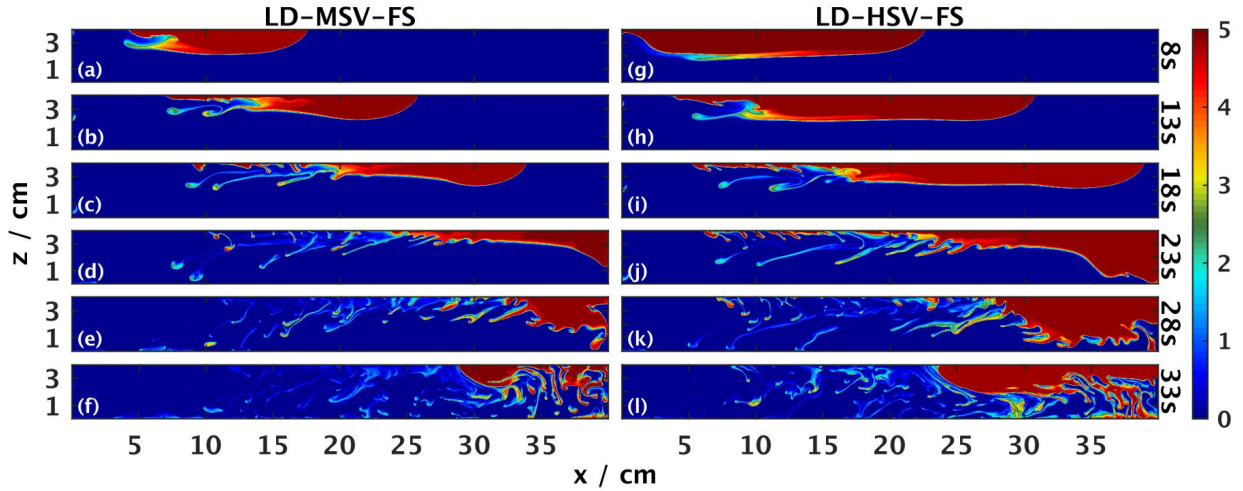
Figure 3.16: Two-dimensional salinity profiles near the spanwise midpoint ($y = 1.98\,\text{cm}$) for cases initialized with medium (LD-MSV-FS, left, (a)-(f)) and high (LD-HSV-FS, right, (g)-(l)) volumes of salty water. The colour bar indicates the salinity in psu.

right corner of the domain. The degree of fingering has also increased in the wake of the current as it travels leftward when compared to the rightward travelling current earlier in the flow.

3.3.4   Current Propagation Speed

In order to analyze the general displacement of the current and its overall propagation speed, the position of the current front was selected as the rightmost instance of salinity above a threshold value of $4.95\,\text{psu}$, prior to collision with the wall. Linear regression was performed on the front position with respect to time, with the resulting slope giving the approximate streamwise propagation speed of the gravity current. Fig. 3.17(a) presents the position of each of the fronts, while Fig. 3.17(b) gives the front position relative to the initial stratification midpoint to better compare displacement between experiments. Free-slip cases SD-LSV-FS, LD-MSV-FS, and LD-HSV-FS all experience a relatively constant change in position, giving an approximately constant propagation speed of $1.70\pm0.02\,\text{cm/s}$. For cases LD-LSV-FS, SD-LSV-NS, and LD-MSV-NS, the front position as a function of time is more nonlinear. SD-LSV-FS and LD-LSV-FS, which have the same initial stratification but different domain lengths, have identical flow patterns prior to the collision of the SD-LSV-FS current with the wall around $t = 12\,\text{s}$. The current in LD-LSV-FS

52
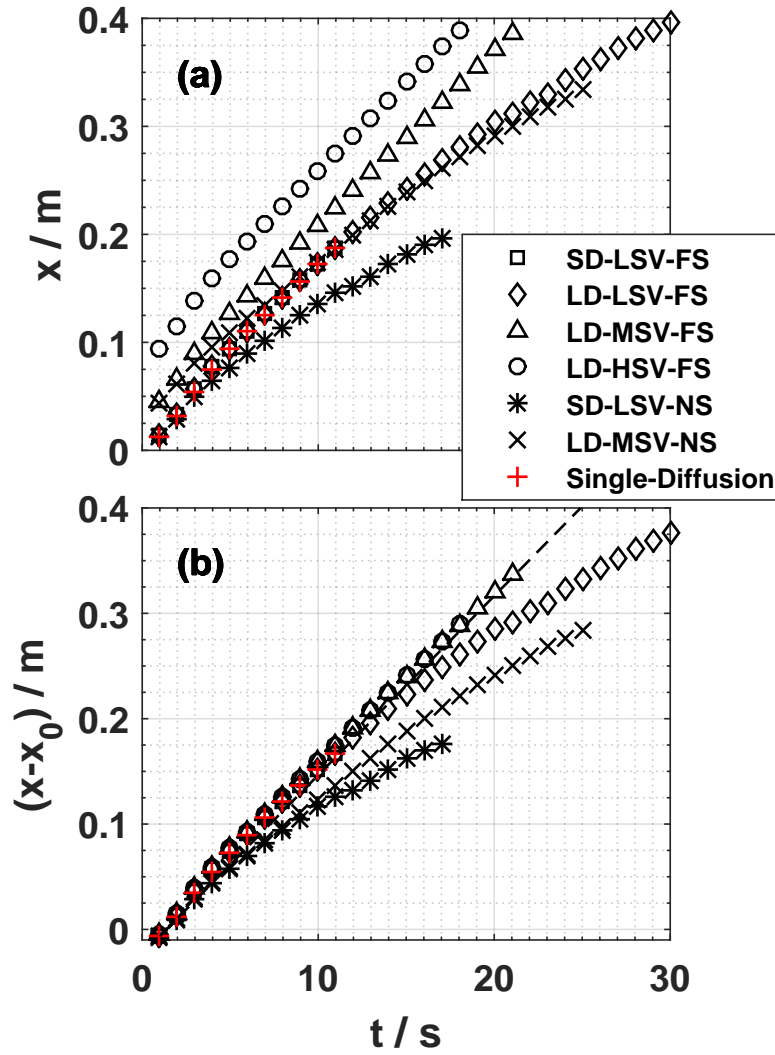
Figure 3.17: Current front position as a function of time (a), and distance of the current front from the density distribution midpoint as a function of time (b) for each of the numerical simulations. The dashed line in (b) has a slope of 1.7 cm/s, for comparison with the average front speeds of the free-slip cases.

travels with the same approximate propagation speed as the other free-slip cases until 11 s, after which the current begins to slow down due to a decrease in salt concentration and coherence of the current. From about $t = 18$ s until just before it collides with the wall around $t = 31$ s, the LD-LSV-FS current moves at approximately 0.97 cm/s in the stream-wise direction. The no-slip cases do not maintain a constant velocity, but instead slow down as they travel the length of the channel. Although there is some overlap in their displacements initially, the small current case SD-LSV-NS travels slower than the medium current case LD-MSV-NS. The front position of the single-diffusion comparison case from Fig. 3.13 was also calculated, showing front positions similar to the other two low volume cases (and thus, displacements similar to all four double-diffusive free-slip cases), with an average propagation speed of 1.70 cm/s. This indicates that, at least at early times, the bulk motion of the free-slip cases is unaffected by fingering.

3.3.5   Three-Dimensionalization, Kinetic Energy, and Dissipation

To characterize the onset time and amount of three-dimensionalization in each simulation, the spanwise standard deviation of salinity,

$$\sigma_y\left(x,z,t\right) = \sqrt{\frac{1}{L_y} \int_0^{L_y} \left(s - \bar{s}\right)^2 \, dy}, \tag{3.3}$$

where $\bar{s}$ is the spanwise mean,

$$\bar{s} = \frac{1}{L_y} \int_0^{L_y} s \, dy, \tag{3.4}$$

was computed numerically at each time step, and then integrated over the streamwise and vertical directions

$$\sigma_y^{\text{Tot}}\left(t\right) = \iint\limits_{[0,L_x]\times[0,L_z]} \sigma_y \, dx \, dz. \tag{3.5}$$

These time series are presented for each simulation in Fig. 3.18(a). In each panel of this figure, the x indicates when the current collides with the wall in each case. The time at which each of the series becomes non-zero indicates when the salinity begins to vary in the spanwise direction, and therefore, when the flow begins to three-dimensionalize. Both no-slip cases first begin to exhibit noticeable three-dimensionalization at about the same time ($t \approx 10$ s), although the medium volume current (LD-MSV-NS) case increases faster and exhibits a greater degree of three-dimensionalization than the small volume current case (SD-LSV-NS). The free-slip cases take longer to exhibit three-dimensional effects than

54

the no-slip cases. Cases LD-MSV-FS and LD-HSV-FS begin to three-dimensionalize at about the same time ($t \approx 15\,\text{s}$), and see a similar initial rate of growth in total standard deviation of salinity. Despite colliding with the right-hand wall relatively early at $t = 12\,\text{s}$, it is still some time before any significant 3D effects develop for SD-LSV-FS. Though the initial growth of total standard deviation of LD-LSV-FS is identical to SD-LSV-FS, the long domain case does three-dimensionalize before hitting the wall. In general, the total degree of three-dimensionalization increases with current volume, while the no-slip cases experience earlier three-dimensionalization at a faster rate and to a greater degree than their free-slip counterparts.

In order to characterize the streamwise regions of three-dimensionalization, the spanwise standard deviation integrated in the vertical direction

$$\sigma_y^{\text{Tot,z}}(x,t) = \int_0^{L_z} \sigma_y \, dz, \tag{3.6}$$

is calculated. Fig. 3.19(a) presents the vertical total spanwise standard deviation as a function of x for the no-slip case SD-LSV-NS at $t = 9\,\text{s}$, $12\,\text{s}$, and $15\,\text{s}$, normalized by the maximum value of the three times. Salinity isosurfaces for this simulation at these times are presented in Fig. 3.3. The position of the current front for each case as defined in Section 3.3.4 is given by a black x. For SD-LSV-NS, the amount of three-dimensionalization is relatively small at $t = 9\,\text{s}$, with a sharp peak occurring near the head of the current at $x = 13\,\text{cm}$, and a smaller, broader peak further back in the current at $x = 11\,\text{cm}$. This three-dimensionalization is imperceptible in the isosurfaces presented in Fig. 3.3. With time, the sharp peak near the current head increases in height as the lobe-and-cleft instabilities develop. At $t = 12\,\text{s}$, the greatest contribution to three-dimensionalization still occurs near the front, although there is some contribution from the salt sheet ripples between $x = 10\,\text{cm}$ and $x = 15\,\text{cm}$. By $t = 15\,\text{s}$, the strongest three-dimensionalization corresponds to the fingers that have begun to emerge from the salt sheet ripples from $x = 12\,\text{cm}$ to $x = 16\,\text{cm}$. The three-dimensionalization at the front has increased from the previous time, but is now weaker than that of the growing fingers. Fig. 3.19(b) presents the vertical total spanwise standard deviation for each case at $15\,\text{s}$. At $t = 15\,\text{s}$, as also indicated in Fig. 3.18, the no-slip cases show a greater degree of three-dimensionalization than the free-slip cases. Additionally, both no-slip simulations exhibit three-dimensional effects at the head, which are absent in the free-slip cases. LD-MSV-FS experiences some three-dimensionalization closer to its current front than LD-HSV-FS. This reflects the volume of each gravity current, since at earlier times the fingers in these cases primarily develop from the back of the currents, resulting in a greater distance between the front and the fingers as current volume increases (see Fig. 3.16).

55
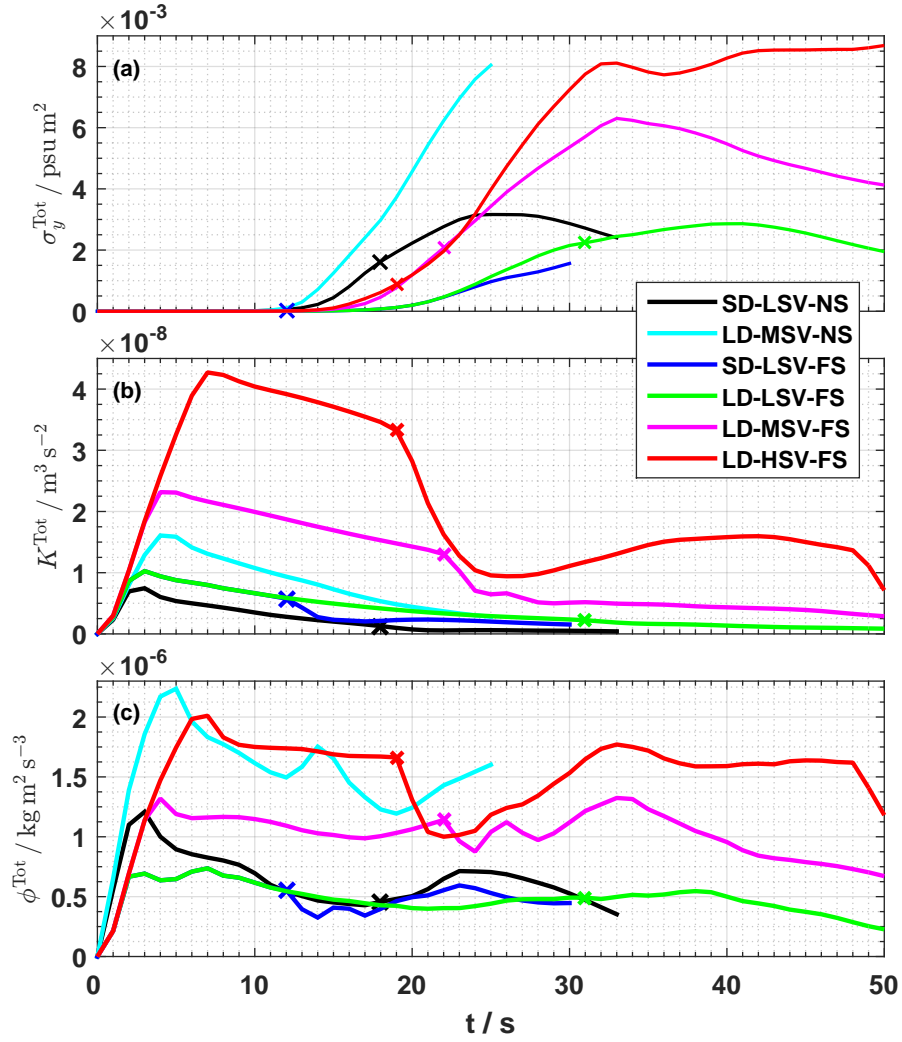
Figure 3.18: (a) The total spanwise standard deviation (SD) of salinity, (b) the total kinetic energy (KE), and (c) the total rate of viscous dissipation for the simulations as labeled in the legend. The time at which each gravity current collides with the wall is indicated by an x that matches the line colour of each simulation.
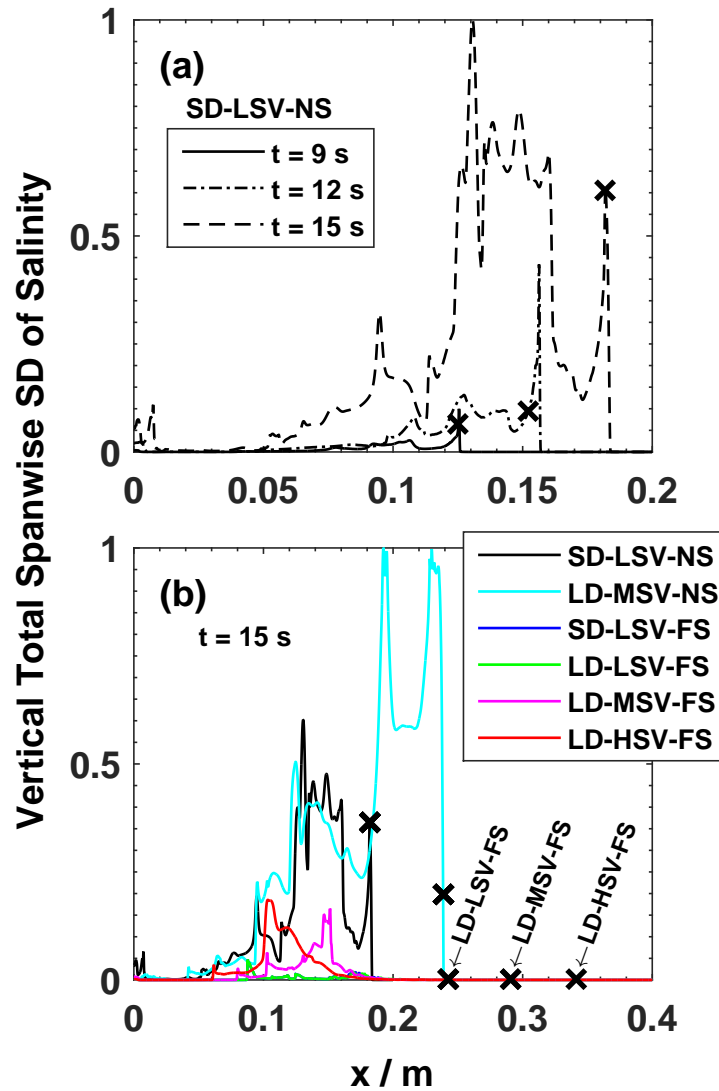
Figure 3.19: The spanwise standard deviation (SD) of salinity integrated vertically as per equation (3.6), (a) for the no-slip case SD-LSV-NS at $t = 9\,$s, $12\,$s, and $15\,$s (normalized by the maximum value of the three times), and (b) for each case at $15\,$s (normalized by the maximum value of all six simulations at $t = 15\,$s). The position of the current front for each simulation is indicated by a black x.

The total kinetic energy (KE) per unit mass (henceforth just kinetic energy),

$$K^{\text{Tot}} = \frac{1}{2} \iiint\limits_V \boldsymbol{u} \cdot \boldsymbol{u} \, dx \, dy \, dz, \tag{3.7}$$

where V is the volume of the domain $[0, L_x] \times [0, L_y] \times [0, L_z]$, is presented as a time series for each simulation in Fig. 3.18(b). The total kinetic energy of each simulation initially increases at approximately the same rate, to a maximum which corresponds to the time at which the entire volume of salty water moves over the fresh water, and the density gradient stabilizes. After that, K^{Tot} begins to decrease at a nearly linear rate. Once the free-slip cases that maintain significant coherence collide with the wall (SD-LSV-FS, LD-MSV-FS, and LD-HSV-FS), there is a steep decrease in kinetic energy as the current moves toward the bottom and loses some of its shape. This decrease is not observed for LD-LSV-FS, as the current has lost most of its volume to fingering prior to colliding with the wall. Only the LD-HSV-FS simulation maintains enough coherence for the total kinetic energy of the system to increase after the gravity current rebounds off the wall. In general, the larger the current, the greater the total kinetic energy. Additionally, the no-slip cases have lower total kinetic energies than the corresponding free-slip cases due to slowing of the current by the vertical boundary conditions.

The total rate of viscous dissipation (hereafter, total dissipation) is computed as

$$\phi^{\text{Tot}} = 2\nu\rho_0 \iiint\limits_V e_{ij}e_{ij} \, dx \, dy \, dz, \tag{3.8}$$

where $e_{ij} = \frac{1}{2}\left(\frac{\partial u_i}{\partial x_j} + \frac{\partial u_j}{\partial x_i}\right)$ is the rate of strain tensor for an incompressible fluid. Fig. 3.18(c) presents the total dissipation for each simulation as a function of time. The dissipation begins to increase similarly to the total kinetic energy, reaching an initial maximum in each case at roughly the same time as the corresponding KE maximum. Both of the no-slip simulations display greater overall total viscous dissipation than the corresponding free-slip cases. In general, each simulation sees a decrease in total dissipation, although both low volume cases see a slightly larger maximum about 4 s after the current initially becomes stably stratified. Both no-slip cases experience a greater drop than the free-slip cases, which experience a slight drop before remaining relatively constant. Upon collision with the right-hand wall, cases SD-LSV-FS and LD-MSV-FS experience small, but rapid, drops in total dissipation, while LD-HSV-FS experiences a much larger drop. After these initial drops, SD-LSV-NS and LD-LSV-FS both continue to increase in dissipation after colliding with the wall. The total dissipation time series of SD-LSV-NS, LD-LSV-FS, LD-MSV-FS,
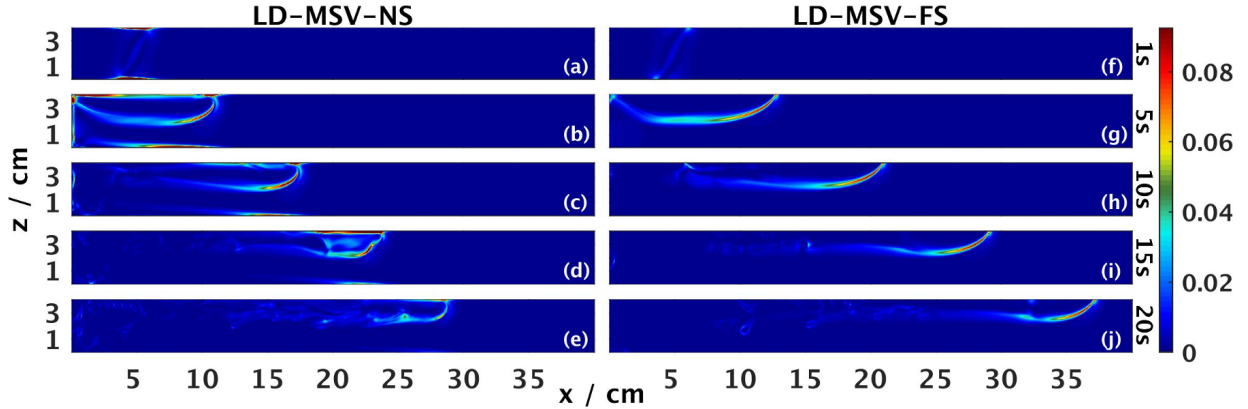
Figure 3.20: Viscous dissipation for LD-MSV-NS (left, (a)-(e)) and LD-MSV-FS (right, (f)-(j)) from $t = 1\,\mathrm{s}$ to $20\,\mathrm{s}$ (top to bottom) along $y = 1.98\,\mathrm{cm}$. The colour bar indicates the viscous dissipation in $\mathrm{kg/m\,s^3}$.

and LD-HSV-FS all display local maxima that correspond fairly well to the maximum total spanwise standard deviation of salinity. In the case of LD-HSV-FS, it corresponds to the first local maximum of the standard deviation, not the maximum value at the end of the simulation. While there is some correlation between the total KE and the total viscous dissipation, there appears to be no relationship between total kinetic energy and the spanwise standard deviation of salinity, as each simulation reaches its maximum K^{Tot} well before significant three-dimensionalization takes place. This indicates that the primary contribution to kinetic energy is due to the formation of the gravity current, and that, in comparison, relatively little kinetic energy is contributed by the three-dimensional instabilities.

Fig. 3.20 compares the viscous dissipation for the no-slip case LD-MSV-NS (left) and free-slip case LD-MSV-FS(right) from $t = 1\,\mathrm{s}$ to $20\,\mathrm{s}$, along $y = 1.98\,\mathrm{cm}$. The no-slip slices indicate several different regions of high dissipation, while the free-slip slices only show strong dissipation along the front of the current. The dissipative regions at the front of the currents are similar in strength for both the no-slip and free-slip cases, while there is significantly stronger dissipation in the boundary layer above the no-slip current (and along the bottom of the domain at early times). At $t = 15\,\mathrm{s}$, there is a significant region of dissipation in the upper boundary layer, which may be responsible for the second local maximum in the total dissipation time series for LD-MSV-NS in Fig. 3.18. Additionally, in the no-slip case, there is a thin region of strong dissipation along the bottom that travels with the current and becomes smaller over time, until it is imperceptible at $t = 20\,\mathrm{s}$.

59

Both cases show regions of relatively weak dissipation that trace outlines of the fingering instabilities.

Fig. 3.21 presents time series of the total viscous dissipation in three different vertical regions. The blue line gives the total viscous dissipation near the lower boundary (between $z = 0 \, \text{cm}$ and $0.25 \, \text{cm}$), the black line gives the total viscous dissipation in the interior of the domain (between $z = 0.25 \, \text{cm}$ and $3.75 \, \text{cm}$), and the red line gives the total viscous dissipation near the upper boundary (between $z = 3.75 \, \text{cm}$ and $4 \, \text{cm}$). These three values are denoted $\phi_{\text{Low}}^{\text{Tot}}$, $\phi_{\text{Int}}^{\text{Tot}}$, and $\phi_{\text{Up}}^{\text{Tot}}$, respectively, and are calculated by first determining the total dissipation in the horizontal directions,

$$\phi_{\text{H}}^{\text{Tot}} (z, t) = \iint\limits_{[0, L_x] \times [0, L_y]} \phi (\boldsymbol{x}, t) \, dx dy, \tag{3.9}$$

then multiplying the horizontal total by a window function defined in terms of z, $W_* (z)$, and integrating in the vertical direction

$$\phi_*^{\text{Tot}} (t) = \int\limits_0^{L_z} W_* (z) \, \phi_{\text{H}}^{\text{Tot}} (z, t) \, dz. \tag{3.10}$$

The three window functions are defined to be 1 in the region of interest, and 0 everywhere else, with a smooth transition between the two regions. The window functions are defined as

$$W_{\text{Low}} (z) = \frac{1}{2} - \frac{1}{2} \tanh \left(\frac{z - 0.25 \, \text{cm}}{0.05 \, \text{cm}} \right), \tag{3.11}$$

for the lower region,

$$W_{\text{Up}} (z) = \frac{1}{2} + \frac{1}{2} \tanh \left(\frac{z - 3.75 \, \text{cm}}{0.05 \, \text{cm}} \right), \tag{3.12}$$

for the upper region, and

$$W_{\text{Int}} (z) = 1 - W_{\text{Up}} (z) - W_{\text{Low}} (z) \tag{3.13}$$

for the interior of the domain. In the resulting time series presented in Fig. 3.21(a), where each regional contribution to dissipation is divided by the total contribution to dissipation at a given time, the interior of the vertical domain is the primary contributor to the total dissipation. Initially, most of the dissipation is contributed in equal parts from the lower and upper regions, as in Fig. 3.20(a), which shows thin regions of high dissipation near the upper and lower boundaries near $x = 5 \, \text{cm}$ due to the initial horizontal density distribution

moving to form the gravity current. As the current develops, the greatest contribution to dissipation comes from the interior. Both the contributions from near the upper and lower boundaries generally decrease with time, though the relative contribution from the upper region increases around $t = 15\,\text{s}$, at which point there is a slight decrease in the interior contribution. This corresponds to the long strip of high dissipation seen in the upper boundary of the current head in Fig. 3.20(d).

It is reasonable to expect that most of the viscous dissipation would be in the interior of the domain, given that, as defined, the interior region (between $z = 0.25\,\text{cm}$ and $3.75\,\text{cm}$) comprises 87.5% of the total vertical domain. However, since the lower and upper regions each comprise 6.25% of the vertical domain, these regions proportionally contribute more to the total dissipation. This is shown in Fig. 3.21(b), which displays the mean contribution in the vertical direction (per cm) to the total dissipation over each of the regions. The mean total dissipation over the interior region increases slowly until about $t = 4\,\text{s}$, where it remains fairly consistent around $3.75 \times 10^{-7}\,\text{kg}\,\text{m}^2\,\text{s}^{-3}/\text{cm}$. Both of the means over the upper and lower regions increase at the same rate until $t = 2\,\text{s}$. The lower region reaches its maximum of about $1.8 \times 10^{-6}\,\text{kg}\,\text{m}^2\,\text{s}^{-3}/\text{cm}$ at $t = 3\,\text{s}$, and decreases steadily afterwards, becoming lower than the mean over the internal region at $t = 17\,\text{s}$. The mean over the upper region reaches its maximum of about $2.3 \times 10^{-6}\,\text{kg}\,\text{m}^2\,\text{s}^{-3}/\text{cm}$ at $t = 5\,\text{s}$, and decreases until $t = 11\,\text{s}$, after which it increases and reaches a second maximum of about $1.75 \times 10^{-6}\,\text{kg}\,\text{m}^2\,\text{s}^{-3}/\text{cm}$ at $t = 14\,\text{s}$, before it decreases again. Over the entire simulation period, the mean contribution to dissipation in the upper region is signifcantly stronger than the mean contribution in the interior region.

To examine the regions of greatest viscous dissipation, $\phi = 2\nu\rho_0 e_{ij}e_{ij}$, around the fingers, Fig. 3.22 presents a $2\,\text{psu}$ salinity isosurface in grey and a $9.1 \times 10^{-3}\,\text{kg/m}\,\text{s}^3$ viscous dissipation isosurface in red (which is 4% of the maximum value of dissipation) for the no-slip experiment LD-MSV-NS at $t = 20\,\text{s}$. This figure indicates that there is dissipation primarily along the fronts and sides of the fingers, with negligible dissipation along the backs. The amount of dissipation around the fingers increases and surrounds more of each individual finger moving toward the front of the current, while the thinner fingers near the back show negligible dissipation in the surrounding areas.

3.3.6 Stirring and Mixing

The stirring and mixing of salinity (as defined by equation (2.40)) along a slice near the spanwise midpoint of the domain ($y = 1.98\,\text{cm}$) at $t = 20\,\text{s}$ are presented for the free-slip case LD-MSV-FS in Fig. 3.23, and for the no-slip case LD-MSV-NS in Fig. 3.24. These images present a magnified view of the regions of primary stirring and mixing.
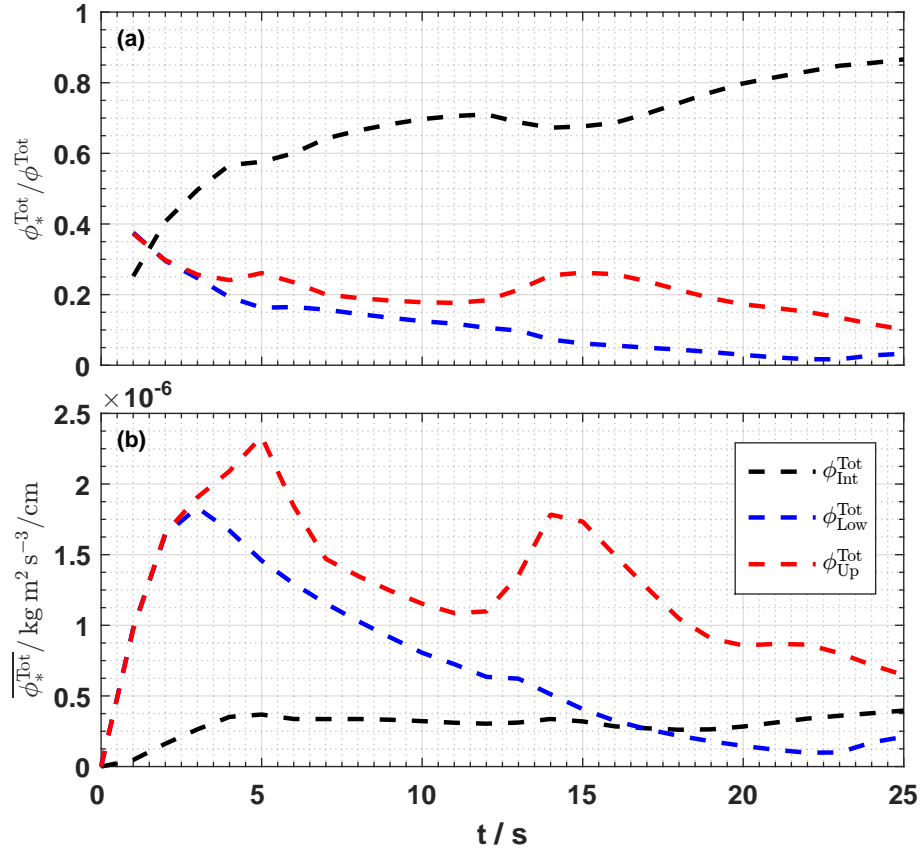
Figure 3.21: Total viscous dissipation between $z = 0\,\text{cm}$ and $0.25\,\text{cm}$ (blue line), $z = 0.25\,\text{cm}$ and $3.75\,\text{cm}$ (black line), and $z = 3.75\,\text{cm}$ and $4\,\text{cm}$ (red line), as a function of time, (a) normalized by the total viscous dissipation at each time. The vertical mean of the total viscous dissipation over each of the three regions is presented in panel (b).
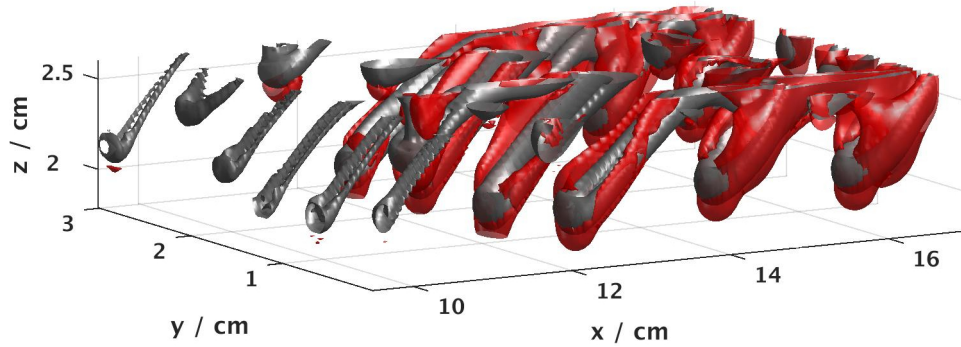
Figure 3.22: 2 psu salinity isosurface in grey for the no-slip case LD-MSV-NS at $t = 20\,\mathrm{s}$, with a viscous dissipation isosurface in red for $\phi = 9.1 \times 10^{-3}\,\mathrm{kg/m\,s^3}$.
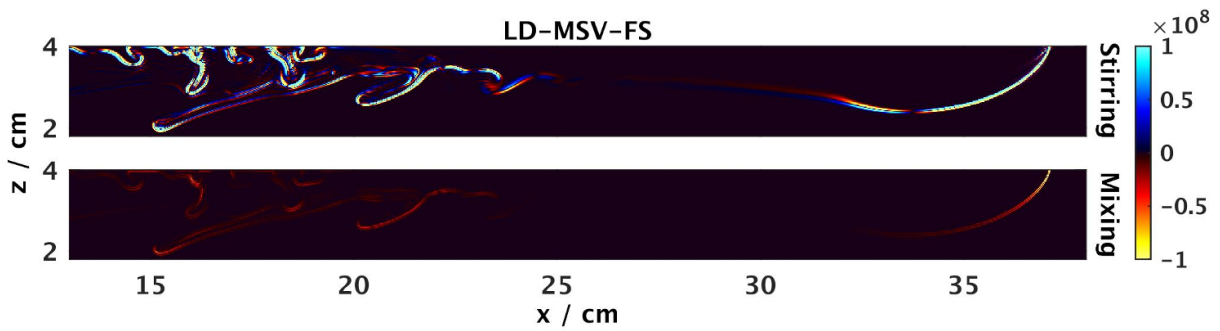
Figure 3.23: Stirring (top) and mixing (bottom) of the salinity field of simulation LD-MSV-FS along $y = 1.98\,\mathrm{cm}$ at $t = 20\,\mathrm{s}$ in units of $\mathrm{psu^2/m^2s}$.
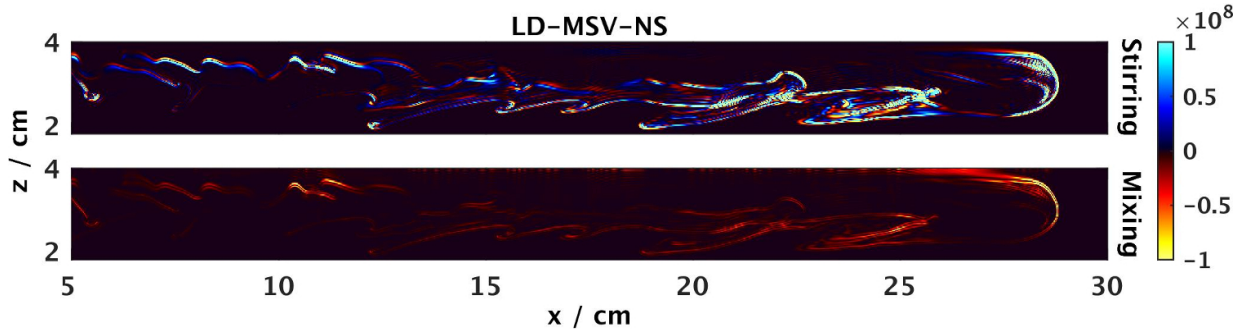
Figure 3.24:   Stirring (top) and mixing (bottom) of the salinity field of simulation LD-MSV-NS along $y = 1.98\,\text{cm}$ at $t = 20\,\text{s}$ in units of $\text{psu}^2/\text{m}^2\text{s}$.

The free-slip case experiences strong stirring of the salinity field along the current head and around the fingers trailing from the back of the current, with almost no stirring along the belly of the current. While there is some mixing around the fingers at the back of the current, the strongest mixing occurs near the very front of the current head. The strength of the stirring and mixing around the fingers of the no-slip case appears to be similar to the stirring and mixing around the fingers of the free-slip case. There is strong stirring and mixing at the top front of the current head, in the region where the lobes and clefts have developed. In both cases, the regions of strongest mixing typically correspond to the regions of strongest stirring. Overall, the strength of the stirring is significantly greater than the strength of the mixing. The temperature stirring and mixing for the no-slip case LD-MSV-NS are presented in Fig. 3.25. Both fields outline the fingers and the current head, similar to the salinity stirring and mixing, although there are no small scale features of alternating positive and negative stirring or strong mixing. Each of the mixing regions appears to correspond to the regions of non-zero stirring. Additionally, there is a patch of strong mixing above the head around $x = 27.5\,\text{cm}$, which corresponds to very weak stirring. This suggests that the transport of heat is primarily due to thermodynamic effects in that region and not the motion of the fluid.

Fig. 3.26 presents the absolute value of the mixing of salinity integrated in the vertical and spanwise directions as a function of the streamwise variable at $t = 15\,\text{s}$ (dashed line) and $20\,\text{s}$ (solid line) for the free-slip case LD-MSV-FS (a) and the no-slip case LD-MSV-NS (b). The position of the current front, as defined in Section 3.3.4, is identified at each time by a black x. The plots are normalized by the maximum of the absolute value of total mixing for both cases and times (i.e., the minimum of LD-MSV-FS at $t = 20\,\text{s}$, since mixing is always negative). At both $t = 15\,\text{s}$ and $20\,\text{s}$, the free-slip case shows the highest values
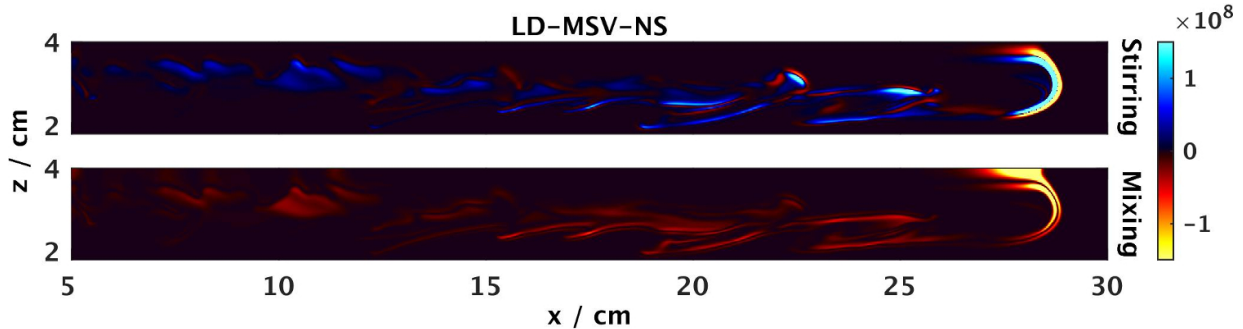
Figure 3.25: Stirring (top) and mixing (bottom) of the temperature field of simulation LD-MSV-NS along $y = 1.98\,$cm at $t = 20\,$s in units of $°C^2/m^2$s.

of localized mixing about 3 cm behind the front of the current as defined by Section 3.3.4, with the local mixing near the front at $t = 15\,$s comprising about 90% of the local mixing near the front at $t = 20\,$s. This corresponds to the region of strong mixing that traces the front of the current, as shown in Fig. 3.23. Both times show a rapid decrease in total mixing moving towards the back of the current, with imperceptible mixing along the current belly, and increased mixing at the back of the current due to fingering. At $t = 15\,$s, there is relatively weak mixing (typically below 5% of the maximum) between $x = 8\,$cm to 15 cm, with a localized peak of mixing (about 10% of the maximum) at $x = 7.9\,$cm. At $t = 20\,$s, the length of this mixing region (from $x = 8\,$cm to 24 cm) has more than doubled, and a significant number of localized peaks are visible, with the largest reaching about 25% of the maximum. In this region, the mixing is typically greater than at least 2% of the maximum.

The no-slip case, at both $t = 15\,$s and 20 s, shows strong mixing in two peaks just ahead of the front of the current as defined by Section 3.3.4. There is more mixing near the front of the current at $t = 15\,$s (55% of the maximum) than at $t = 20\,$s (40% of the maximum). The decrease in mixing is less rapid moving towards the back of the current for the no-slip case than for the free-slip case. Between $x = 0\,$cm and 19 cm, the mixing at $t = 15\,$s is typically below 5% of the maximum, with strong localized peaks occuring at $x = 0\,$cm (25% of the maximum), 0.5 cm (30% of the maximum), and 7 cm (15% of the maximum), among other places. At $t = 20\,$s, the no-slip case shows relatively strong mixing from $x = 13\,$cm to 30 cm, where the mixing is always greater than 5% of the maximum. The greatest localized mixing occurs near $x = 1\,$cm, and is about 47% of the maximum. Between $x = 1\,$cm and 6 cm, there are a number of localized peaks ranging from 5% to 13% of the maximum. Though the free-slip case exhibits localized regions of stronger mixing

65

than the no-slip case near the front, overall, the no-slip case exhibits greater total mixing than the free-slip case at corresponding times.

3.4   Summary

Through high-resolution DNS, double-diffusive gravity currents were simulated, and the effects of boundary conditions and current volume on flow development were characterized. In particular, it was observed that:

1. Current heads exhibit the typical lobe-and-cleft and inviscid theory patterns when under the effects of no-slip and free-slip boundary conditions, respectively.

2. Two-dimensional salt fingers develop in the primary direction of the shear near the bottom of the wake of the currents. These fingers eventually experience spanwise rippling due to the shear-induced salt sheet instability, leading to fully three-dimensional salt fingers.

3. The no-slip currents also experience the growth of a set of larger-scale fingers near the front of the current head. These fingers are absent from the free-slip cases, where the head remains mostly two-dimensional. The fingers near the head are typically about 2 to 3 times the spanwise width of the fingers that trail from the back of the current.

4. Larger volume currents retain enough coherence that upon colliding with the far wall, they rebound and begin to flow back toward their starting point. If the current volume is small enough with respect to the domain, the salt fingering may cause the current to lose enough mass that it breaks down.

5. In each of the free-slip simulations, the gravity current was observed to move with nearly the same propagation speed, which was the same for a single-diffusive free-slip simulation.

6. The onset of three-dimensionalization occurs earlier and faster for the no-slip cases than for the free-slip cases. There is also an increase in the amount of three-dimensionalization with the volume of the current. Similar trends are observed for the total viscous dissipation.
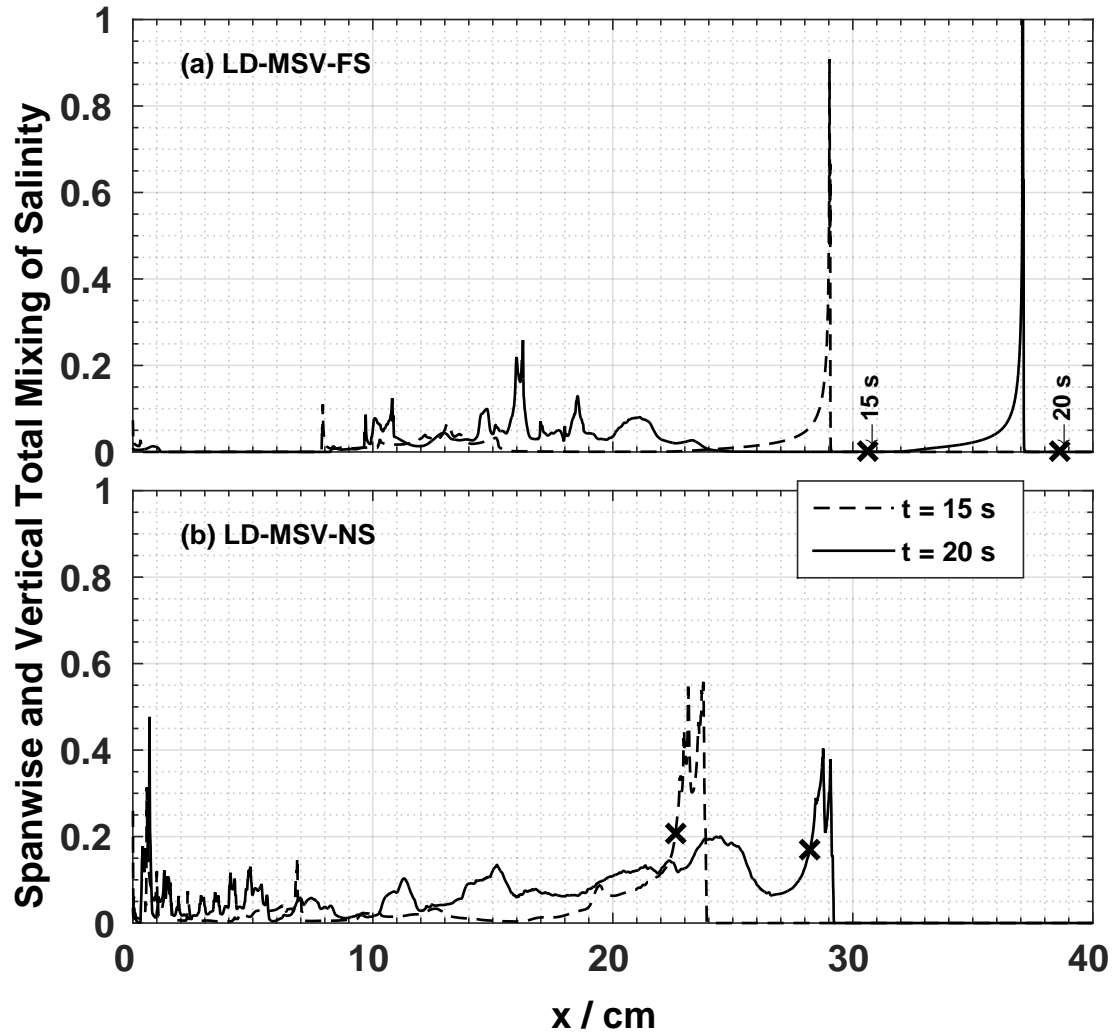
Figure 3.26: The total mixing of salinity integrated in the spanwise and vertical directions for (a) the free-slip case LD-MSV-FS and (b) the no-slip case LD-MSV-NS at $t = 15\,\text{s}$ (dashed line) and $20\,\text{s}$ (solid line), normalized by the maximum value for both cases and times. The position of the current front at each time is indicated by a black x.

7. Both the free-slip and no-slip cases exhibit regions of high dissipation that trace the fronts of the currents, as well as regions of lower dissipation about the salt fingers. The strongest dissipation in the no-slip cases is seen in the upper boundary layer.

8. Due to the lobe-and-cleft instabilities about the current head and the additional fingering along the entire current, the no-slip simulation LD-MSV-NS experiences an overall greater degree of stirring and mixing when compared to the corresponding free-slip case. The profiles of salinity stirring and mixing feature structures that are more fine scale than those of the temperature stirring and mixing.

Chapter 4

Double-Diffusive Rayleigh Taylor Instabilities

4.1 Rayleigh-Taylor Instabilities

The salt fingering experiments of Jevons were likely influential in later research performed by Lord Rayleigh. Unpublished laboratory notebooks indicate that he and Eleanor M. Sidgwick had attempted to replicate these experiments [85]. He would later attempt to explain the observed phenomenon mathematically through linear stability analysis [52], although he ignores viscous effects completely and assumes the instability is due to an unstable density stratification. Based on his analysis, he concludes that in a fluid that is stratified in two layers, if the upper layer of fluid is heavier than the lower layer, then the interface of the two fluids will become unstable. Subsequent analysis by Taylor [99] determined that in the event that the two layers are in a stable configuration, if the fluid is accelerated downward at a rate greater than the acceleration due to gravity, then instabilities will also form along the interface of the two layers. In the experimental companion paper by Lewis [49], it was observed that the amplitude of the instabilities initially grew as predicted by the first-order approximation derived by Taylor. The paper presents the first experimental results of what are now referred to as Rayleigh-Taylor instabilities.

Recently, double-diffusion has been suggested as a mechanism which may be responsible for enhanced sedimentation rates in sedimenting flows [67, 13]. In stably-stratified systems with a layer of sediment-laden, fresh water over a layer of clear, salty water, two different instability mechanisms may develop. The first is the sediment analog to salt fingers in a typical double-diffusive system, where salt diffuses more rapidly than sediment into the

upper layer, increasing its density and causing fingers. The second, called settling-driven convection, is due to sediment settling across the pycnocline, increasing the density of the upper region of salty fluid, which then sinks in the form of Rayleigh-Taylor instabilities [32, 13]. Green [23] established a relationship between the double-diffusive flux and the settling flux to determine whether fingers or settling convection would dominate. Burns and Meiburg [9] performed linear stability analysis to further explore the nature of the mechanisms behind particle sedimentation from buoyant river plumes. It was noted that in an entirely freshwater system with a layer of sediment-laden water above clear water, the development of Rayleigh-Taylor instabilities along the pycnocline was increasingly impeded by larger particle settling velocities. When the density field is stabilized by adding salt to the lower layer, it was determined that the nature of the instability is governed by a relationship between the unstable layer thickness (i.e., the salty region into which particles initially settle and destabilize) and the thickness of the salinity interface due to diffusion. If the unstable layer thickness is less than or similar to the salinity interface thickness, double-diffusion is important. If the unstable layer is thicker than the salinity interface, then Rayleigh-Taylor instabilities dominate. This work was later extended using nonlinear two- and three-dimensional DNS [10]. In a series of experiments involving silicon carbide grinding powder and salt, Davarpanah Jazi and Wells [13] observed that for $R_\rho > 1.2$, settling-driven convection was the dominant mechanism.

In the aforementioned references, the dominance of Rayleigh-Taylor instabilities does not necessarily preclude the occurrence of double-diffusive effects, as the density still depends on two tracers with different diffusivities. Since there are no settling velocities to drive Rayleigh-Taylor instabilities in a stably-stratified purely double-diffusive system, the this research examines the development of a Rayleigh-Taylor instability along an unstable pycnocline where the density difference is due to both temperature and salinity gradients. This chapter examines a three-dimensional high-resolution direct numerical simulation of a double-diffusive Rayleigh-Taylor instability arising from a three-layer density stratification. Visualizations of the various flow fields are presented and discussed. An eddy diffusivity parameterization for the temperature, salinity, and density fields is attempted, and determined to be inappropriate for the flow presented here. Fourier analysis of each of the fields is performed to further examine the dominant scales, and the resulting information is used to filter different length scales from the density field.

4.2 Mathematical Formulation

Like gravity currents, Rayleigh-Taylor (henceforth RT) instabilities develop due to the interaction of two masses of fluids of different densities. Unlike gravity currents, RT instabilities are a result of the buoyancy force acting in the same direction as the density gradient. The most basic example of such a configuration would be a layer of dense fluid over top of a layer of less dense fluid. The simulation presented in this chapter considers an initial setup with two pycnoclines: a lower pycnocline, across which density and temperature are stably-stratified, but salinity is unstably-stratified, and an upper pycnocline, across which density and temperature are unstably-stratified, but salinity is stably stratified, as presented in Fig. 4.1. This stratification is expected to form primarily RT instabilities along the upper pycnocline, while the lower pycnocline should produce salt fingers.

Jacobs and Dalziel [36] performed experiments examining Rayleigh-Taylor instabilities developing from a similar three-layer density stratification, where the stratification along the upper pycnocline is unstable, and the stratification along the lower pycnocline is stable. Although their stratification is much like the one described in Fig. 4.1, the simulation presented here is complicated by the presence of two diffusive tracers. The authors observed that in the event that the upper layer and lower layer have the same density, there is little penetration (or erosion) of the lower layer by the RT instabilities. This is attributed to the fact that the fluid remains stably stratified at the lower interface, even when impacted by the RT instabilities. Piacsek et al. [70] performed 2D numerical simulations of three-layer double-diffusive systems to examine the mechanics of flow inside interleaving layers of hot and cold water. Their initial density profile was stable, with conditions favourable to salt fingering along the upper interface, and oscillating instabilities along the lower interface. From a similar perspective, the simulation presented here could be considered a small region of three interleaving layers of water resulting from thermohaline intrusions, in a regime where horizontal shear is not important.

Before proceeding with the equations of the initial stratification, it is important to note that, in this chapter, a modification will be made to the governing equations. Because of the way SPINS organizes blocks of memory along the x-direction, it is convenient when simulating domains that have long vertical extents, but narrow horizontal domains, to treat the x-direction as vertical. As such, equation (2.1) becomes,

$$\frac{\partial \boldsymbol{u}}{\partial t} + \boldsymbol{u} \cdot \boldsymbol{\nabla} \boldsymbol{u} = -\frac{1}{\rho_0} \boldsymbol{\nabla} p - g \frac{\rho}{\rho_0} \delta_{i1} + \nu \nabla^2 \boldsymbol{u}, \qquad (4.1)$$

indicating that buoyancy acts in the negative x-direction. For $\boldsymbol{u} = (u, v, w)$, u is the vertical
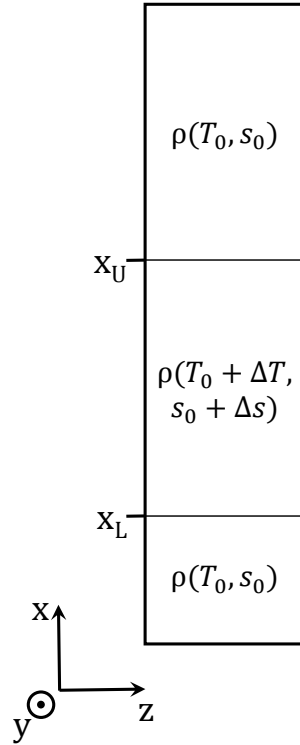
Figure 4.1: Two-dimensional sketch of the initial conditions of the simulation presented in this chapter, with x indicating the vertical direction, and the y-direction pointing out of the page. In this simulation, $\rho\left(T_0, s_0\right) > \rho\left(T_0 + \Delta T, s_0 + \Delta s\right)$, while $T_0 < T_0 + \Delta T$ and $s_0 < s_0 + \Delta s$, indicating that there is less dense, warm, salty fluid between two layers of denser, cold, fresh fluid. Along $x = x_U$, the density field is unstably stratified, while the density is stably stratified along $x = x_L$, though conditions are favourable for salt finger formation.

component of velocity, while v and w are the horizontal components of velocity. As in the gravity current simulations of Chapter 3, the thermal and salinity diffusion coefficients are $\kappa_T = 3.4 \times 10^{-7}\,\mathrm{m^2/s}$ and $\kappa_s = 2 \times 10^{-8}\,\mathrm{m^2/s}$, giving dimensionless parameters $\mathrm{Pr} = 5.88$, $\mathrm{Sc} = 100$, and $\tau = 5.88 \times 10^{-2}$.

The initial stratification is defined using a linear combination of hyperbolic tangent functions, set by

$$T\left(\boldsymbol{x}, t = 0\right) = T_0 + \frac{\Delta T}{2}\left(\tanh\left(\frac{x_U - x}{\Delta x}\right) - \tanh\left(\frac{x_L - x}{\Delta x}\right)\right),\tag{4.2}$$

and

$$s\left(\boldsymbol{x}, t = 0\right) = s_0 + \frac{\Delta s}{2}\left(\tanh\left(\frac{x_U - x}{\Delta x}\right) - \tanh\left(\frac{x_L - x}{\Delta x}\right)\right).\tag{4.3}$$

As in Chapter 3, T_0 and s_0 refer to the temperature and salinity of the cold, fresh fluid. $x_L = 2\,\mathrm{cm}$ and $x_U = 6\,\mathrm{cm}$ indicate that the transition from the bottom layer of cold, fresh fluid to the intermediate layer of hot, salty fluid occurs at $2\,\mathrm{cm}$, and that the hot, salty fluid transitions to the upper layer of cold, fresh fluid at $6\,\mathrm{cm}$. Δx defines stratification width, set to $0.1\,\mathrm{cm}$. As in Chapter 3, the warm, salty water has an initial density of $995.91\,\mathrm{kg/m^3}$, while the density of the cool, fresh water is initially $999.12\,\mathrm{kg/m^3}$, giving a density difference of $3.21\,\mathrm{kg/m^3}$. This gives an Atwood number of $\mathrm{A} = 1.61 \times 10^{-3}$, suggesting symmetric penetration by both the bubbles and the spikes (i.e., the rising and falling RT instabilities, respectively).

Equations (2.36) and (2.37), can be used to determine estimates of the most unstable wavelength, λ_{RT}, and corresponding growth rate, σ_{RT}, of the RT instabilities developing along $x = 6\,\mathrm{cm}$. Using the above parameters for the simulations presented in this chapter, $\lambda_{\mathrm{RT}} = 0.795\,\mathrm{cm}$ and $\sigma_{\mathrm{RT}} = 2.497\,\mathrm{s^{-1}}$. Similarly, from equations (2.25) and (2.26), the wavelength of the fastest-growing salt fingers, λ_{SF}, and corresponding initial growth rate, σ_{SF}, along the lower pycnocline at $x = 2\,\mathrm{cm}$ can be computed. Since $(T, s) = (27.5°\mathrm{C}, 2.5\,\mathrm{psu})$ at $x = 2\,\mathrm{cm}$ initially, and using linear approximations to the temperature (2.32) and salinity (2.33) derivatives at that height, this gives a density ratio of $R_\rho = 1.9$, and therefore $\lambda_{\mathrm{SF}} = 0.283\,\mathrm{cm}$ and $\sigma_{\mathrm{SF}} = 0.358\,\mathrm{s^{-1}}$. This implies that the RT instabilities along the upper interface will develop significantly faster than the salt fingers along the lower interface.

4.3   Single-Diffusive Rayleigh-Taylor Instabilities

In the event that the density difference across the layers only depends on a single tracer gradient, the sharpness of the density interfaces are set by the diffusivity of that tracer.

Fig. 4.2 presents density contours of three different RT instabilities developing from the same initial density stratification, with the densities of the lighter fluid and heavier fluid set to $995.91\,\mathrm{kg/m^3}$ and $999.12\,\mathrm{kg/m^3}$, respectively, but where the density stratification is due only to a temperature gradient ((a)-(b)), to a salinity gradient ((c)-(d)), and to gradients in both temperature and salinity ((e)-(f)). Using initial conditions (4.2) and (4.3), in the left column, salinity is kept constant at $s = 0$, while $T_0 = 15\,^\circ\mathrm{C}$ and $\Delta T = 14.2015\,^\circ\mathrm{C}$. In the middle column, temperature is kept constant at $T = 40\,^\circ\mathrm{C}$, while $s_0 = 9.3548\,\mathrm{psu}$ and $\Delta s = -4.3548\,\mathrm{psu}$. The right column presents a density stratification that is due to both variable salinity and temperature fields, with the temperature of the warm water set to $T_0 = 15\,^\circ\mathrm{C}$, a change in temperature between layers of $\Delta T = 25\,^\circ\mathrm{C}$. The salinity of the salty layer is $s_0 = 0$, with a change in salinity of $\Delta s = 5\,\mathrm{psu}$. Each of the simulations displays similar rising mushroom-like parcels of low density fluid moving upwards from near the upper pycnocline, while the lower pycnocline remains stable and flat. The primary difference between the temperature-only and salinity-only simulations is the steepness of the gradients between the high density fluid and the low density fluid. The pycnoclines of the temperature-only simulation are much broader than the pycnoclines of the salinity-only simulation, since the diffusivity of temperature is higher than that of salt. At $t = 9\,\mathrm{s}$, the double-diffusive case displays thin alternating regions of low and high density outlining the RT instabilities. This is also visible in the lower pycnocline, where a thin layer of high-density fluid rests between a layer of slightly lower density fluid below, and the original low density layer above. These alternating layers of high and low density are typical of double-diffusive flows, and will be discussed later in this chapter. They will henceforth be referred to as double layers. By $t = 11\,\mathrm{s}$, the lower pycnocline in the T- and s-only cases shows a small degree of additional diffusion, while the double layer in the double-diffusive case begins to show some oscillations, suggesting the initial stages of salt fingers. Meanwhile, the RT instabilities in the T-only case appear to be larger in scale than the instabilities in the s-only case, which display a number of fine filaments. The double-diffusive case shows larger scale RT instabilities on roughly the same scale as the T-only case, which are outlined by thin layers of alternating high and low density fluid.

This double layer along the double-diffusive interface is similar to the double-boundary layer described by [51, 20, 11], with one important difference. Those papers were concerned with stable density stratifications with cold, fresh water above hot, salty water. As the lighter cool, fresh fluid gains heat, it experiences a decrease in density above the thermohaline interface, while the heavier, hot, salty layer loses heat, causing an increase in density just below the interface. This is in contrast to the simulation presented here, where the lighter, hot, salty layer loses heat to the heavier, cool, fresh layer. Along the interface, this causes an increase in density in the salty layer, and a decrease in density
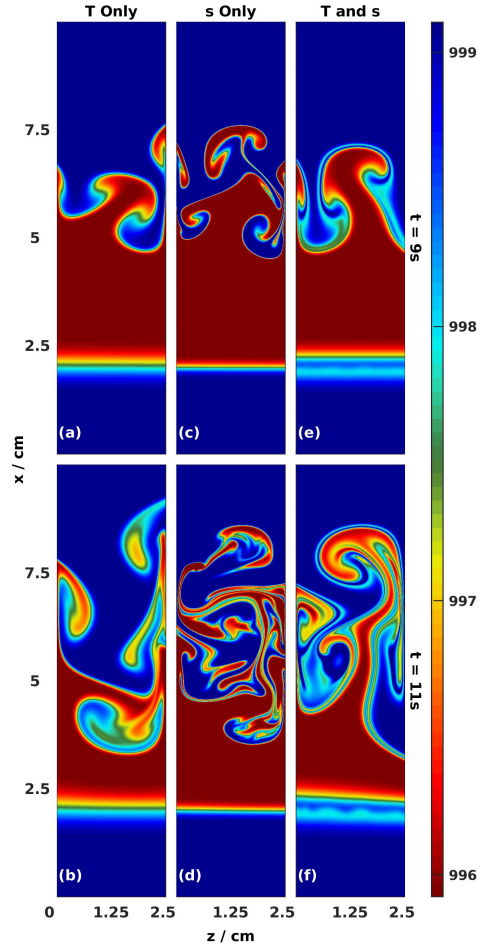
Figure 4.2: Density profiles of 2D Rayleigh-Taylor simulations where the density gradient depends on only temperature ((a)-(b)), only salinity ((c)-(d)), and both temperature and salinity ((e)-(f)), after 9 s (top) and after 11 s (bottom). The colour bar indicates the density in kg/m³.
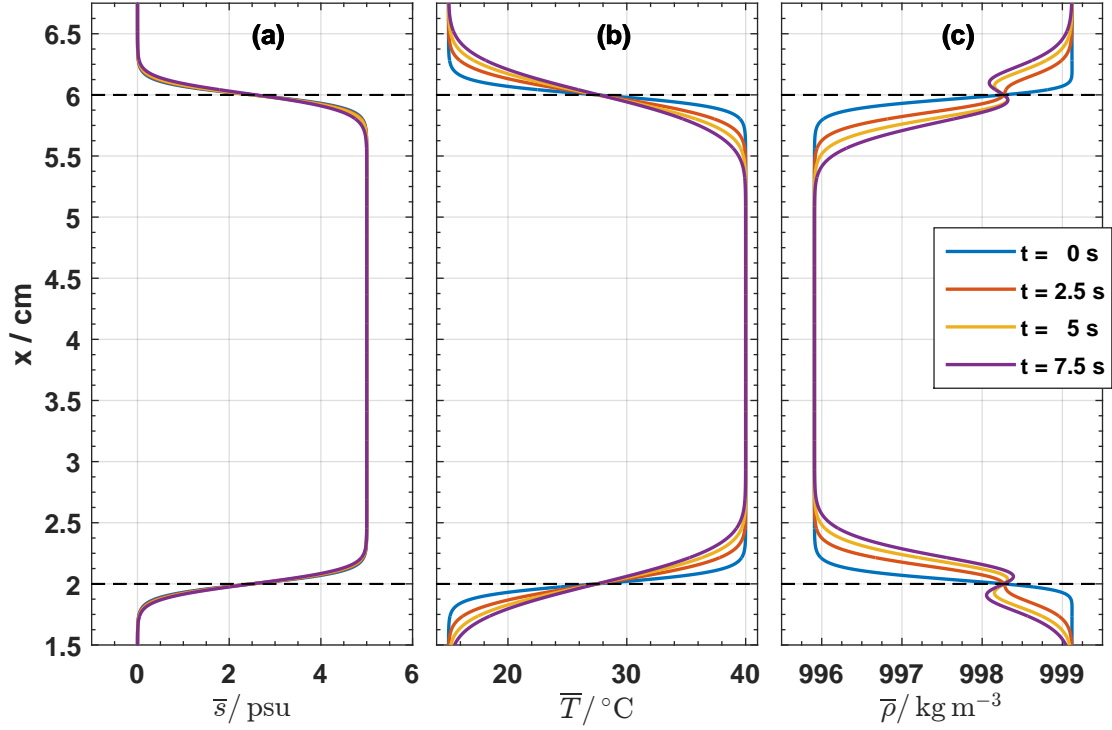
Figure 4.3: Horizontal means of (a) salinity, (b) temperature, and (c) density as a function of x. The dashed lines along $x = 2 \, \text{cm}$ and $6 \, \text{cm}$ indicate the initial locations of the pycnoclines.

in the fresh layer. Fig. 4.3 illustrates the formation of this double layer, presenting the horizontally-averaged salinity, temperature, and density of the 3D simulation presented in this chapter, as a function of the vertical position. Over the first $7.5 \, \text{s}$ of the simulation, the salinity interfaces display negligible diffusion, while the higher thermal diffusion causes an increase in the width of the temperature interface, increasing (decreasing) the temperature just below (above) $x = 2 \, \text{cm}$, and just above (below) $x = 6 \, \text{cm}$. The resulting double layers are visible in Fig. 4.3(c) at $t = 2.5 \, \text{s}$, $5 \, \text{s}$, and $7.5 \, \text{s}$ along $x = 2 \, \text{cm}$ and $6 \, \text{cm}$.
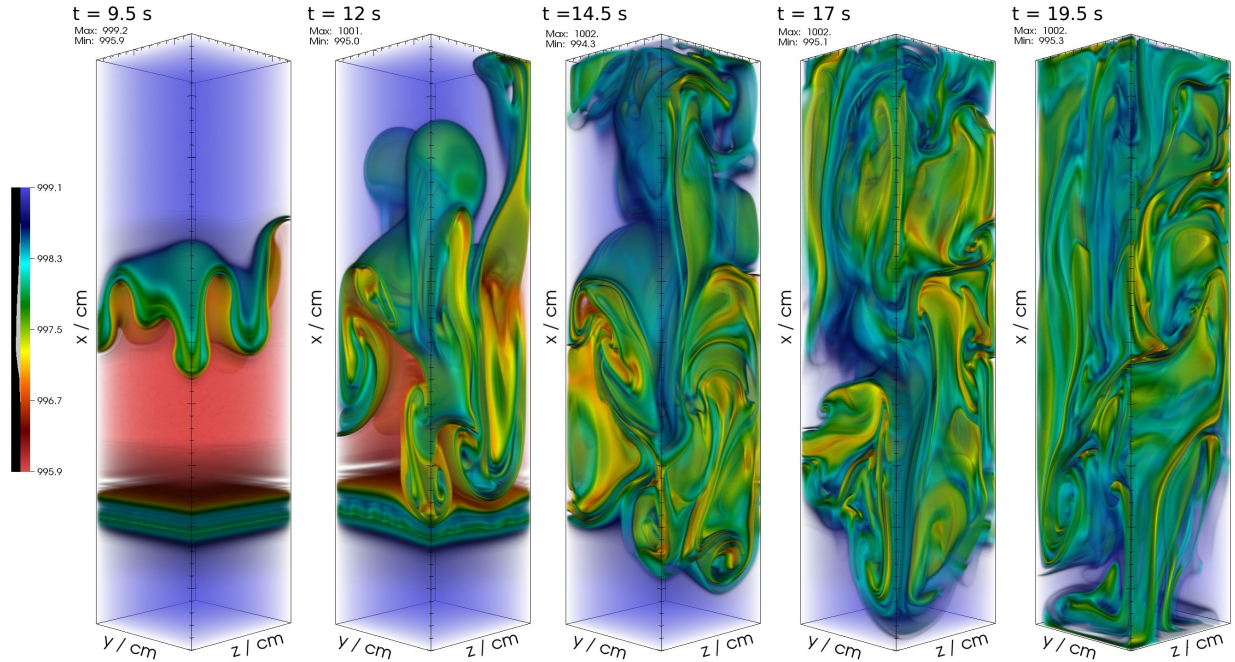
Figure 4.4:   Volume plots of density, where the colour and opacity function are given by the colour bar. Along each axis, the large ticks indicate $1\,\mathrm{cm}$ spacings, while the small ticks indicate $0.2\,\mathrm{cm}$ spacings. The colour bar indicates the density in $\mathrm{kg/m^3}$.

4.4   Three-Dimensional Double-Diffusive Rayleigh-Taylor Instability

The focus of this chapter is a three-dimensional direct numerical simulation of double-diffusive Rayleigh-Taylor instabilities arising from an initial density stratification as defined by equations (4.2) and (4.3). The stratification is identical to that of the two-dimensional simulation presented in panels (e) and (f) of Fig. 4.2, with $T_0 = 15\,^{\circ}\mathrm{C}$, $\Delta T = 25\,^{\circ}\mathrm{C}$, $s_0 = 0$, and $\Delta s = 5\,\mathrm{psu}$. The domain of this simulation is $L_x = 10\,\mathrm{cm}$ tall in the vertical direction, and $L_y = 2.4\,\mathrm{cm}$ and $L_z = 2.5\,\mathrm{cm}$ wide in the horizontal directions. 2048 grid points are used in the x-direction, giving a vertical grid spacing of $4.88 \times 10^{-3}\,\mathrm{cm}$. 512 grid points are used in each of the horizontal directions, for grid spacings of $4.69 \times 10^{-3}\,\mathrm{cm}$ and $4.88 \times 10^{-3}\,\mathrm{cm}$ in the y- and z-directions, respectively. Volume plots of the density field of this flow at various times are presented in Fig. 4.4. At $t = 9.5\,\mathrm{s}$, motion occurs primarily along the upper pycnocline, as RT instabilities on the order of $1\,\mathrm{cm}$ wide begin

to develop, which reflects the wavelength of $\lambda_{\mathrm{RT}} = 0.795\,\mathrm{cm}$ predicted in Section 4.2. As noted in the 2D simulation presented in Figs. 4.2(e), (f), the presence of a double layer is observed along each of the pycnoclines, with thin layers of lighter fluid forming between regions of heavier fluid. By $t = 12\,\mathrm{s}$, some small rippling can be observed along the lower pycnocline, indicating the initial formation of salt fingers, although some of the sinking RT instabilities have begun to interact with and distort the lower pycnocline. Between $t = 12\,\mathrm{s}$ and $14.5\,\mathrm{s}$, the RT instabilities slow down as they travel through the lower pycnocline. This reflects the results of Jacobs and Dalziel [36], who observed that there was little penetration by RT instabilities into the bottom layer of a three-layer system when the densities were similar. However, there seems to be enhanced penetration later in these simulations due to the increase in density above the initial maximum due to double-diffusive effects. Additionally, fine features of alternating low and high density are observed within the larger RT structures. As time progresses, the dominant flow features appear to be due to the larger-scale rising and sinking RT instabilities, although finer density features can be observed in the rising and falling bulbs. This can be difficult to distinguish in the three-dimensional volume plots, so Fig. 4.5 presents slices of density (top, (a), (c), (e)) and kinetic energy (bottom, (b), (d), (f)) in the xz-plane along $y = 0.60\,\mathrm{cm}$, at various times. At $t = 12\,\mathrm{s}$, the high density region is still fairly coherent, with double layers occurring along the interface of the easily-distinguishable large scale RT instabilities. By $t = 15.75\,\mathrm{s}$, the shape of some larger RT instabilities are still noticeable, but the thin density filaments are far more prominent. By $t = 19.5\,\mathrm{s}$, the flow has become fairly chaotic, though thin regions of alternating levels of density are still prominent. In contrast, the kinetic energy field displays no similar small scale features, instead appearing to trace some of the larger-scale features of the density field. At $t = 12\,\mathrm{s}$, there is noticeable overlap between the RT features visible in the density field and some of the larger features present in the KE field.

As depicted in Fig. 4.6, the flow can be separated into active and quiescent regions that evolve with time. Early in the flow (Fig. 4.6(a)), the activity occurs near the original upper pycnocline, as the RT instabilities have only begun to form. Above and below the instabilities, the flow is fairly inactive, even near the double layer forming along the lower pycnocline. At intermediary stages (Fig. 4.6(b)), the flow is active above the lower pycnocline and quiescent below it. With enough time (Fig. 4.6(c)), the RT instabilities pass through the lower double layer, and the entire domain becomes active.

Slices along $y = 0.60\,\mathrm{cm}$ in the xz-plane of temperature (top, (a),(c),(e)) and salinity (bottom, (b),(d),(f)) are presented in Fig. 4.7. The salinity and temperature fields exhibit similar behaviour to the gravity currents presented in Chapter 3: the geometries of the fields are similar, but the lower diffusivity of salt results in sharper interfaces throughout the

78
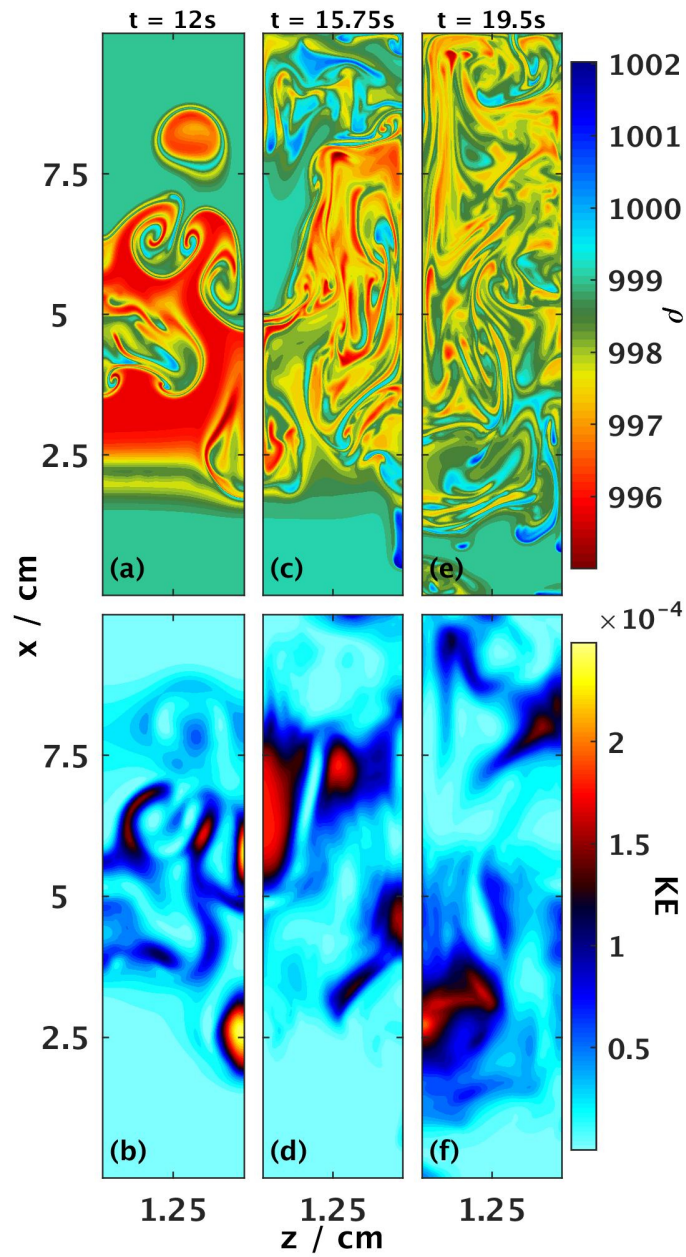
Figure 4.5: Contour slices of density (top) and kinetic energy (bottom) in the xz-plane along $y = 0.60$ cm. The upper colour bar indicates the density in kg/m^3, while the lower colour bar indicates the kinetic energy in m^2/s^2.
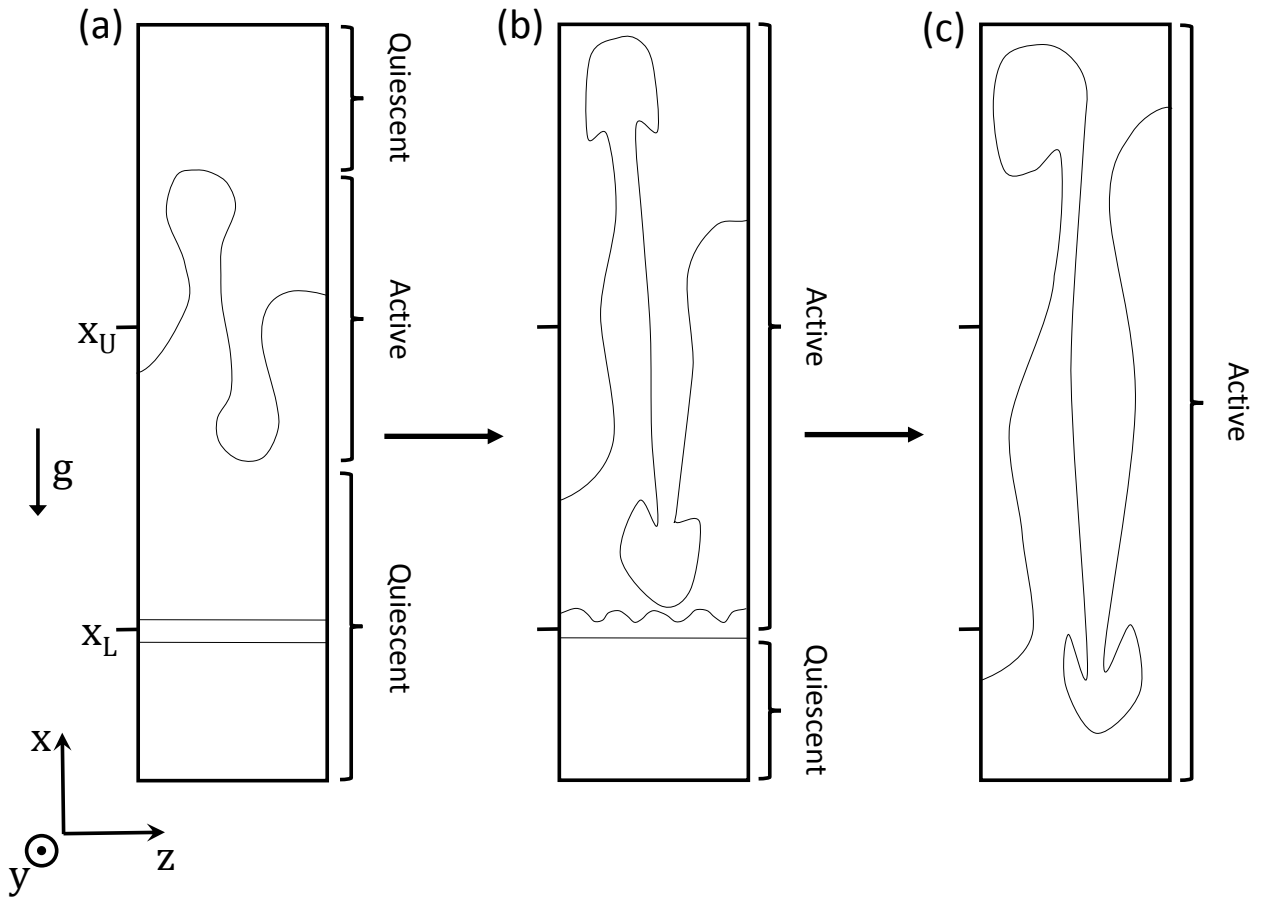
Figure 4.6: Sketches depicting the general evolution of the flow with time. (a) Initially, as the RT instabilities begin to grow, any activity is confined to near the upper pycnocline, while the rest of the domain is largely quiescent. (b) As time passes, the RT instabilities grow and fill the domain, the region below the lower pycnocline remains fairly inactive. (c) Towards the end of the simulation, the RT instabilities have grown to fill the domain, causing activity to permeate the entire domain.

salinity fields. At $t = 12$ s, both fields are very similar geometrically, though, as expected, the higher diffusivity of temperature has led to broader interfaces between the hot and cold fluid, while the salinity interfaces are significantly sharper. This is indicative of the double layer discussed above. For example, consider the round parcel of lower density fluid (in yellow) near the top of the domain in Fig. 4.5 (a). It is immediately surrounded by a thin ring of higher density fluid (in light blue), which is in turn surrounded by a thin ring of low density fluid (in green). Fig. 4.8 examines the temperature and salinity fields of this parcel in more detail, with white contour lines tracing regions where the density is $998.1 \, \text{kg/m}^3$. The region traced by the inner white contour is slightly higher in density than the initially light fluid ($995.91 \, \text{kg/m}^3$). Between the inner contour and the middle contour, salinity stays high enough that the decrease in temperature results in denser fluid (near the density of the initial high density fluid, $999.12 \, \text{kg/m}^3$). The middle contour effectively traces the region of non-zero salinity, so between it and the outer contour, the fluid is nearly fresh, indicating that the increase in temperature has caused a decrease in density of the fresh fluid. At $t = 15.75$ s and 19.5 s, both the T and s fields exhibit similar large scale features, though within the large scale features of the salinity field there are many finer features. The small scale features of the salinity field also appear to correspond fairly well with the small scale features of the density field.

In a system where the density depends on a single tracer subject to a typical advection-diffusion equation, the maximum fluid density can never increase, and the minimum fluid density can never decrease. However, this is possible in double-diffusive systems. For example, in the heat-salt system presented here, if enough heat is transferred from the hot, salty layer to the cool, fresh layer, the increase in heat to the cold layer along the interface can be enough to decrease its density below the initial density of the hot, salty layer. Similarly, this loss of heat can increase the density in the salty layer above the initial density of the fresh layer. This behaviour will be captured when using both linear and nonlinear equations of state for density.

By computing the minimum and maximum density at each time step and determining when they are above and below the initial maximum and minimum, the time at which double-diffusion becomes important can be estimated. In Fig. 4.9, the maximum and minimum density as a function of time are given by the blue and red lines, respectively. The dashed lines indicate the initial minimum ($995.91 \, \text{kg/m}^3$) and maximum ($999.12 \, \text{kg/m}^3$) densities as set by equations (4.2) and (4.3). The first instance of ρ increasing above the initial maximum density occurs at $t = 9.25$ s. The first instance of ρ decreasing below the initial minimum density occurs 1.5 s later at $t = 10.75$ s. This is likely due to the greater rate of change of density with respect to temperature when $T = 40°C$ than when $T = 15°C$, which implies that as the warmer water loses heat to the cooler water, there will be a
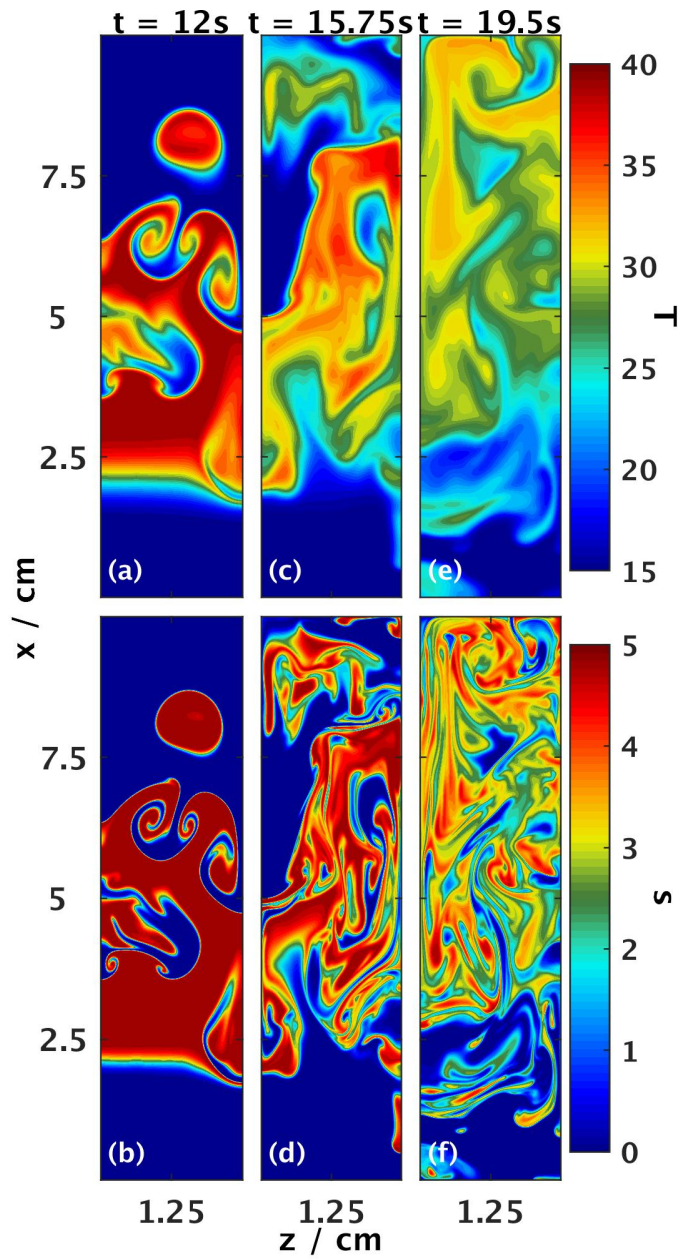
Figure 4.7: Contour slices of temperature (top) and salinity (bottom) in the xz-plane along $y = 0.60$ cm. The upper colour bar indicates the temperature in °C, while the lower colour bar indicates the salinity in psu.
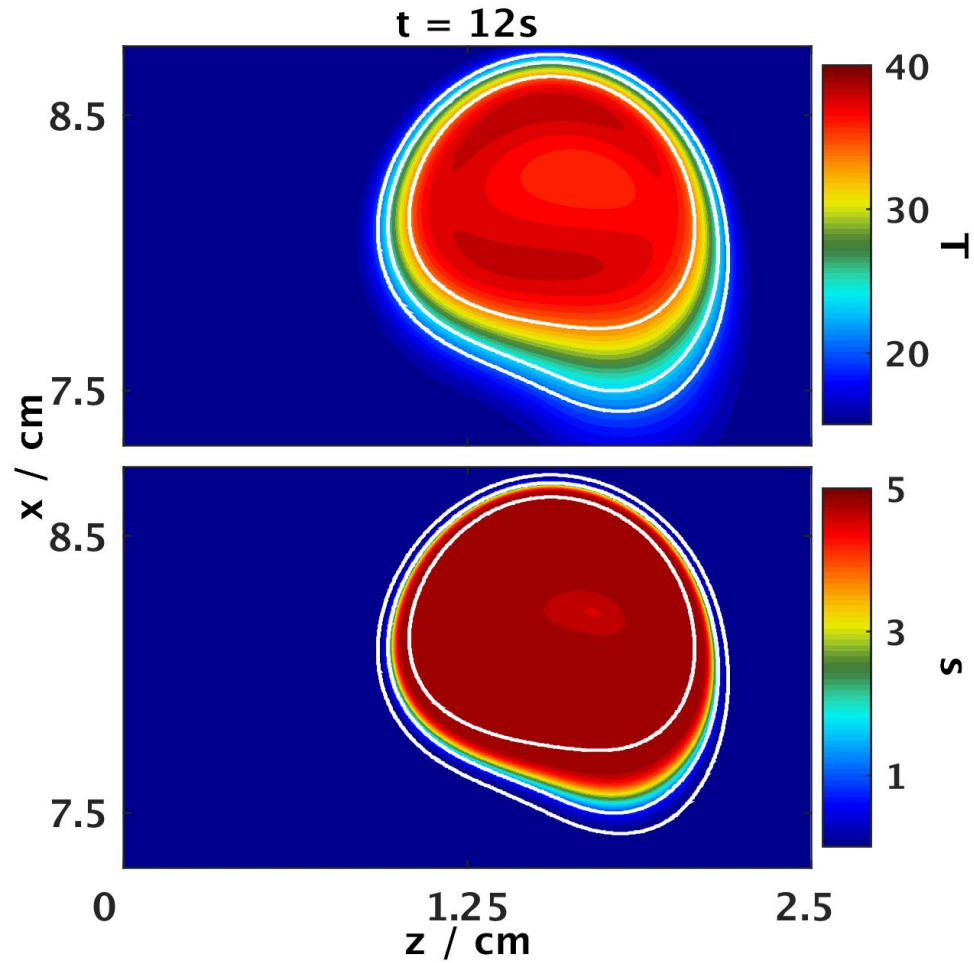
Figure 4.8: Magnified contour plots of temperature (top) and salinity (bottom) in the xz-plane along $y = 0.60\,\text{cm}$ about the lower density parcel of fluid near the top of the domain at $t = 12\,\text{s}$. The white contour lines indicate regions where $\rho = 998.1\,\text{kg/m}^3$. The upper colour bar indicates the temperature in $^\circ$C, while the lower colour bar indicates the salinity in psu.
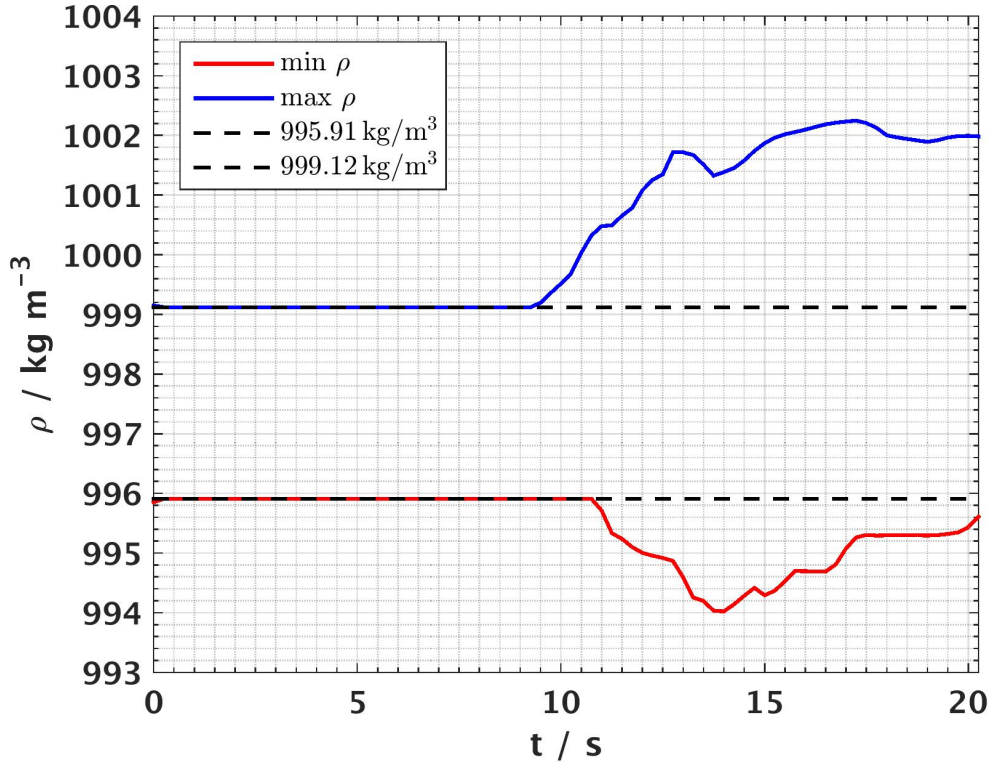
Figure 4.9: Minimum (red) and maximum (blue) density as a function of time, with the initial minimum (995.91 kg/m³) and maximum (999.12 kg/m³) given by dashed lines.

greater increase in density in the warm, salty water than there a decrease in density of the cool, fresh water. The maximum density increases to $1001.72\,\mathrm{kg/m^3}$ at $t = 12.75\,\mathrm{s}$, before briefly decreasing to $1001.33\,\mathrm{kg/m^3}$ at $t = 13.75\,\mathrm{s}$, and then increasing above $1002\,\mathrm{kg/m^3}$ and staying fairly steady at the density for the remainder of the simulation. The minimum density reaches its lowest value of $994.02\,\mathrm{kg/m^3}$ at $t = 14\,\mathrm{s}$.

Slices of the rate of viscous dissipation in the xz-plane along $y = 0.60\,\mathrm{cm}$ are presented in Fig. 4.10. These slices indicate that the regions of greatest dissipation occur along the interfaces of the larger scale features in the kinetic energy fields. While not as large as the length scales of kinetic energy, the dissipation lacks the finer scale features of density and salinity. The length scales of each of the fields discussed in this section will be examined in greater detail using Fourier analysis in Section 4.5.

Fig. 4.11(a) presents the total kinetic energy, as well as the individual contributions from
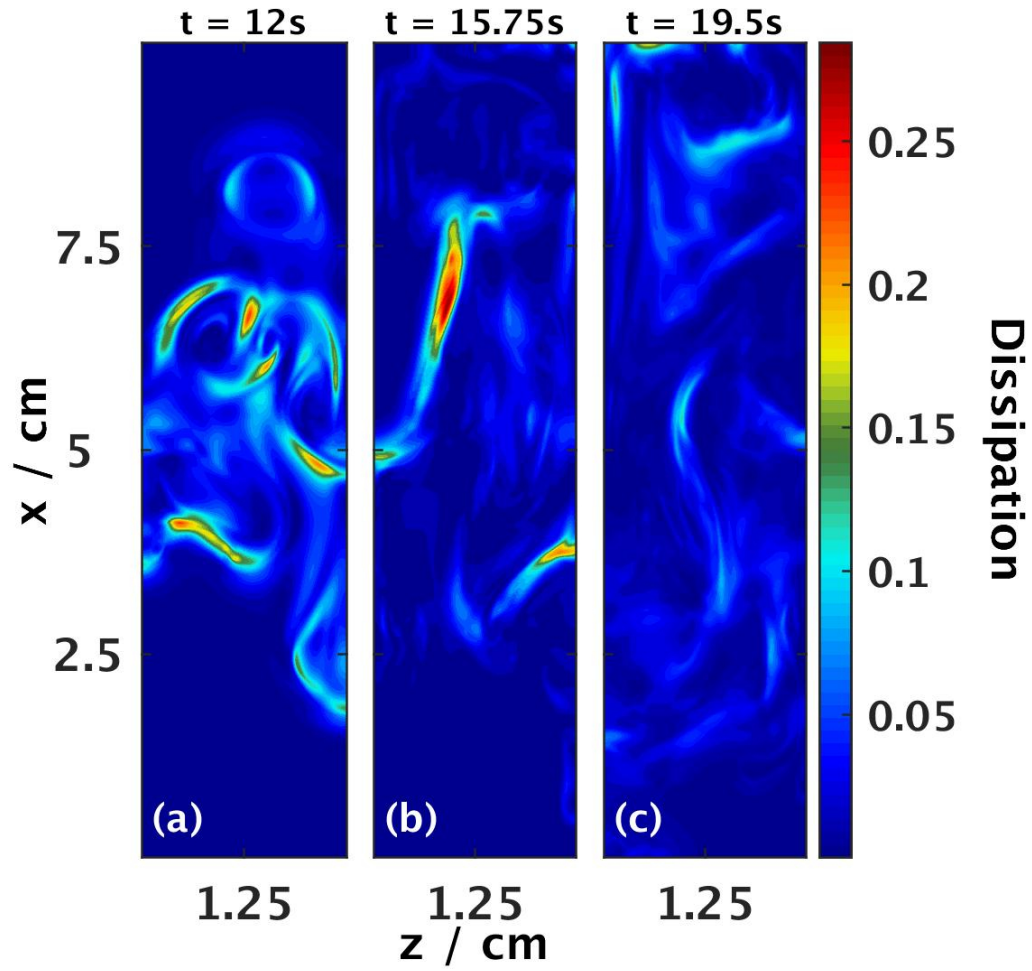
Figure 4.10: The rate of viscous dissipation in the xz-plane along $y = 0.60\,\mathrm{cm}$ at (a) $t = 12\,\mathrm{s}$, (b) $15.75\,\mathrm{s}$, and (c) $19.5\,\mathrm{s}$. The colour bar indicates the viscous dissipation in $\mathrm{kg/m\,s^3}$.

u, v, and w, as a function of time. The primary contribution to kinetic energy comes from the vertical motion of the fluid, while there is relatively little contributed by the horizontal motions. The contributions to kinetic energy by each of the horizontal components are nearly equal in magnitude, since the flow has no preferential horizontal direction. The KE exhibits two different maxima at $t = 12.5$ s and 18.25 s, and a local minimum at $t = 14.75$ s. The decrease in kinetic energy between $t = 12.5$ s and 14.75 s appears to correspond to the interaction of the rising RT instabilities with the top of the domain, and to the sinking RT instabilities interacting with the lower pycnocline, as observed in Fig. 4.4 at $t = 12$ s and 14.5 s. The subsequent increase in KE appears to be due to additional action of the instability in previously inactive regions, such as along the edge (nearest the x-axis label) of the domain and along the front corner below $x = 2$ cm at $t = 17$ s in Fig. 4.4.

The total rate of viscous dissipation is presented in Fig. 4.11(b). It begins to increase rapidly around $t = 7.5$ s, and reaches a maximum ($\phi_{\mathrm{Tot}} = 1.904 \times 10^{-6}$ kg/m s^3) at $t = 12.5$ s, after which there is a slower decrease to approximately $\phi_{\mathrm{Tot}} = 1 \times 10^{-6}$ kg/m s^3. The time at which the maximum dissipation is reached corresponds to the first maximum of total kinetic energy, while the total dissipation continues to decrease even as KE reaches its second maximum.

4.4.1   Vertical Tracer Flux

The horizontal means of the salinity, temperature, and density fields as a function of x from $t = 10$ s to 20 s are presented in Fig. 4.12. At $t = 10$ s, the effect of the developing RT instability along the upper interface is visible, as the mean interface between the hot, salty layer and the cool, fresh layer becomes broader. This interface appears to have two distinct nearly linear regimes, with two distinct slopes above and below $x = 6$ cm, with the decrease to the lower density fluid below $x = 6$ cm occurring over a greater depth than the increase to the higher density fluid above it. Though there are some oscillations displayed by the salinity (at $x = 4.5$ cm and 7 cm) and the density (at $x = 2$ cm and 7 cm), the mean fields are still relatively smooth at $t = 10$ s. At later times, however, each of the mean fields are dominated by small oscillations, with the salinity and density fields exhibiting a greater number of finer scale oscillations than the temperature field. The general shape of the mean salinity and temperature fields are very similar, though the salinity fields exhibit far finer vertical features due to the lower diffusivity of salinity. On the time scale of this simulation, the density field appears to be tending to a stable, nearly linear stratification, though to verify that the steady-state for density is indeed linear, a larger ensemble of experiments that simulate a longer time period would be needed. Above the initial upper pycnocline at $x = 6$ cm, both temperature and salinity experience an overall
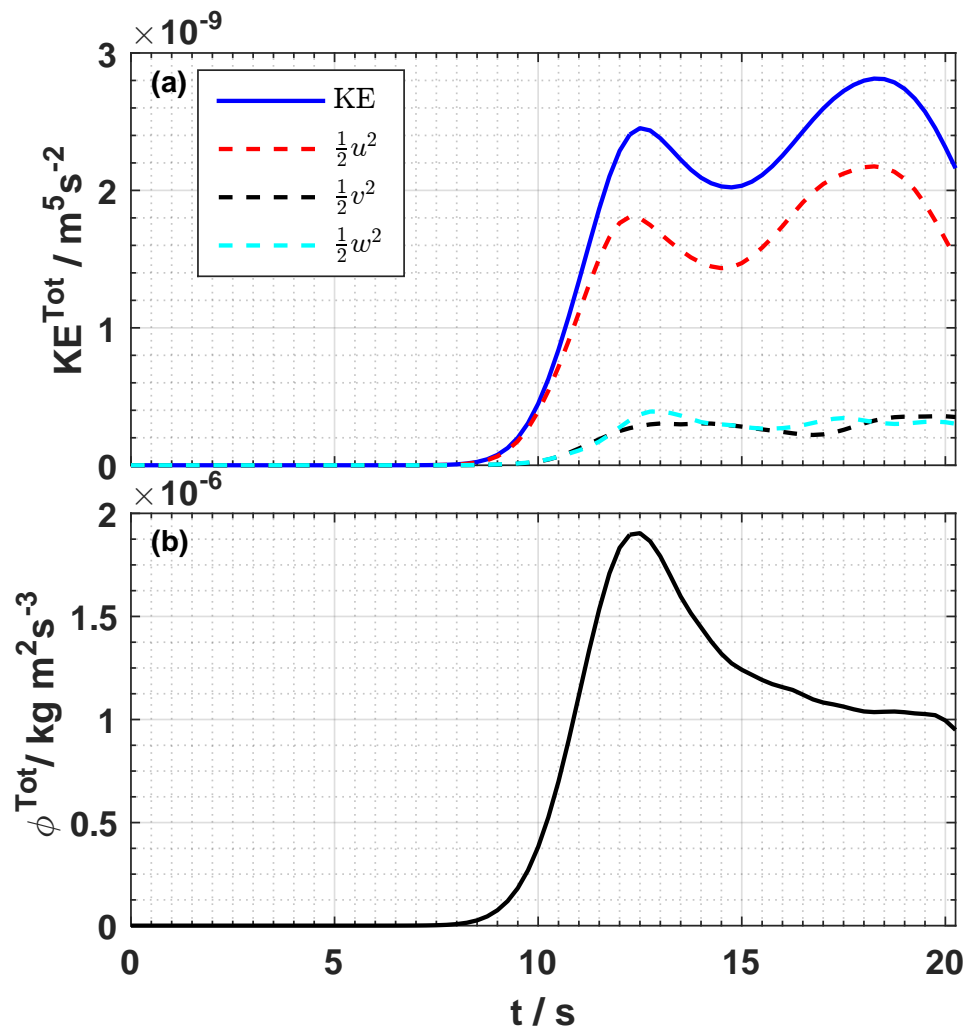
Figure 4.11: (a) Total kinetic energy, with the total x-, y-, and z-components of kinetic energy, and (b) the total rate of viscous dissipation as a function of time.
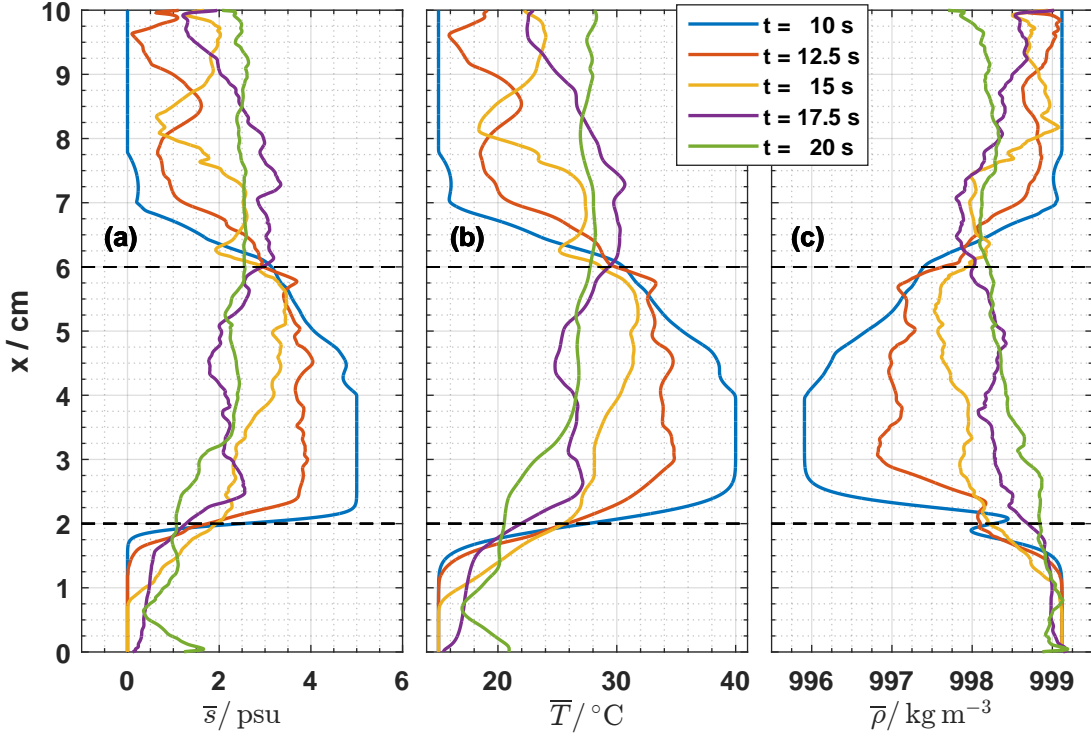
Figure 4.12: Horizontal means of (a) salinity, (b) temperature, and (c) density as a function of x at later times. The dashed lines along $x = 2\,\mathrm{cm}$ and $6\,\mathrm{cm}$ indicate the initial locations of the pycnoclines.

increase, with their mean values tending to $2.25\,\mathrm{psu}$ and $28\,^\circ\mathrm{C}$ above $x = 6\,\mathrm{cm}$ at $t = 20\,\mathrm{s}$. Between $x = 2\,\mathrm{cm}$ and $6\,\mathrm{cm}$ in the initially hot, salty layer, there is an overall decrease in temperature and salinity, while below $x = 2\,\mathrm{cm}$, both fields experience an increase. The increase in mean temperature and salinity in the lower cool, fresh layer is not as significant as the increase in the upper cool, fresh layer, due to the relative inactivity of the flow in that region.

The vertical fluxes of salinity, temperature, and density are defined as

$$F_s\left(x,t\right) = \overline{u's'}, \quad F_T\left(x,t\right) = \overline{u'T'}, \quad F_\rho\left(x,t\right) = \overline{u'\rho'}, \tag{4.4}$$

respectively, where the overline denotes the horizontal mean of the variable, e.g.,

$$\overline{s} = \frac{1}{L_y L_z} \iint\limits_{[0,L_y] \times [0,L_z]} s \, dy \, dz, \tag{4.5}$$

and the primes indicate the fluctuation from the horizontal means, e.g., $s' = s - \overline{s}$. At early times (Fig. 4.13), the limited vertical motion results in negligible vertical fluxes for each of the fields. Between $t = 7.5\,\mathrm{s}$ and $9.5\,\mathrm{s}$, there is a rapid increase in the magnitude of each of the fluxes, with the maximum occurring at $x = 6\,\mathrm{cm}$ for salinity, and slightly below $x = 6\,\mathrm{cm}$ for temperature and density. During this period, the salinity and temperature fluxes are entirely positive, while the density flux is primarily negative, with some slightly positive fluxes occurring at $t = 7.5\,\mathrm{s}$ and $t = 8\,\mathrm{s}$ just above $x = 6\,\mathrm{cm}$. For each tracer, the flux profiles are all fairly smooth.

At later times (Fig. 4.14), the flux profiles are considerably less smooth. The temperature and salinity flux profiles display similar shapes, although the salinity flux exhibits a significant number of finer scale oscillations. This is indicative of the fine scale features of alternating low and high salinity as presented in Figs. 4.7 (b), (d), (f). The density flux exhibits similar fine scale oscillations, reflecting how the shape of the density field is dominated by the salinity field. For salinity and temperature from $t = 10\,\mathrm{s}$ to $17.5\,\mathrm{s}$, the flux is still mostly positive, though at $t = 12.5\,\mathrm{s}$, $15\,\mathrm{s}$, and $17.5\,\mathrm{s}$, it is negative below $x = 3\,\mathrm{cm}$. It is also negative at $t = 15\,\mathrm{s}$ above $x = 8.5\,\mathrm{cm}$. The density flux stays primarily negative, although near and below $x = 3\,\mathrm{cm}$, similar to the salinity and temperature fluxes, it is occasionally positive at certain times. At $t = 20\,\mathrm{s}$, the salinity flux is almost entirely negative below $x = 6\,\mathrm{cm}$, while the temperature flux is almost entirely negative below $x = 4.5\,\mathrm{cm}$.

In several studies [43, 92, 44], there has been an effort to parameterize effective diffusivities for salinity, temperature, and density (K_s, K_T, and K_ρ), based on the vertical fluxes and gradients of the horizontal mean fields,

$$\overline{u's'} = -K_s\left(t\right)\frac{\partial \overline{s}}{\partial z}, \quad \overline{u'T'} = -K_T\left(t\right)\frac{\partial \overline{T}}{\partial z}, \quad \overline{u'\rho'} = -K_\rho\left(t\right)\frac{\partial \overline{\rho}}{\partial z}. \tag{4.6}$$

This is a form of parameterization that is common in turbulence theory [46]. Though it would be beneficial to calculate these approximate diffusivities for usage in larger scale models where this type of double-diffusion is a subgrid scale process, the flow considered here does not lend itself well to such an approximation. First, consider the fluxes presented in Figs. 4.13 and 4.14. As mentioned, until later times, the fluxes typically only have a single sign, with the salinity and temperature fluxes being mostly positive, and the density
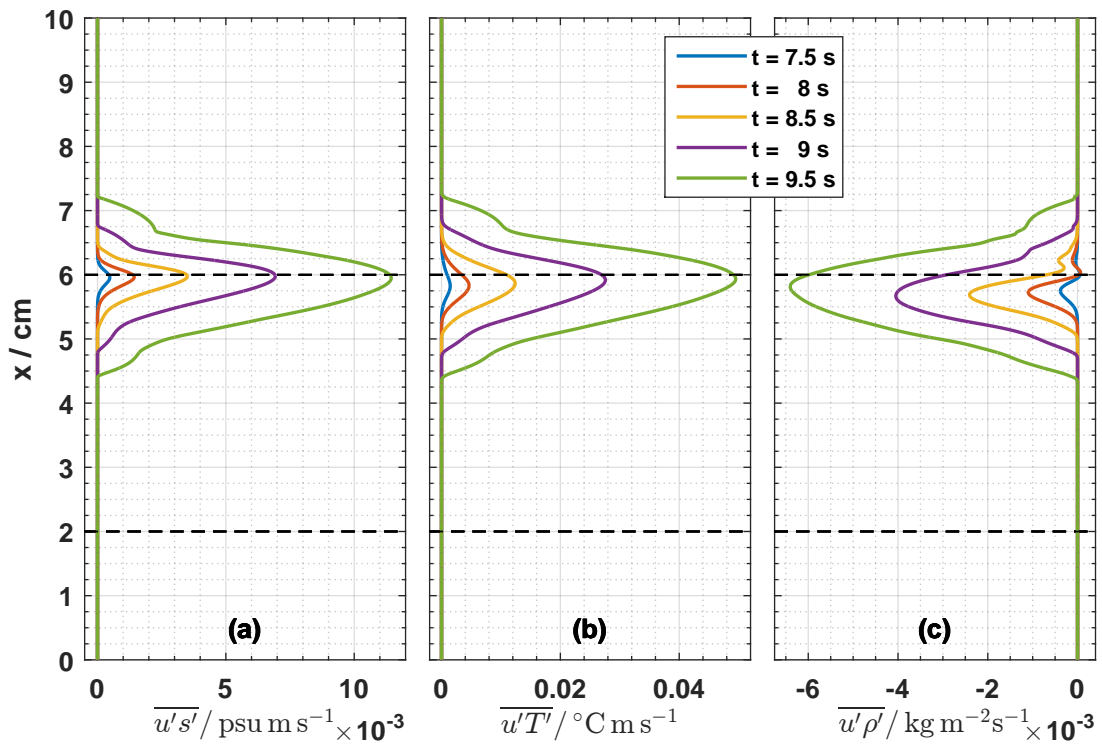
Figure 4.13: Horizontal means of (a) salinity flux, (b) temperature flux, and (c) density flux as a function of x from $t = 7.5\,\mathrm{s}$ to $9.5\,\mathrm{s}$. The dashed lines along $x = 2\,\mathrm{cm}$ and $6\,\mathrm{cm}$ indicate the initial locations of the pycnoclines.
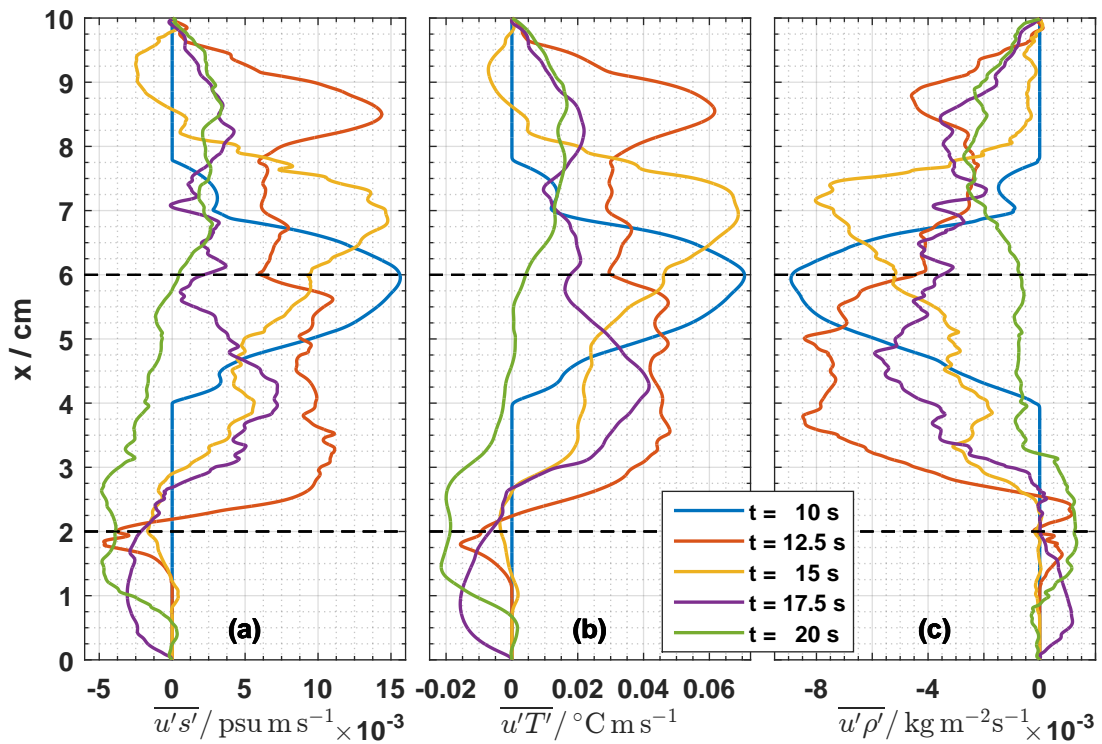
Figure 4.14: Horizontal means of (a) salinity flux, (b) temperature flux, and (c) density flux as a function of x from $t = 10\,\mathrm{s}$ to $20\,\mathrm{s}$. The dashed lines along $x = 2\,\mathrm{cm}$ and $6\,\mathrm{cm}$ indicate the initial locations of the pycnoclines.
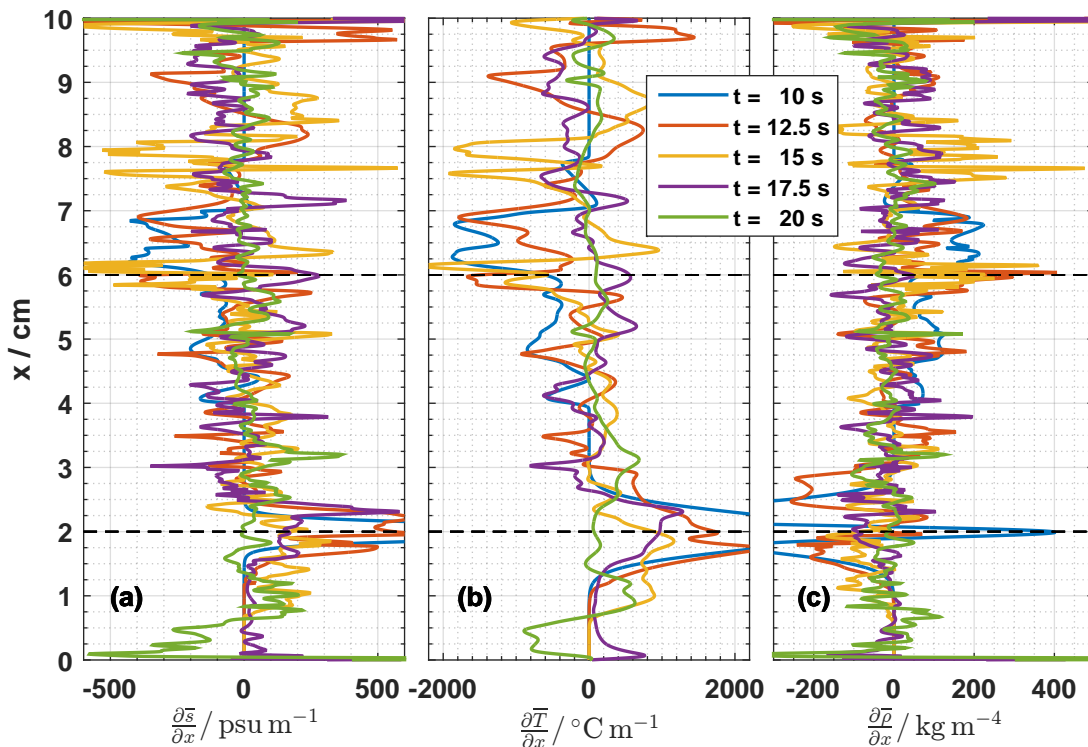
Figure 4.15: Vertical derivatives of the horizontal means of (a) salinity, (b) temperature, and (c) density as a function of x at later times. The dashed lines along $x = 2\,\text{cm}$ and $6\,\text{cm}$ indicate the initial locations of the pycnoclines.

fluxes being mostly negative. Now consider the vertical derivative of each of the mean fields presented in Fig. 4.12. From the rapid oscillations of increasing and decreasing tracer fields, this results in large magnitude derivatives that rapidly oscillate sign with height, as shown in Fig. 4.15. Calculating the eddy diffusivities as described by equations (4.6) pointwise at different heights would result in diffusivities that rapidly oscillate sign with x, as well as alternating sign with time for values calculated at a given height. Fig. 4.16 presents time series of the eddy diffusivities of salinity, temperature, and density calculated pointwise at $x = 2\,\text{cm}$, $4\,\text{cm}$, $6\,\text{cm}$, and $8\,\text{cm}$. At certain points when the vertical derivatives are near zero, this can cause the estimated diffusivity to reach orders of magnitude larger than the scales presented here, with maximum values on the order of 1. These time series show how the diffusivities can vary significantly based on both position and time at which they
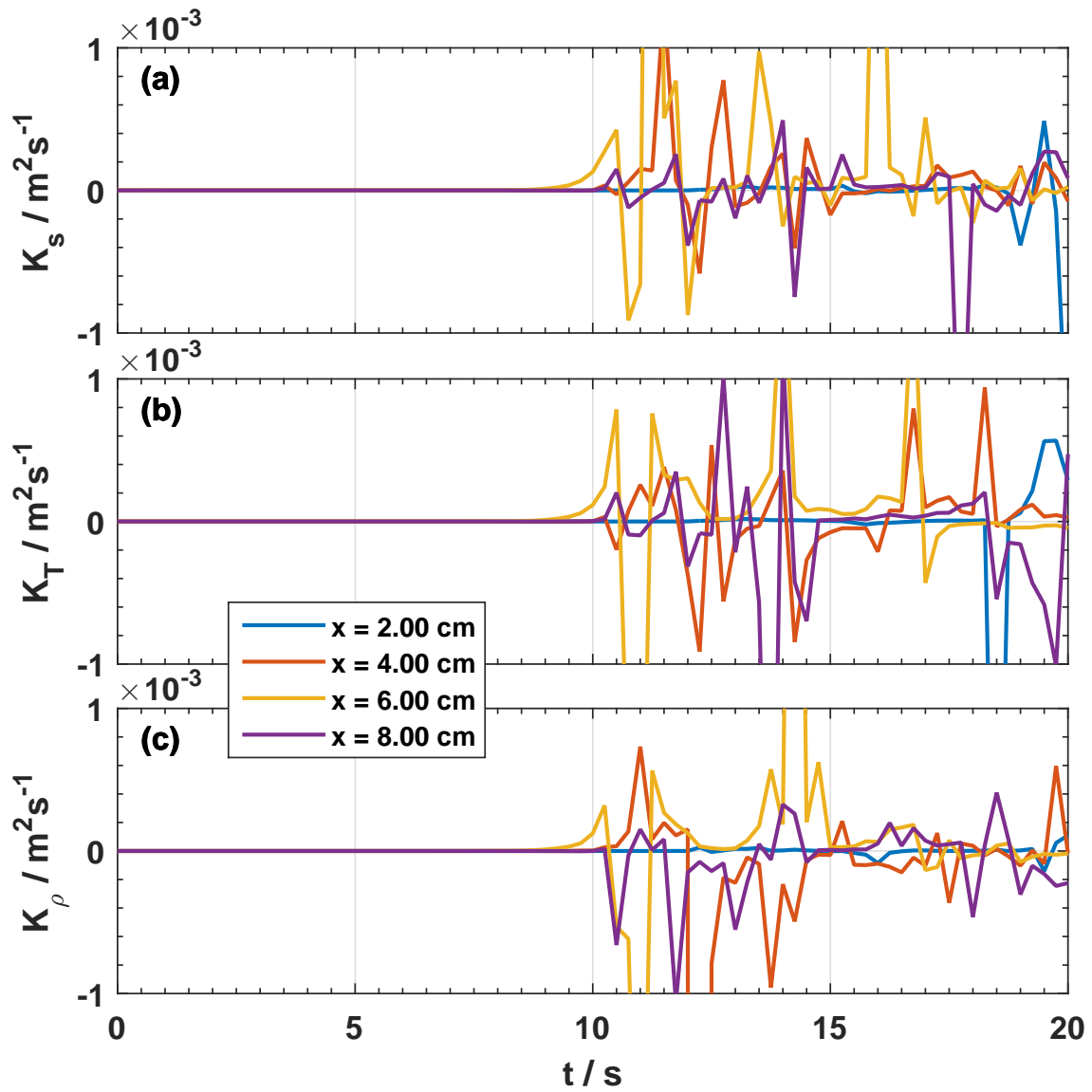
Figure 4.16: (a) Eddy diffusivity of salinity, (b) eddy diffusivity of temperature, and (c) eddy diffusivity of density at $x = 2\,\text{cm}$, $4\,\text{cm}$, $6\,\text{cm}$, and $8\,\text{cm}$, as a function of time.

were calculated. This indicates that the eddy diffusivity approximation is not valid for the simulation presented here. Equations 4.6 assume that the flux is determined by the local vertical gradient [46]. However, this assumption does not apply if the flux is a result of motion on a larger scale than the length scale of the local gradients (Kundu and Cohen [46, see Figure 13.21]). In this simulation, the vertical flux is largely dictated by the vertical motion of the RT instabilities, carrying cool, fresh water downward, and hot, salty water upward. Meanwhile, the length scales of the tracer gradients are much finer than the scale of the RT instabilities, as shown in Fig. 4.17. The contours in this figure indicate the magnitude of the density gradient, $|\nabla \rho|$. The thin scale of the high magnitude features indicate very sharp transitions between regions of high density to low density. This is indicative of the small diffusive scales of salinity. At $t = 12\,\mathrm{s}$, these regions also trace the larger scales of primary motion as set by the RT instabilities. A sketch further detailing this idea is presented in Fig. 4.18.

4.5 Fourier Analysis

A natural extension of double-diffusive research, especially for flows of oceanic interest, is to examine the interplay of double-diffusion and turbulence. In the ocean, measurements have been made to determine the viscous dissipation in double-diffusive regions [25, 2]. Laboratory experiments have examined the effects of intermittent and local patches of turbulence on salt fingering-favourable stratifications [107, 111, 110]. Differential diffusion in isotropic turbulence has been the subject of several papers [6, 118, 41]. Yeung and Pope [118] observed that the correlation between the two tracers with identical initial conditions decreased with time, which is the case with the salt and temperature fields presented in the above DNS. In conjunction with classical turbulence theory, these studies ignore the effect of variable density, and thus miss an important aspect of double-diffusive flow. More recently, there have been numerical investigations into double-diffusive stratified turbulence [22, 26]. Additionally, measurements from the North Atlantic Tracer Release Experiment (NATRE) in a salt fingering-favourable region of the Canary Basin did not resolve the typical staircase distribution associated with fingering [94]. It was suggested that region was turbulent enough to prevent the formation of a persistant staircase, and the fluxes due to both turbulence and salt fingering were estimated. Additional work based on the NATRE by Ruddick et al. [76] attempted to determine the primary mixing mechanism in the sampled region, and found that the measurements did not reflect the behaviour of salt fingers, or isotropic or low-Reynolds number turbulence.

The research presented in this chapter was motivated in part by an effort to obtain
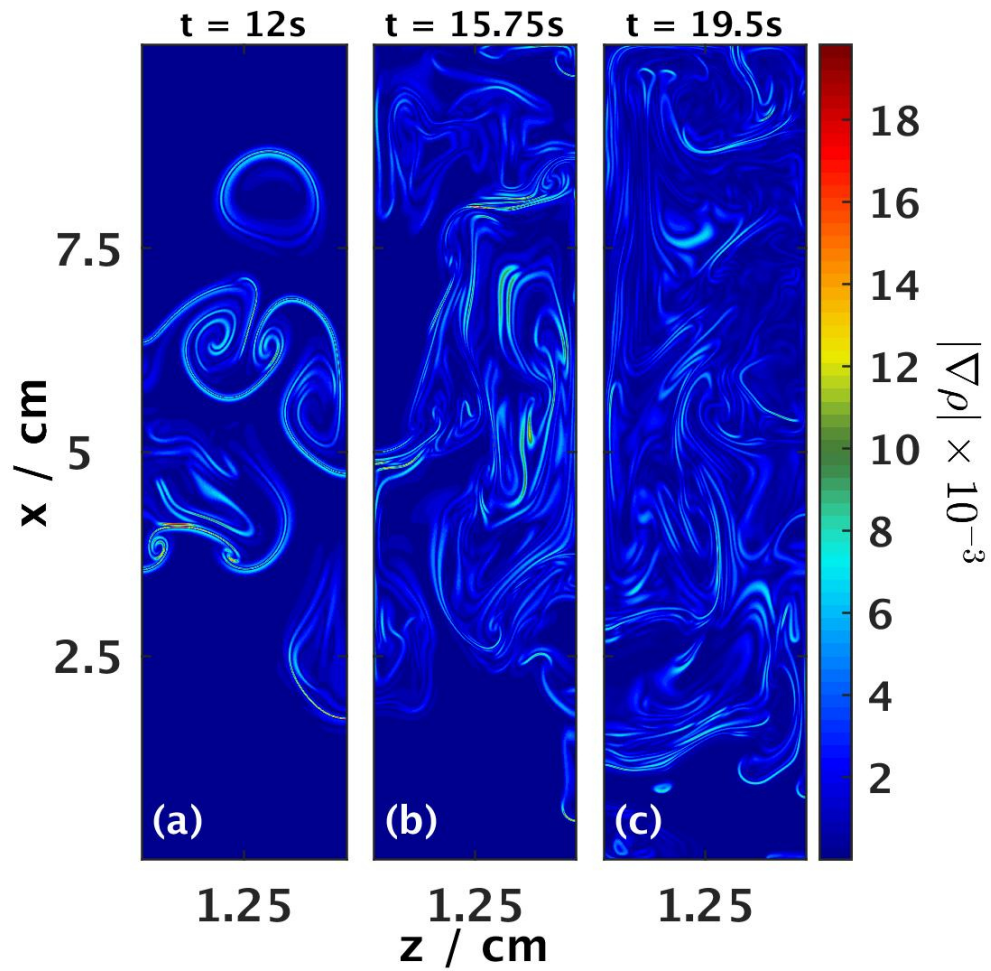
Figure 4.17: Magnitude of the gradient of density in the xz-plane along $y = 0.60\,\text{cm}$ at (a) $t = 12\,\text{s}$, (b) $15.75\,\text{s}$, and (c) $19.5\,\text{s}$.
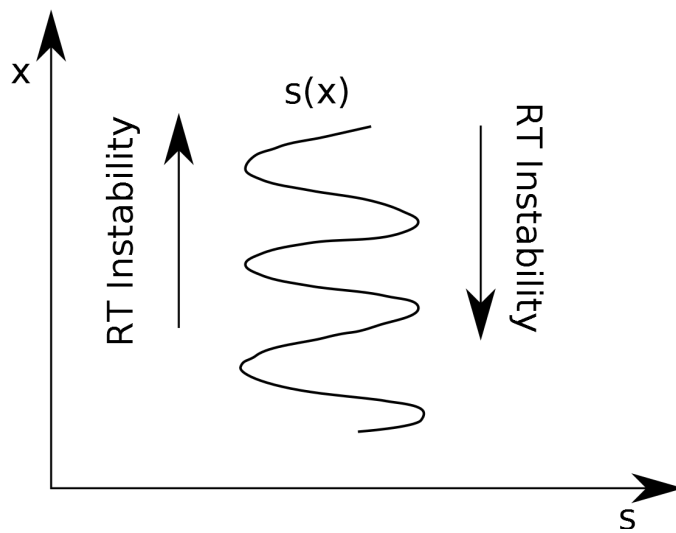
Figure 4.18: Sketch of the behaviour of the vertical salinity profile $s(x)$ in these simulations, with rapidly changing gradients. The arrows indicate the scales of the currents induced by the RT instabilities, which are larger than the local tracer gradient scales. Image adapted from Kundu and Cohen [46, Figure 13.21].

turbulence from a double-diffusive flow without imposing shear or artificially forcing the flow. In this section, Fourier analysis is used to characterize the different dominant length scales of the flow, and the results are used to estimate an appropriate filter to separate the high and low wave number components of density.

4.5.1   Spectra of Two-Dimensional Slices

Each of the fields presented in Section 4.4 exhibit different dominant length scales. The salinity and density fields display very fine scale features, which are absent from the kinetic energy and temperature fields. The Fourier spectrum of each field provides a way of measuring the contribution to that field from each length scale. A challenge with the data presented in this chapter, and indeed a challenge in many scientific fields due to advances in technology [38], is the analysis of large data files resulting from high-resolution simulations or observations. At a given time step, a single variable file from the simulation presented here is about 4 GB (gigabytes) in size. None of the boundaries in this simulation are periodic, so to examine this data using Fourier analysis, each of the variable fields must be extended appropriately in order to obtain periodicity and avoid edge effects, as noted in Section 2.3. To perform a three-dimensional fast Fourier transform (FFT) on this data, a given variable would need to be extended in all three directions. This means 7 additional copies of the data field would be required, resulting in a 32 GB file that would be difficult to analyze in real time on local architectures. To avoid these constraints, multiple two-dimensional slices of data were analyzed along each direction, as each 2D slice would only need 3 additional copies in order to apply a two-dimensional FFT. The density, temperature and salinity fields require even extensions in all directions. For the velocity fields, the free-slip conditions require odd extensions in the same direction as the velocity component, but even extensions in the other two directions. For example, u would be subject to an even extension in the y- and z-directions, but an odd extension in the x-direction. The result of applying a Fourier transform that is even or odd in a given direction is the same as applying a cosine transform or sine transform in that direction, respectively. Constructing spectra using the discrete cosine transform (DCT) and discrete sine transform (DST) was briefly investigated; however, because MATLAB has no built-in 2D DST function, it was more straightforward to perform FFTs on extended data fields. The resulting periodicity of each of the fields gives two-dimensional spectra that are symmetric across both of the wave number axes. As such, the spectra presented here will be limited to examining the upper right quadrant, as the other three would give identical information.

In Fig. 4.19, the base 10 logarithm of the two-dimensional spectra of horizontal slices along $x = 4$ cm of (a) density, (b) salinity, (c) temperature, (d) kinetic energy, and (e)

dissipation are presented, at $t = 19.5$ s, when the flow is well-developed. As a brief note, all two-dimensional spectra presented in this section are displayed by taking the base 10 logarithm, so for the sake of simplicity, they will just be referred to as the 2D spectra from here onward. The vertical axis of each spectrum corresponds to the wave number in the y-direction, l, while the horizontal axis of each spectrum corresponds to the wave number in the z-direction, m. The most obvious information that can be drawn from these spectra is that both the density and salinity fields experience contributions from much larger wave numbers than any of the other fields. Letting $k_H = \sqrt{l^2 + m^2}$, where k_H is the wave number magnitude, both the density and salinity spectra appear to exhibit a steady decrease in power until $k_H \approx 300 - 400$ cm^{-1}, above which the contribution is minimal. The temperature spectrum displays a similar drop in power, but over a much smaller range of wave numbers, until $k_H \approx 100$ cm^{-1}. The contribution to KE comes entirely from wave numbers below $k_H \approx 50$ cm^{-1}, indicating that the KE is dominated by large scale features. The dissipation spectrum appears to experience a less rapid decrease in power (relative to temperature and KE) as k_H increases, with most of the contribution coming from wave numbers below $k_H \approx 200$ cm^{-1}. There is also a striking similarity between the spectra of density and salinity, reinforcing the idea that the prominent scales of the density field are due to the contribution from salinity.

To examine the evolution of the horizontal spectrum of density with time, Fig. 4.20 presents the 2D density spectra in the yz-plane (horizontal) at various points along the x-axis (vertical). The first column shows spectra at various values of x at $t = 8.25$ s. There is some low wave number activity along the initial pycnoclines at $x = 2$ cm and 6 cm, and negligible signals everywhere else, since initially the flow only occurs near these two regions. Along the lower pycnocline, the signal is due to the variability in the density field introduced by double-diffusion, while along the upper pycnocline, it is due to the RT motion. By $t = 12$ s, the slices between $x = 2$ cm and 8 cm show activity at wave numbers up to $k_H \approx 400$ cm^{-1}, while along $x = 1$ cm all signals are still negligible due to the lack of motion in that region, and along $x = 9$ cm there is a greater contribution from larger values of m than from larger values of l. At later times, along $x = 9$ cm the contributions from l and m appear to be similar, with no preference for either direction. Along $x = 1$ cm, there is a greater contribution from larger wave numbers as time increases due to the increased motion in that region. There are also protrusions that extend from the edges of the spectrum that indicate preferred aspect ratios and directions for the density field, although their locations and intensity vary with time step and vertical position. For example, in Fig. 4.20(g), there is a significant protrusion close to the l-axis, indicating a preference for smaller scale features in the y-direction along $x = 2$ cm at $t = 15.75$ s. In Fig. 4.20(l), there is a similar feature near the m-axis indicating a preference for smaller

98
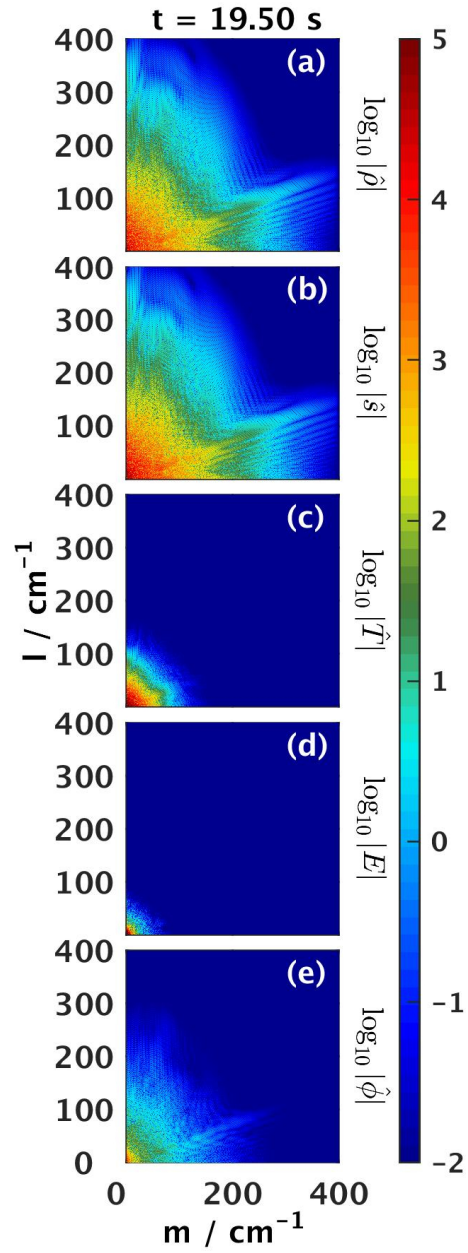
Figure 4.19: Spectrum of (a) density, (b) salinity, (c) temperature, (d) kinetic energy, and (e) rate of viscous dissipation at $t = 19.5\,\mathrm{s}$, along $x = 4\,\mathrm{cm}$.

scale features in the z-direction along $x = 4\,\mathrm{cm}$ at $t = 19.5\,\mathrm{s}$. This suggests that there is no consistently preferred direction for the wave numbers along these horizontal slices.

Fig. 4.21 presents the 2D kinetic energy spectra in the yz-plane at various points along the x-axis. At $t = 8.25\,\mathrm{s}$, the only important activity appears in the spectra along the $x = 6\,\mathrm{cm}$ slice (Fig. 4.21(m)), although there are some negligible signals appearing at very low wave numbers along the $x = 4\,\mathrm{cm}$ and $x = 8\,\mathrm{cm}$ slices. This is in contrast to the density spectra of Fig. 4.20 at $t = 8.25\,\mathrm{s}$, which displayed relatively strong signals along $x = 2\,\mathrm{cm}$ (Fig. 4.20(e)) and $x = 6\,\mathrm{cm}$ (Fig. 4.20(m)), as sketched in Fig. 4.6(a), with an active region near the upper pycnocline, and quiescent regions above and below it. Along $x = 2\,\mathrm{cm}$, this reflects that the primary contributor to kinetic energy is the motion due to the RT instabilities, and that while double-diffusion does serve to increase the variability of the density field, it contributes relatively little KE. By $t = 12\,\mathrm{s}$, the slices between $x = 4\,\mathrm{cm}$ and $8\,\mathrm{cm}$ show activity at wave numbers below $k_H \approx 60\,\mathrm{cm}^{-1}$, while the activity along the $x = 2\,\mathrm{cm}$ and $x = 9\,\mathrm{cm}$ is confined to below $k_H \approx 40\,\mathrm{cm}^{-1}$. Additionally, the $x = 1\,\mathrm{cm}$ spectrum shows some relatively strong activity below $k_H \approx 10\,\mathrm{cm}^{-1}$, indicating some motion into the quiescent region in Fig. 4.6(b). At $t = 15.75\,\mathrm{s}$ and $19.5\,\mathrm{s}$, $x = 1\,\mathrm{cm}$ spectra slowly starts to show more activity from larger and larger wave numbers, while the spectra along the rest of the slices seems to have reached a well-developed state by $t = 15.75\,\mathrm{s}$, as in Fig. 4.6(c). None of the spectra appear to indicate a preferred direction, nor are there any features suggesting a preferred aspect ratio. The primary difference between the kinetic energy spectra and the density spectra is that the kinetic energy spectra at later times show their strongest wave number contributions below $k_H = 20\,\mathrm{cm}$, and display a severe drop in power (about seven orders of magnitude) between $k_H = 0\,\mathrm{cm}$ and $80\,\mathrm{cm}^{-1}$. Meanwhile, the later time density spectra display reasonably strong signals until $k_H = 100\,\mathrm{cm}$, but experience a similar drop in power over a much broader range of wave numbers (from 0 until about $400\,\mathrm{cm}$). The KE spectra exhibit no preference for the direction of the wave numbers, which is a reasonable expectation because the motion of the flow is being driven in the vertical direction by gravity, with no forcing in the horizontal direction. The fact that the density spectra display preferred directions that vary significantly with vertical position and time while the kinetic energy spectra do not is likely due to the increased variability of the long, thin double-diffusive features of the density field which are subject to change from the more rapid, but larger scale and less variable motion of the RT instabilities.

The horizontal 2D spectra of dissipation in Fig. 4.22 show greater intensity at higher wave numbers than the horizontal KE spectra, but lower wave numbers than the density spectra, with signals in the range $k_H \approx 150 - 200\,\mathrm{cm}^{-1}$. These spectra also show similar protrusions to the dominant aspect ratios displayed in the corresponding density spectra of
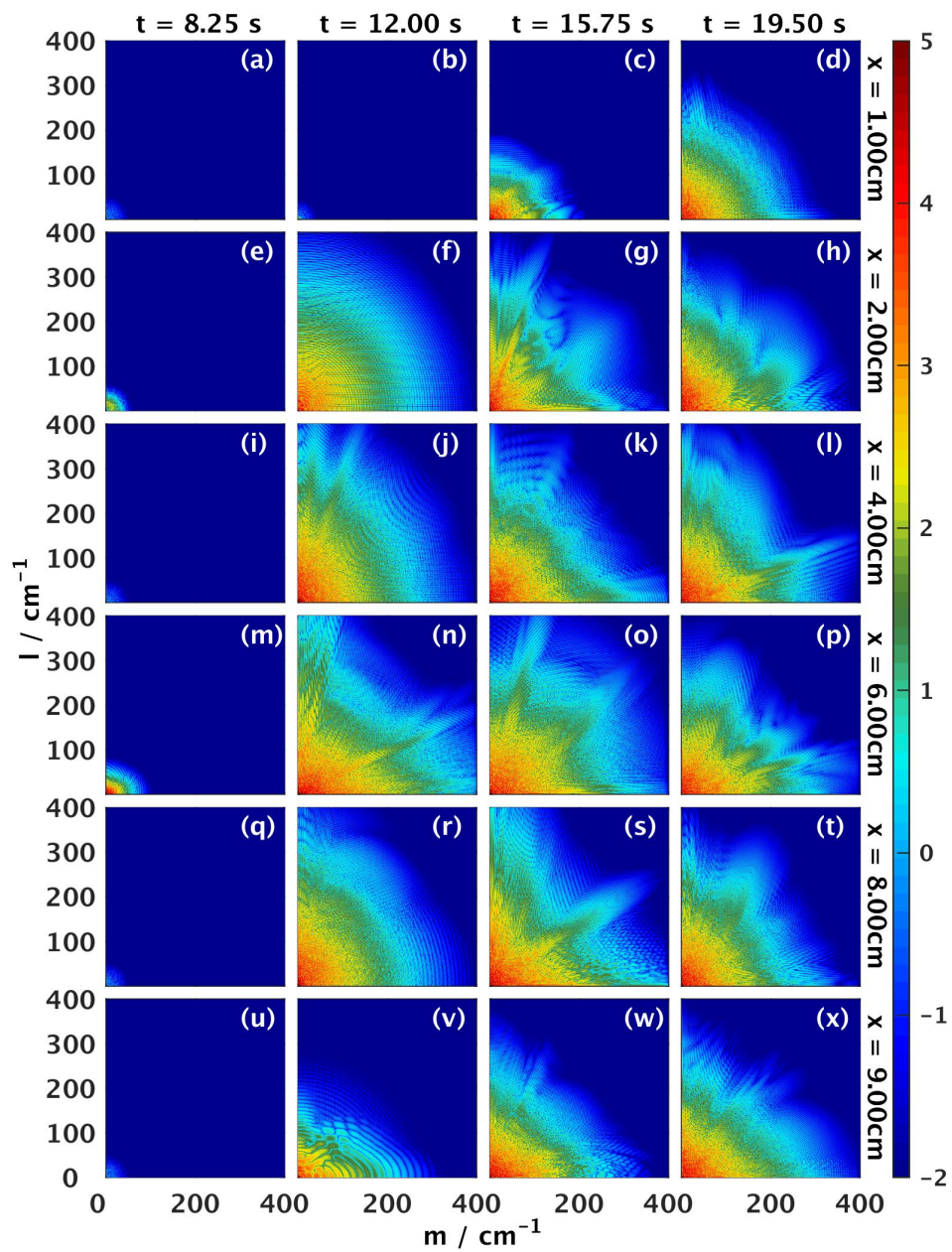
Figure 4.20: Base 10 logarithm of the 2D FFT of density in the yz-plane at various points along the x-axis (top to bottom, $x = 1\,\mathrm{cm}$, $2\,\mathrm{cm}$, $4\,\mathrm{cm}$, $6\,\mathrm{cm}$, $8\,\mathrm{cm}$, $9\,\mathrm{cm}$), at various times (left to right, $t = 8.25\,\mathrm{s}$, $12\,\mathrm{s}$, $15.75\,\mathrm{s}$, $19.5\,\mathrm{s}$).
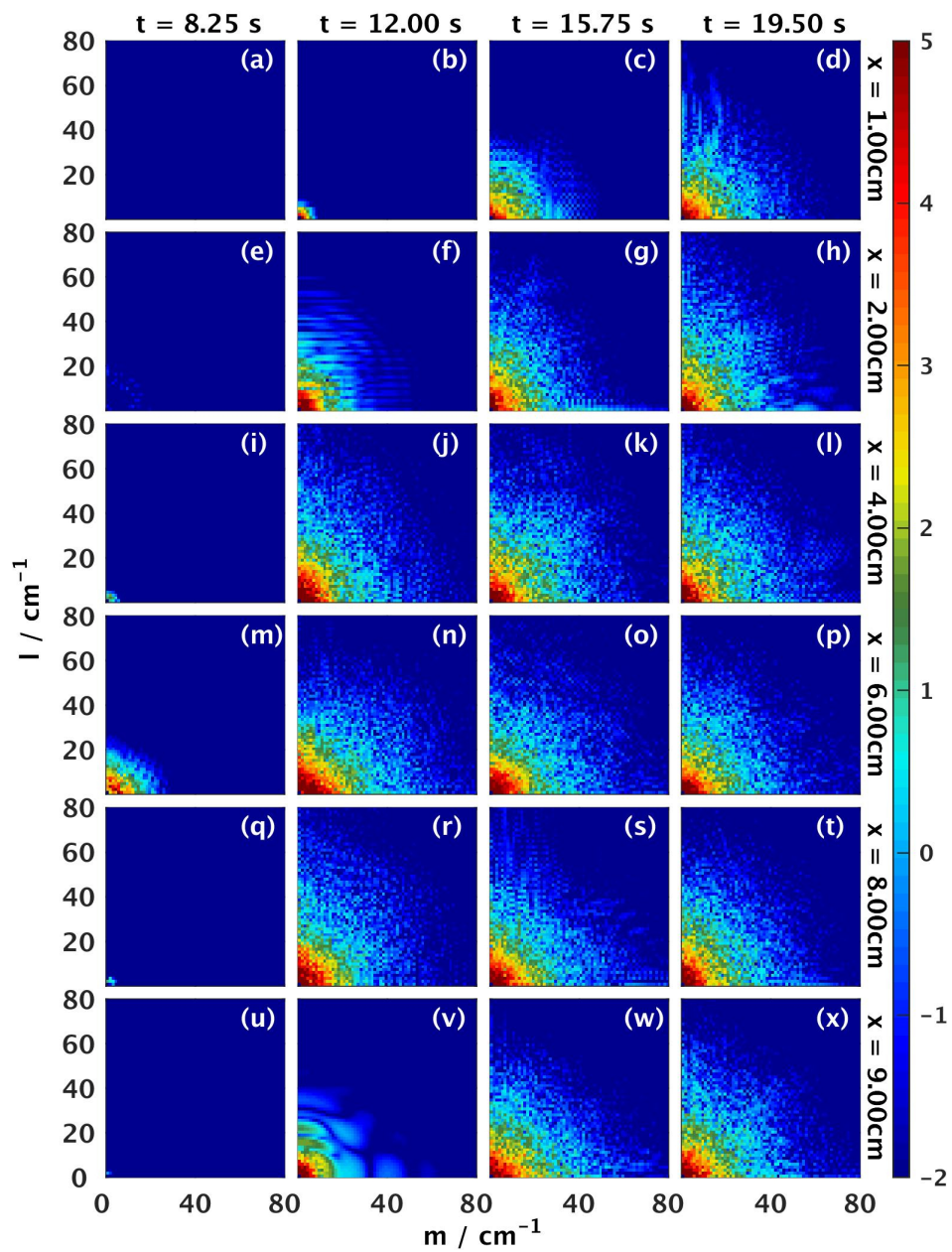
Figure 4.21: Base 10 logarithm of the 2D FFT of kinetic energy in the yz-plane at various points along the x-axis (top to bottom, $x = 1\,\text{cm}$, $2\,\text{cm}$, $4\,\text{cm}$, $6\,\text{cm}$, $8\,\text{cm}$, $9\,\text{cm}$), at various times (left to right, $t = 8.25\,\text{s}$, $12\,\text{s}$, $15.75\,\text{s}$, $19.5\,\text{s}$).

Fig. 4.20, though without the contribution from higher wave numbers. This supports the observations of Fig. 4.10, which shows prominent length scales between the dominant large scales of the KE and the fine scales of the density. It also suggests that some of smaller scale regions of weaker dissipation displayed in Fig. 4.10 may be related to buoyancy effects.

Figs. 4.23 and 4.24 present 2D density spectra along vertical slices in the xz-plane at various points along the y-axis, and in the xy-plane at various points along the z-axis, respectively, at various times. The xz-slices and the xy-slices display very similar general features, which is reasonable since the flow should have no preference between the y- or z-direction. At $t = 8.25\,\text{s}$, each of the spectra show strong contributions from wave numbers below $100\,\text{cm}^{-1}$, with a slight preference towards the vertical wave number. By $t = 12\,\text{s}$, there are increased contributions from all wave numbers below $400\,\text{cm}^{-1}$, as in the later time horizontal slices of Fig. 4.20, with no apparent preference for the vertical or horizontal wave numbers. The vertical spectra also show higher intensity at larger wave numbers than shown by the horizontal spectra in Fig. 4.24.

The 2D spectra of kinetic energy in the vertical direction are presented in Figs. 4.25 (slices in xz-plane at various points along the y-axis) and 4.26 (slices in xy-plane at various points along the z-axis), and evolve similarly to the density spectra of Figs. 4.23 and 4.24. Each slice at $t = 8.25\,\text{s}$ shows some activity from low wave numbers, with a slight preference for the vertical direction. By $t = 12\,\text{s}$, each of the spectra appear to have reached a well-developed state, showing strong contributions from wave numbers below $50\,\text{cm}^{-1}$. There also appears to be a slight preference towards higher horizontal wave numbers (with lower vertical wave numbers) at later times. This suggests that the dominant KE features at later times along vertical slices have larger vertical scales than they do horizontal scales. This aligns with the RT instabilities, stretching vertically as they rise and fall, resulting in larger vertical scales than horizontal scales.

To better examine the rate at which the intensities of the 2D spectra decay with increasing wave number, the directional information can be removed from the 2D spectra, so instead the spectra can be expressed as functions of the magnitude of a 2D wave number vector. This is achieved by plotting the intensity at arbitrary two-dimensional wave number vector $\left(k_{x_i}, k_{x_j}\right)$ from the 2D spectrum as a 1D function at the corresponding wave number magnitude $k_{x_i x_j} = \sqrt{k_{x_i}^2 + k_{x_j}^2}$. In the subsequent spectra plotted in this section, these are the values given by the red dots. Given that multiple wave number vectors can produce the same value of $k_{x_i x_j}$, this means that there will be multiple intensities plotted for a single wave number magnitude. To obtain a better estimate of the shape of the spectrum, the wave number magnitude domain is subdivided into multiple bins of width Δk. For a given bin starting at k_0, $[k_0, k_0 + \Delta k]$, all the contributions from wave numbers
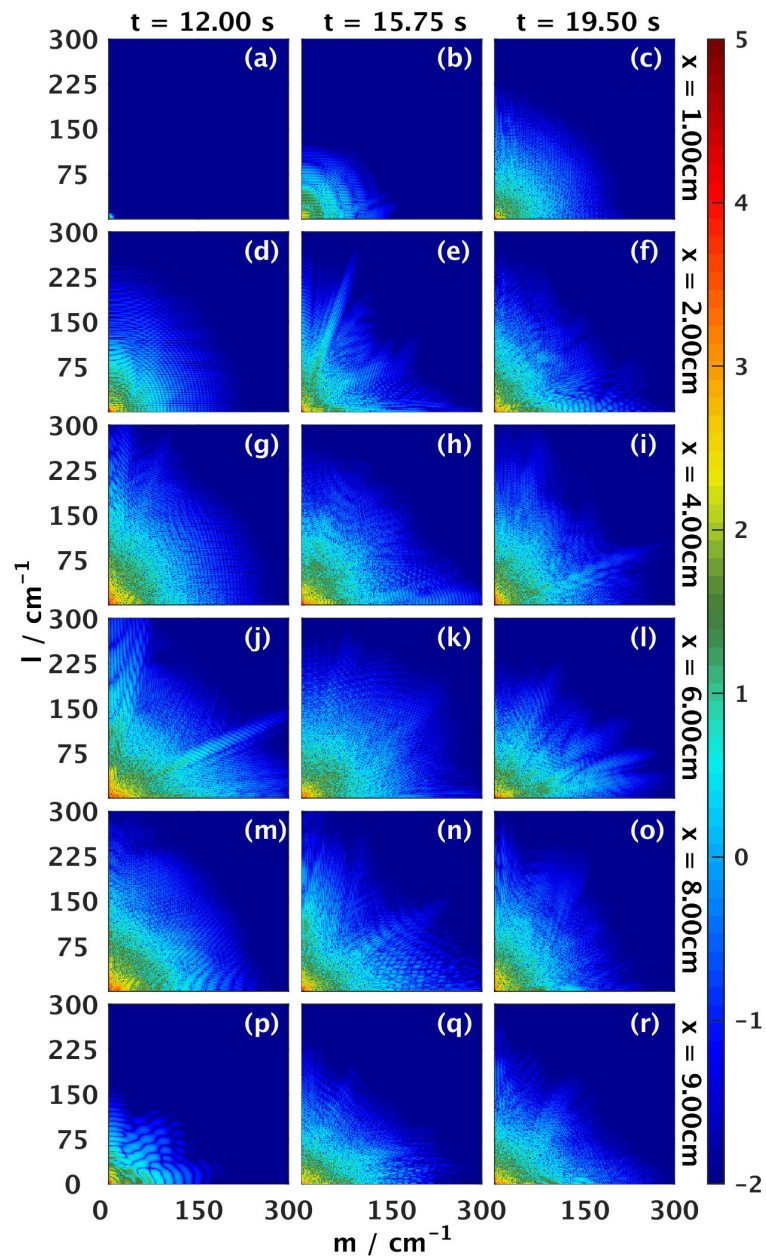
Figure 4.22: Base 10 logarithm of the 2D FFT of dissipation in the yz-plane at various points along the x-axis (top to bottom, $x = 1\,\mathrm{cm}$, $2\,\mathrm{cm}$, $4\,\mathrm{cm}$, $6\,\mathrm{cm}$, $8\,\mathrm{cm}$, $9\,\mathrm{cm}$), at various times (left to right, $t = 12\,\mathrm{s}$, $15.75\,\mathrm{s}$, $19.5\,\mathrm{s}$).
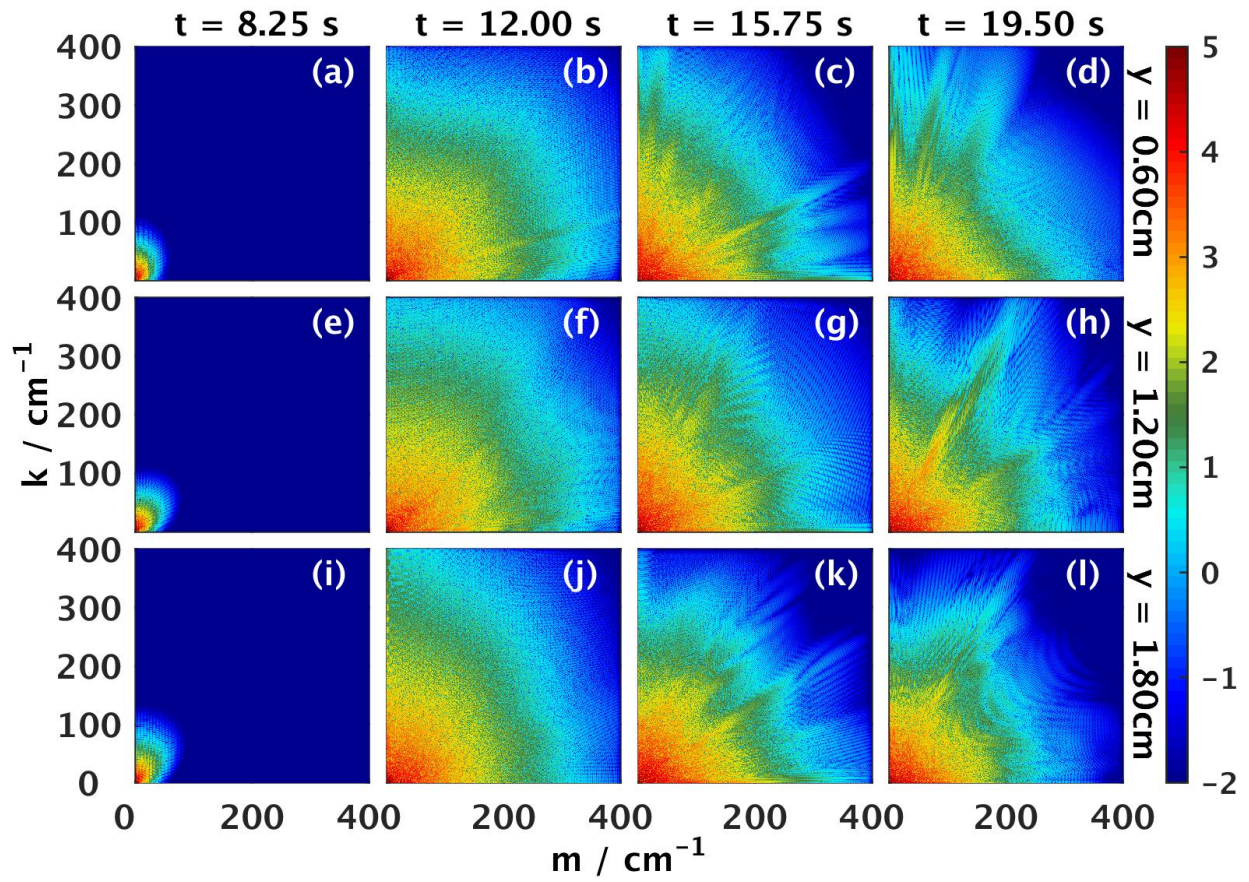
Figure 4.23: Base 10 logarithm of the 2D FFT of density in the xz-plane at various points along the y-axis.
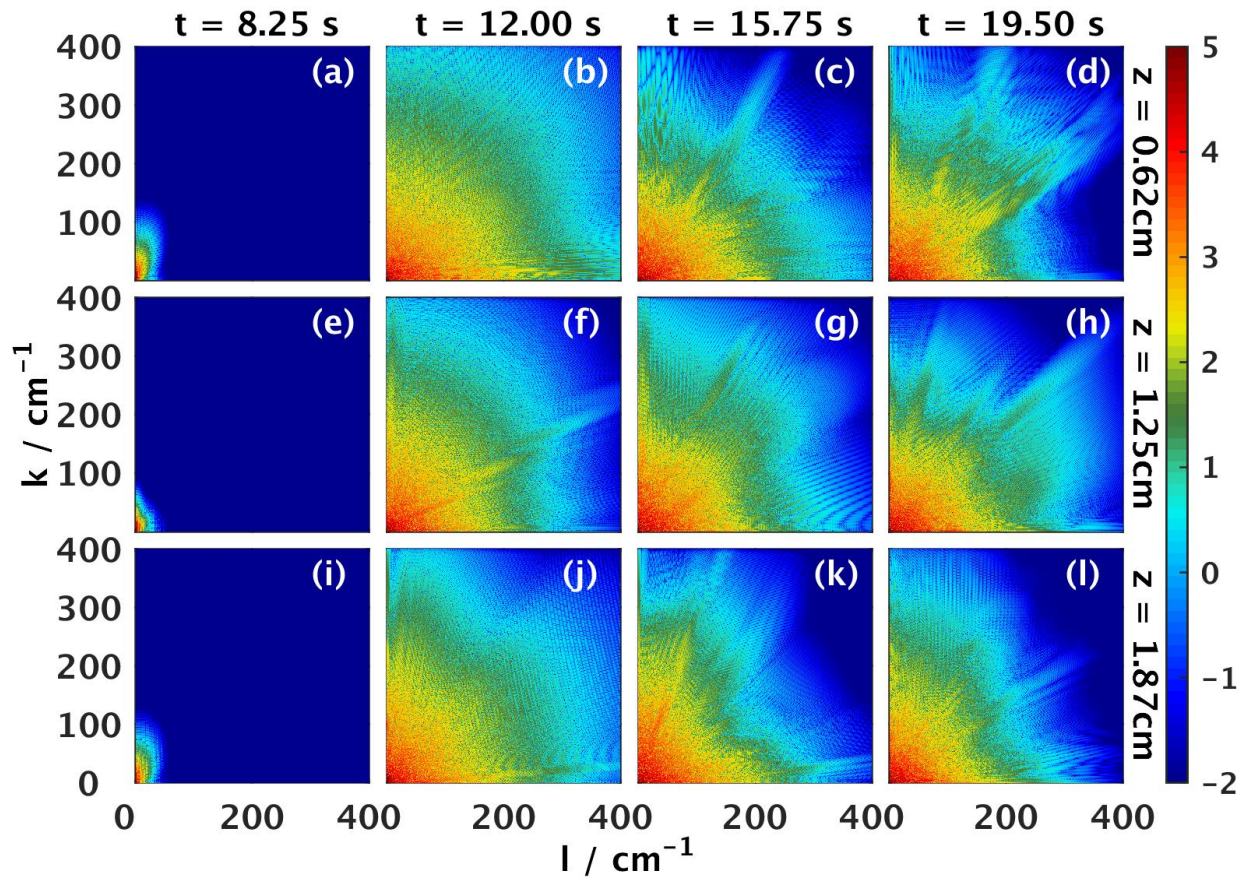
Figure 4.24: Base 10 logarithm of the 2D FFT of density in the xy-plane at various points along the z-axis.
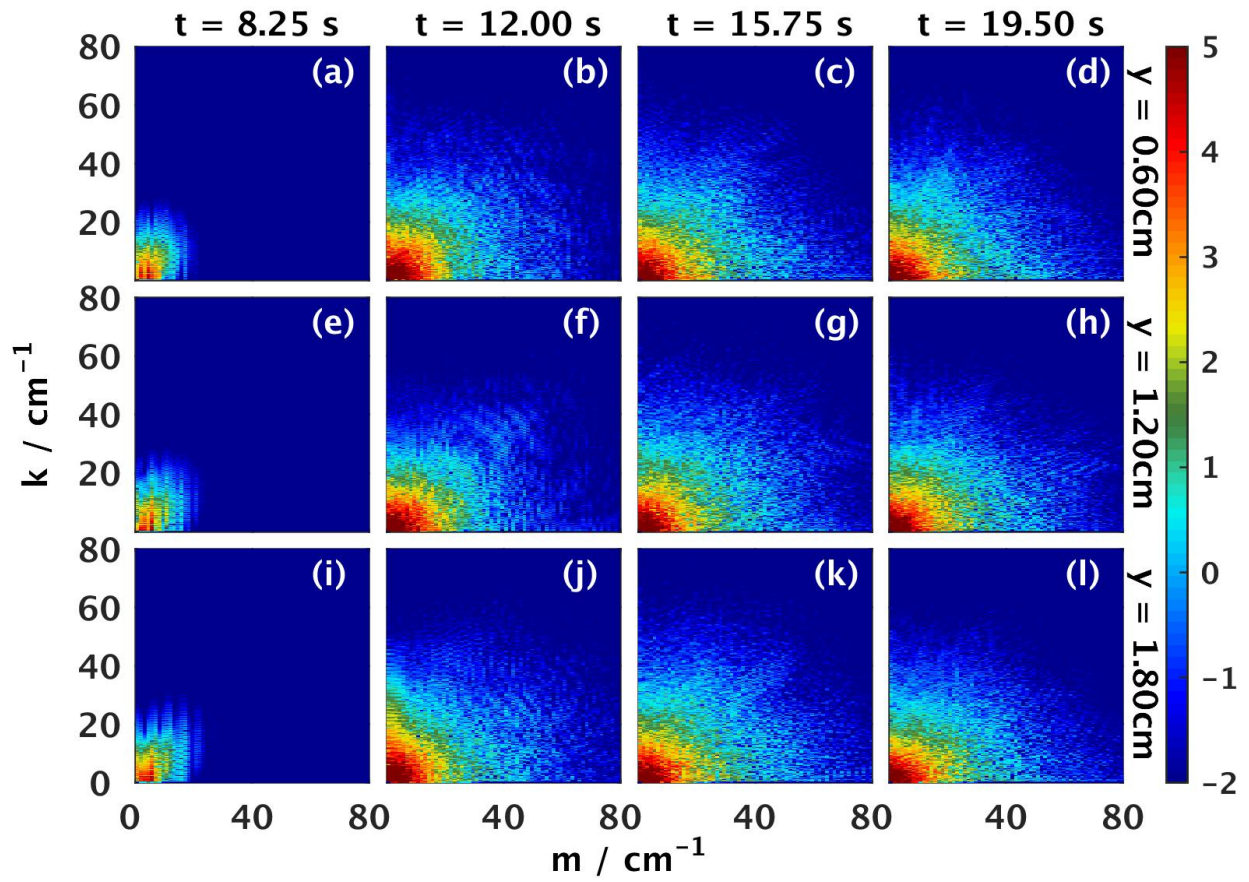
Figure 4.25: Base 10 logarithm of the 2D FFT of kinetic energy in the xz-plane at various points along the y-axis.
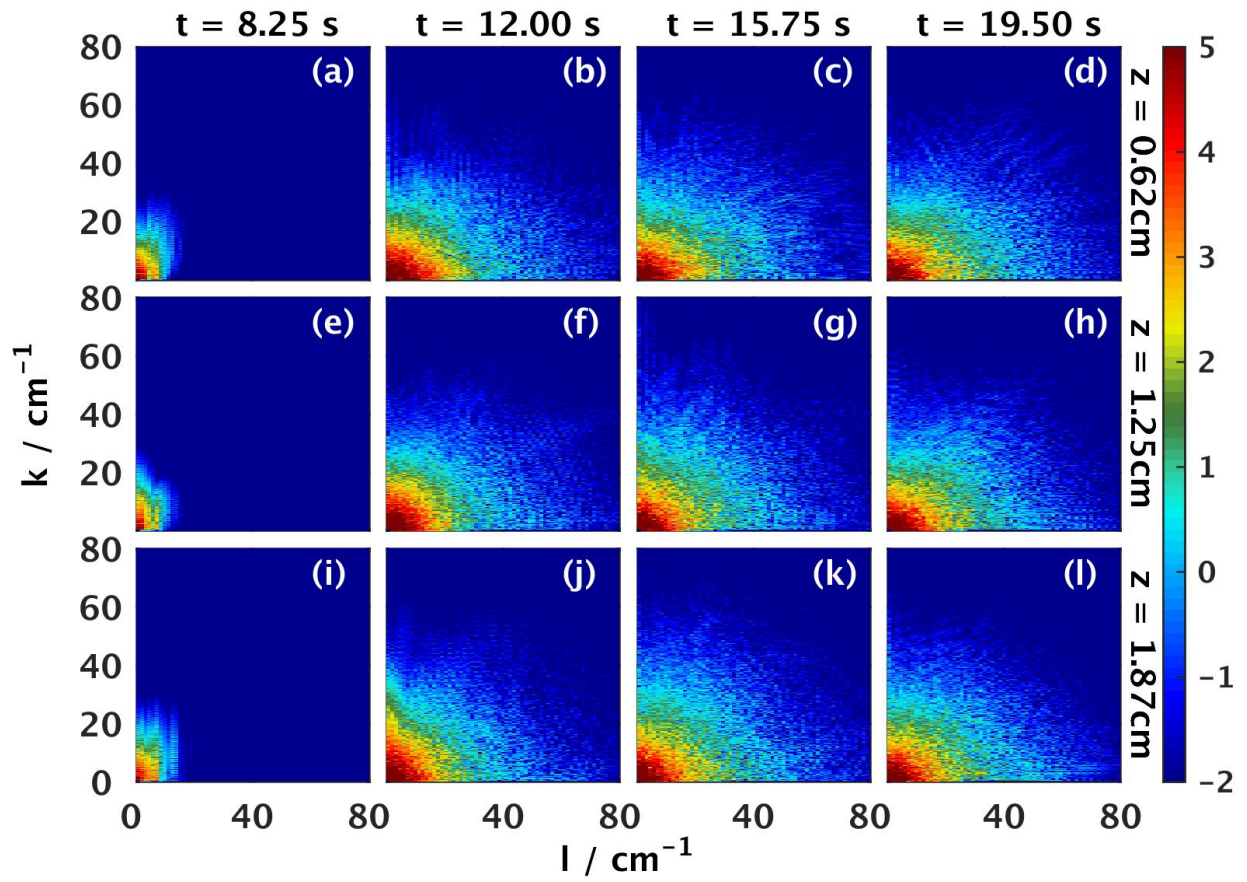
Figure 4.26:   Base 10 logarithm of the 2D FFT of kinetic energy in the xy-plane at various points along the z-axis.

residing in the bin are averaged, with the resulting mean plotted at $k_0 + \frac{1}{2}\Delta k$ as a blue circle in the subsequent spectra. This is equivalent to subdividing the two-dimensional spectra into annular shells, then averaging over each of the shells. In the spectra that follow, 100 bins were used, with $\Delta k = 643\,\mathrm{m}^{-1}$.

In each of the spectra plotted below, the dashed lines indicate an estimate of the wave number corresponding to the Kolmogorov microscale,

$$\eta = \left(\frac{\nu^3}{\epsilon}\right)^{1/4}, \tag{4.7}$$

the scale at which viscous effects become important, where ϵ is a measure of dissipation, and ν is the viscosity of the fluid. Though simulations of homogeneous turbulence may use a volume average as an estimate of the dissipation scale, the inhomogeneity of the dissipation field in this simulation prevents a reasonable estimate using the mean. A key assumption in turbulence theory is that the dissipation scale of turbulent flow depends only on the length and velocity scales of eddies in the flow. Therefore, ϵ can be calculated using estimates of the velocity scale, U, and the length scale, L, of larger features of the flow as

$$\epsilon = \frac{U^3}{L}. \tag{4.8}$$

Through visual inspection the density fields of $t = 9.5\,\mathrm{s}$ and $t = 12\,\mathrm{s}$ of Fig. 4.4, a typical velocity of rising or sinking RT instabilities was estimated to be on the order of $U = 1\,\mathrm{cm/s}$. Estimating the typical width of an RT instability to be on the order of $L = 1\,\mathrm{cm}$, this provides an estimate of $\epsilon = 1 \times 10^{-4}\,\mathrm{m}^2/\mathrm{s}^3$ for the viscous dissipation. With the viscosity used in this simulation, $\nu = 2 \times 10^{-6}\,\mathrm{m}^2/\mathrm{s}$, the resulting estimate of the Kolmogorov microscale is $\eta = 5.32 \times^{-2}$ cm. The resulting estimate of the Kolmogorov wave number is $k_\eta = 2\pi/\eta = 118\,\mathrm{cm}^{-1}$.

In accordance with classical turbulence theory, estimates of the slopes of the linear regimes of the log-log plots of the annularly-averaged spectra were calculated, in order to determine how the spectra behave with increasing wave number magnitude. The slopes representing the decrease in signal strength in the kinetic energy, salinity, and density spectra were estimated by performing a linear polynomial fit from $k_H = 29\,\mathrm{cm}^{-1}$ to $113\,\mathrm{cm}^{-1}$. This choice of region over which to estimate the slopes was entirely subjective, and based on trial and error. Due to the shape of the curve, extending the region too far past the Kolomogorov scale resulted in an attempt to linearize over a regime that was clearly non-linear, giving slopes with unrealistically high magnitudes. Because this flow does not give way to fully-developed turbulence, these lines give an estimate of the decrease in strength of the contributions of increasing wave numbers. It is therefore not expected that the

slopes will reflect the results of classical turbulence theory, such as the $-5/3$-law in the inertial subrange of the KE spectrum, or the -1-law in the viscous-convective subrange of the tracer fields [100].

As a brief note, the horizontal axes of Figs. 4.27-4.33 are given as the logarithm of the wave number magnitude in m^{-1}.

The slopes of the KE spectra presented in Fig. 4.27 reflect the information presented by the 2D KE spectra of Fig. 4.21, in that there is a rapid drop in contribution to kinetic energy as the wave number magnitude increases, with slopes ranging from -7.5 to -9.6. In contrast, the density spectra in Fig. 4.28 show a much weaker drop in contribution to the density field as wave number magnitude increases, with estimated slopes ranging from -1.7 to -3.0. As with the previous 2D spectra, the behaviour of the density spectra is strongly reflected by the salinity spectra in Fig. 4.29, which exhibit similar slopes along each of the slices. The temperature spectra of Fig. 4.30 appear to display two distinct regions where the power of the spectra decreases nearly linearly. Below $k_H = 10^{1.5}$ cm^{-1}, the temperature spectra of Fig. 4.30 decrease nearly linearly and rather slowly. Above $10^{1.5}$ cm^{-1}, there is a second nearly linear region that continues past k_η that decreases much more rapidly. The slope of the slowly decreasing region was estimated by performing a linear polynomial fit from $k_H = 3.2$ cm^{-1} to 29 cm^{-1}, while the slope of the rapidly decreasing region was estimated by performing a linear polynomial fit from $k_{yz} = 48$ cm^{-1} to 229 cm^{-1}. In the slowly decreasing region of the temperature spectra, the slopes range from -1.6 to -2.1, while in the rapidly decreasing region, they range from -8.3 to -10.4. The KE spectra display a much greater relative decrease in intensity with respect to wave number than either the tracer fields, from about from 10^7 to 10^{-30} (far below numerical precision), compared to a decrease of about 10^7 to 10^{-10}.

Fig. 4.31 gives the viscous dissipation spectra as a function of k_H, with slopes estimating the decay rate calculated from $k_H = 29$ cm^{-1} to 113 cm^{-1}. These slopes range from -2.4 to -4.1, with values from the slices away from the boundaries tending towards -3.0. Overall, this is a more rapid decay than the rates estimated for the salinity and density fields, but slower than the decay exhibited by the kinetic energy and temperature fields.

Figs. 4.32 and 4.33 present kinetic energy spectra of vertical slices along the xz-plane at various points in the y-direction, and along the xy-plane at various points in the z-direction, respectively. The slopes were estimated in the same way as for the horizontal spectra, with values ranging from -7.8 to -8.5 for the xz-slices, and -8.1 to -8.8 for the xy-slices. These values are similar to those calculated for the horizontal spectra.
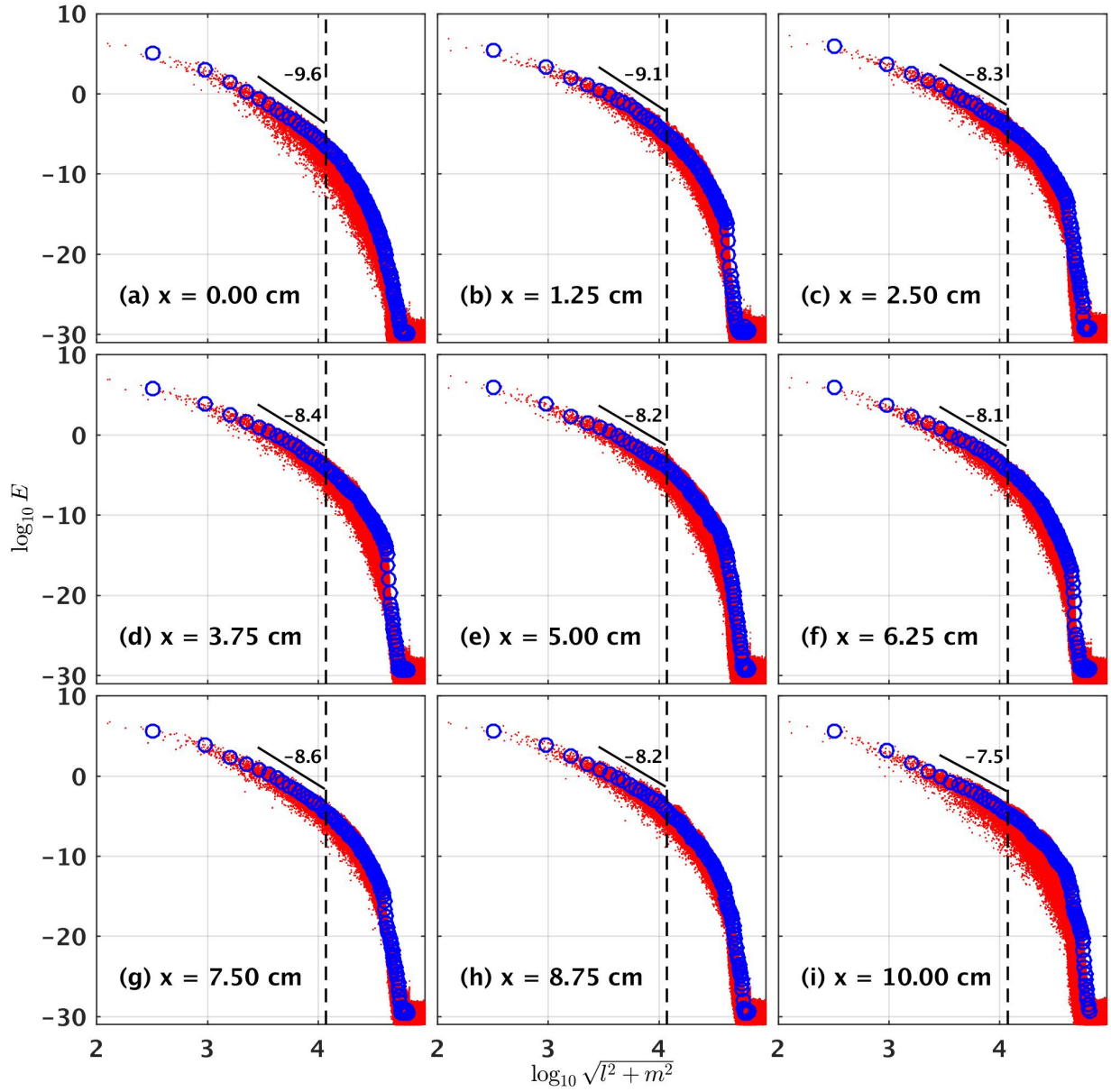
Figure 4.27: Base 10 logarithm of the kinetic energy spectrum slices in the yz-plane along various values of x as a function of $\log_{10}\sqrt{l^2+m^2}$. The dashed line indicates the wave number corresponding to the estimate of the Kolmogorov scale, $2\pi/\eta$. The red dots indicate the contribution to KE from each individual wave number, while the blue circles indicate the mean value within a given bin.
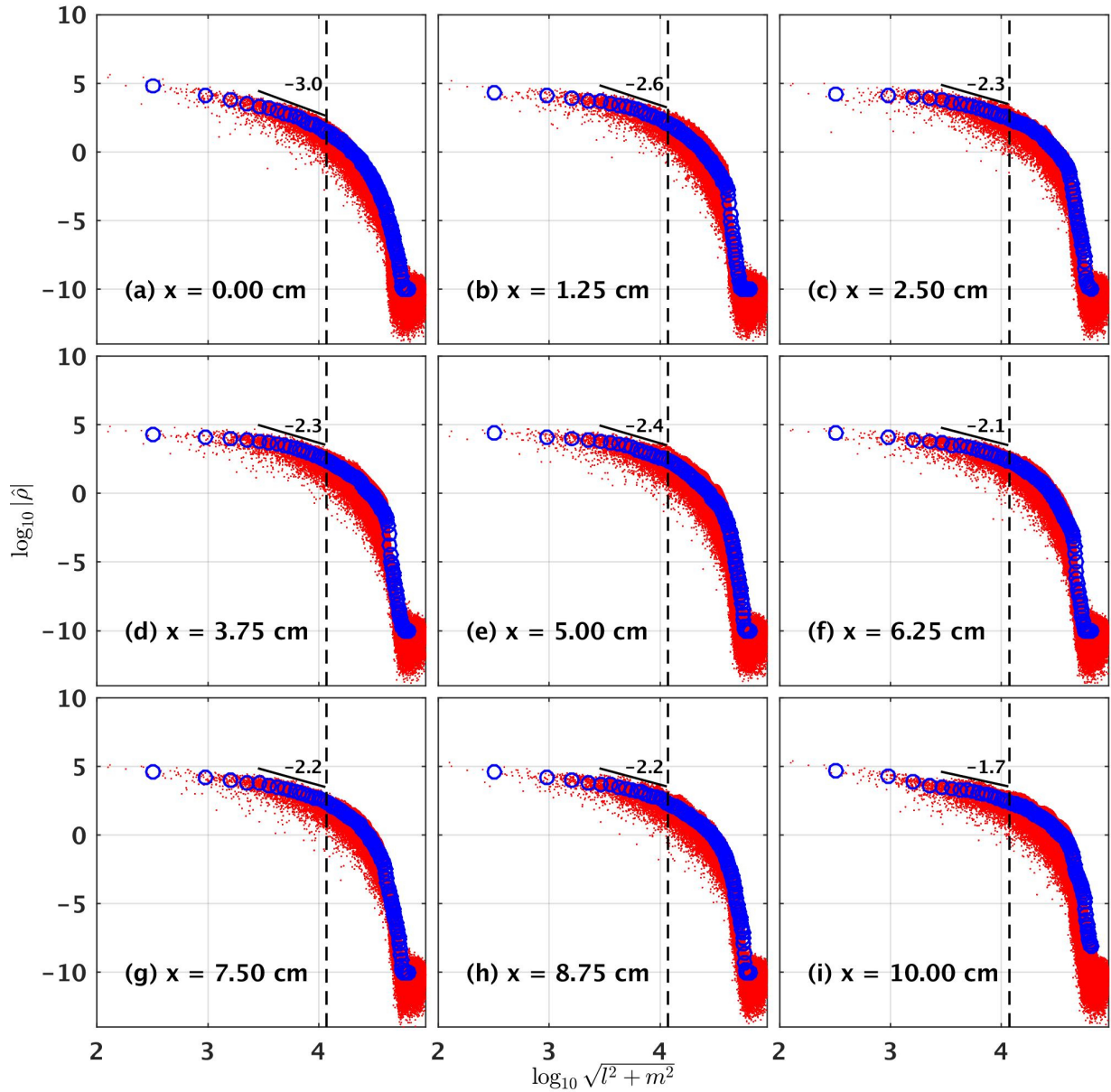
Figure 4.28: Base 10 logarithm of the density spectrum slices in the yz-plane along various values of x as a function of $\log_{10} \sqrt{l^2 + m^2}$. The dashed line indicates the wave number corresponding to the estimate of the Kolmogorov scale, $2\pi/\eta$. The solid line indicates the slope of the nearly linear region to the left of the Kolmogorov wave number.
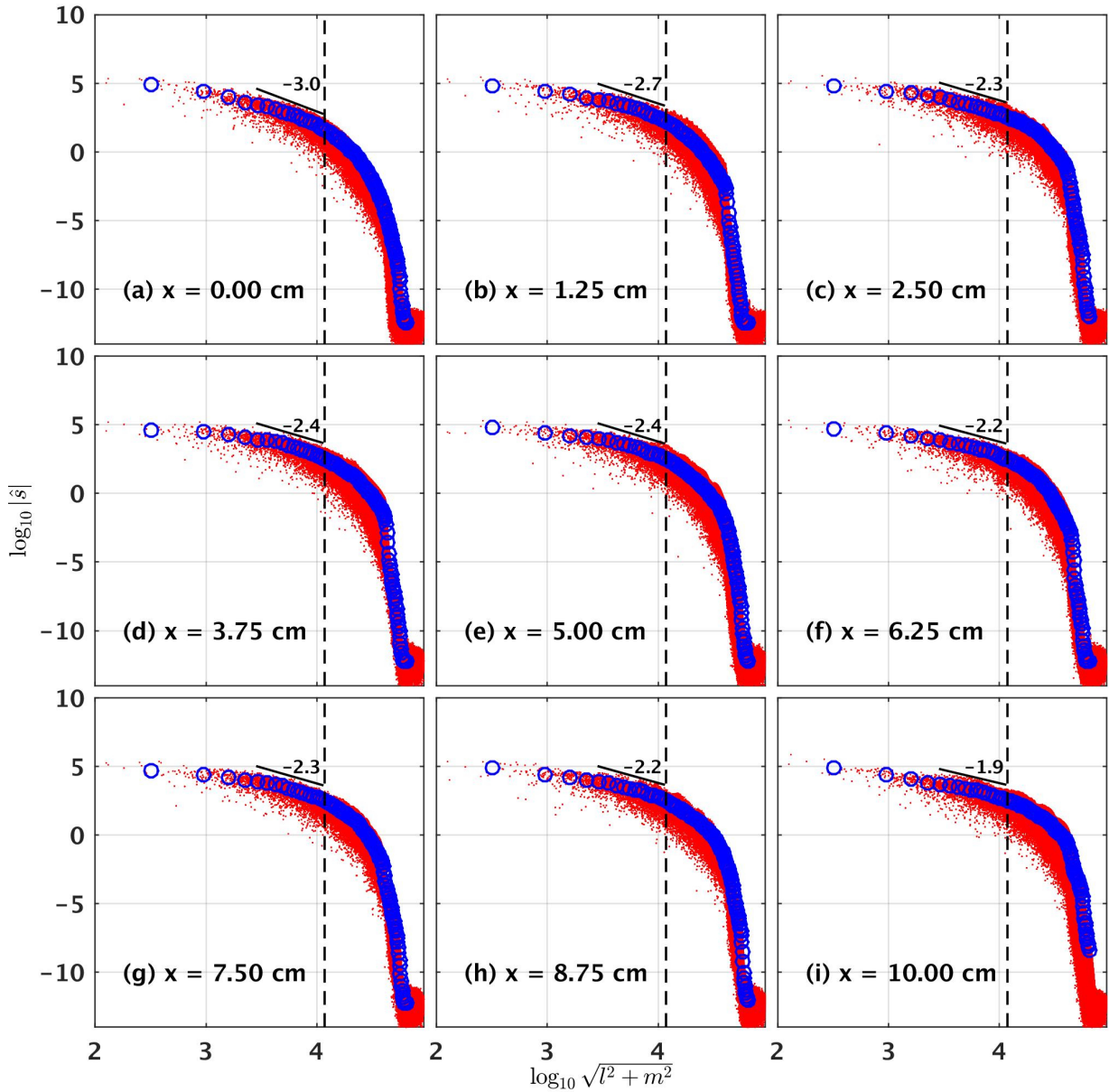
Figure 4.29: Base 10 logarithm of the salinity spectrum slices in the yz-plane along various values of x as a function of $\log_{10}\sqrt{l^2+m^2}$. The dashed line indicates the wave number corresponding to the estimate of the Kolmogorov scale, $2\pi/\eta$. The solid line indicates the slope of the nearly linear region to the left of the Kolmogorov wave number.

113
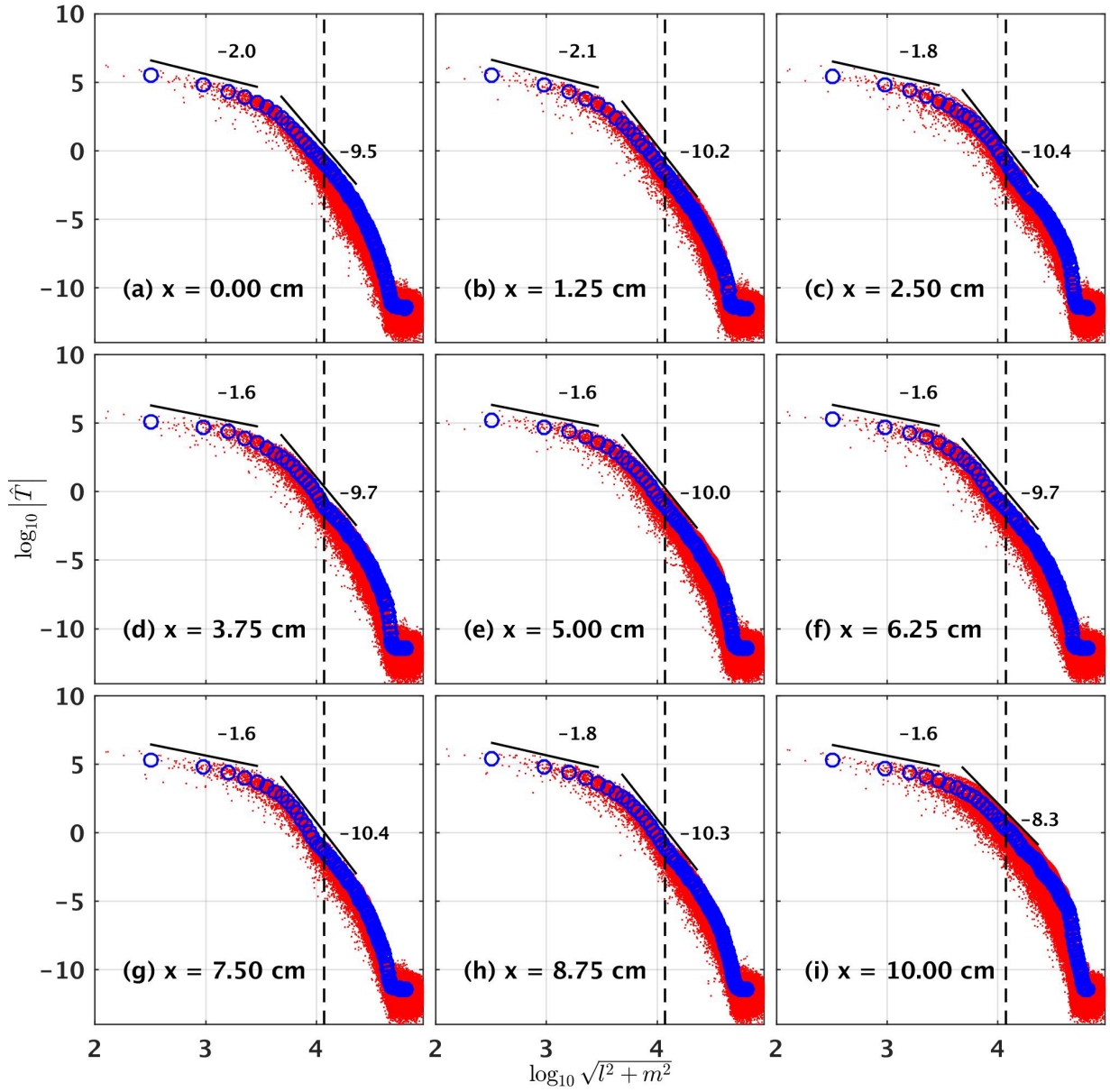
Figure 4.30: Base 10 logarithm of the temperature spectrum slices in the yz-plane along various values of x as a function of $\log_{10} \sqrt{l^2 + m^2}$. The dashed line indicates the wave number corresponding to the estimate of the Kolmogorov scale, $2\pi/\eta$. The solid lines indicate the approximate slopes of the spectra in the slowly decreasing region and the rapidly decreasing region.

114
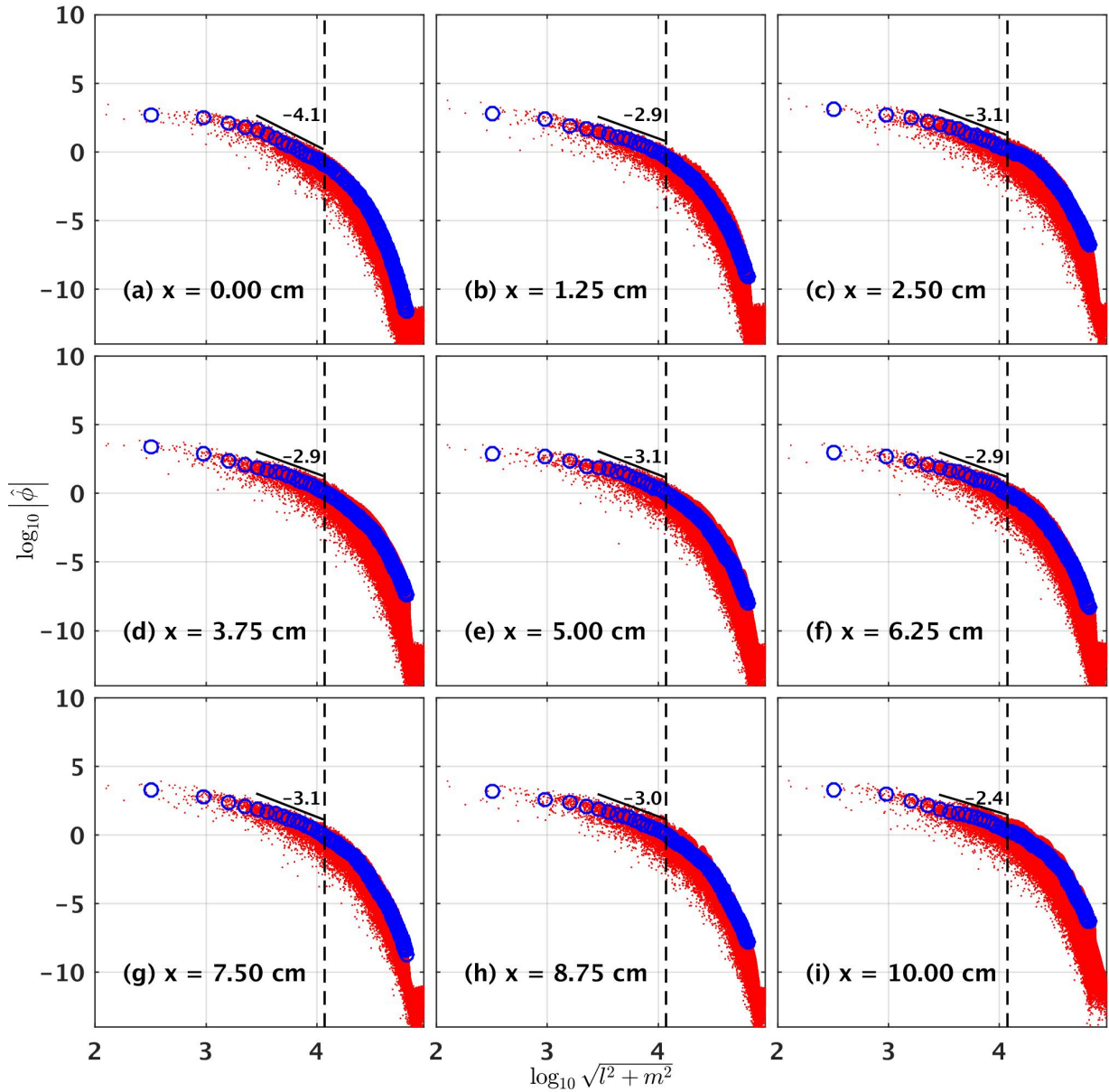
Figure 4.31: Base 10 logarithm of the dissipation spectrum slices in the yz-plane along various values of x as a function of $\log_{10}\sqrt{l^2 + m^2}$. The dashed line indicates the wave number corresponding to the estimate of the Kolmogorov scale, $2\pi/\eta$. The solid line indicates the slope of the nearly linear region to the left of the Kolmogorov wave number.
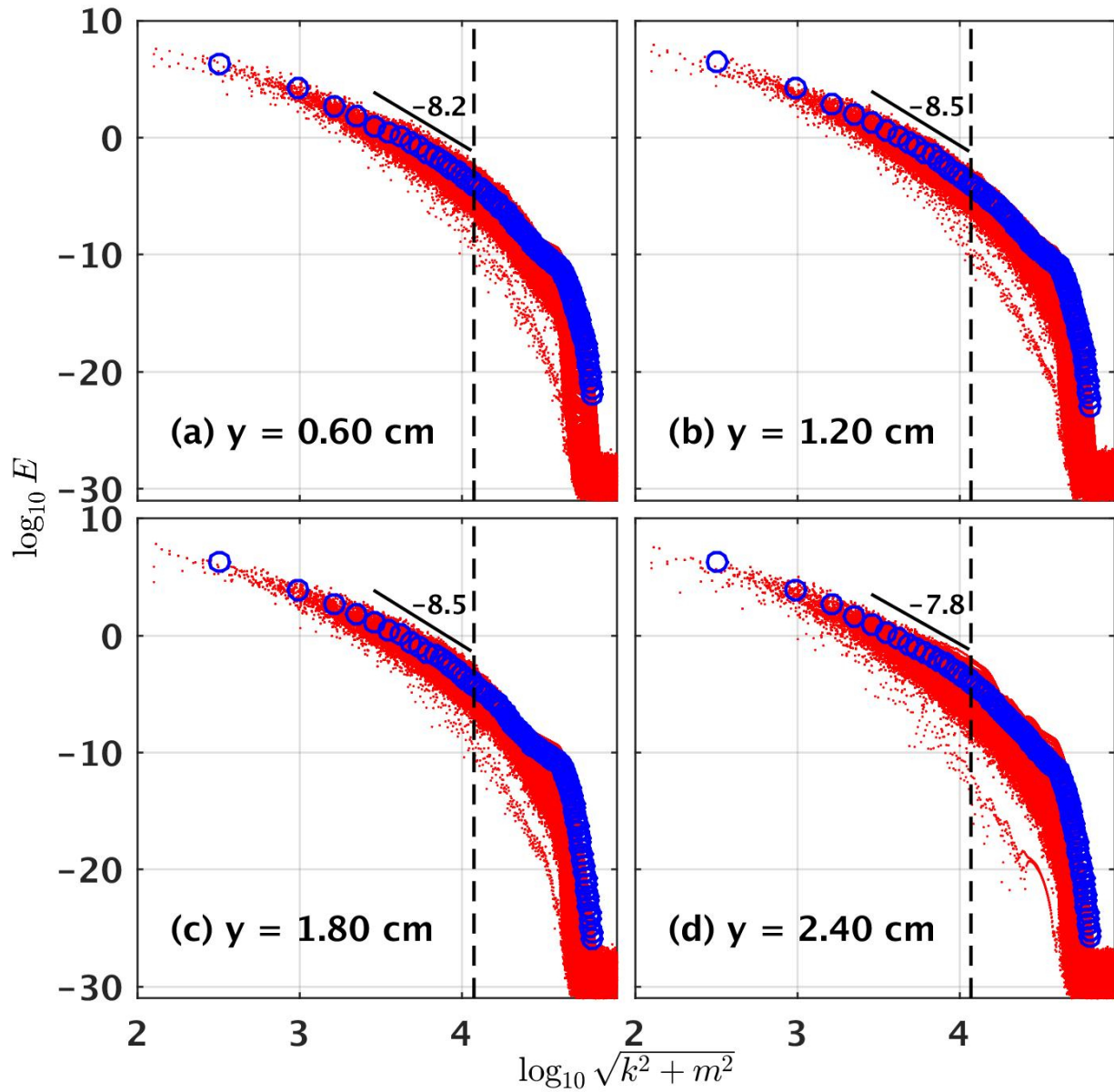
Figure 4.32: Base 10 logarithm of the kinetic energy spectrum slices in the xz-plane along various values of y as a function of $\log_{10}\sqrt{k^2 + m^2}$. The red dots indicate the contribution to KE from each individual wave number, while the blue circles indicate the mean value within a given bin.
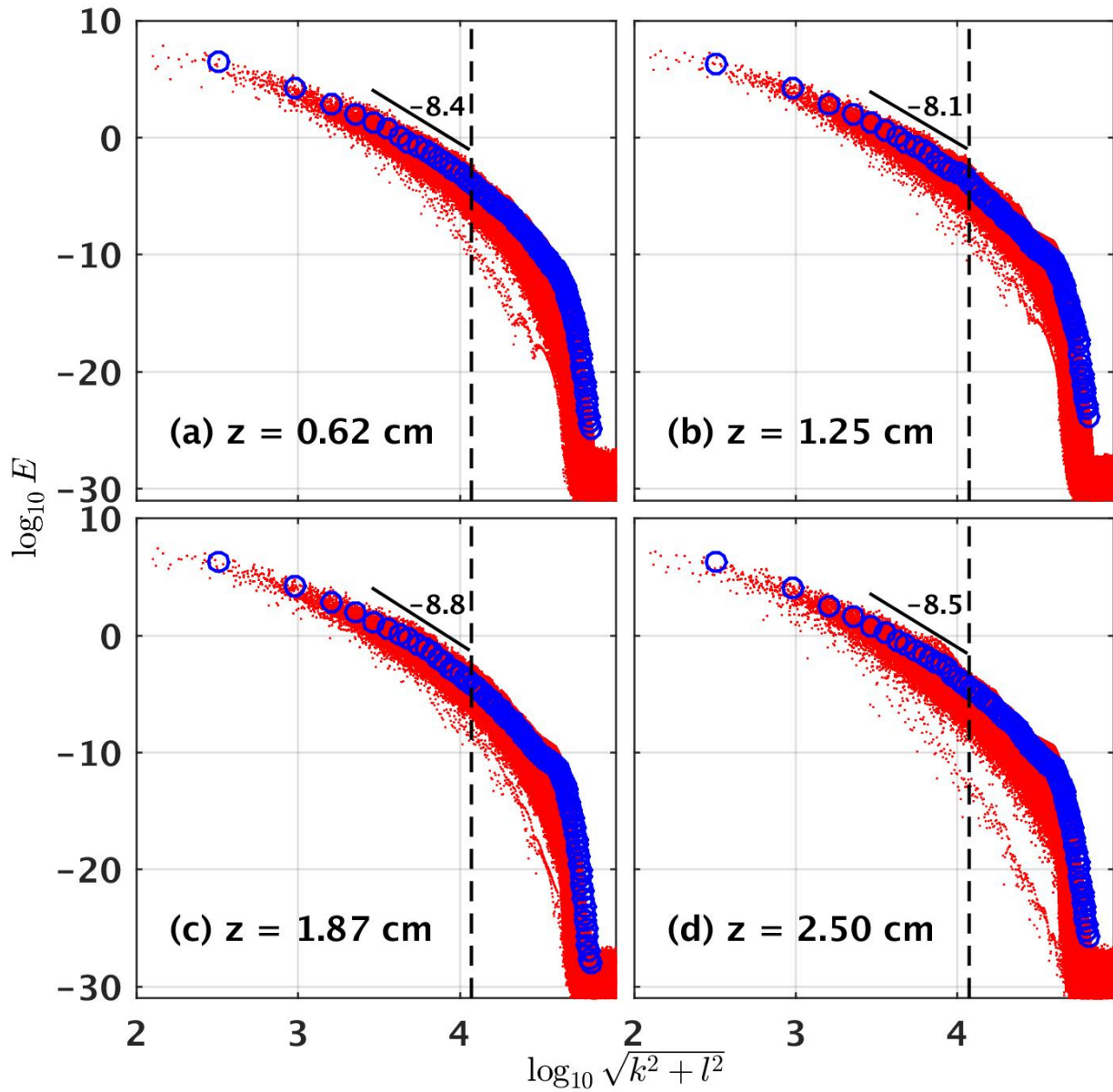
Figure 4.33: Base 10 logarithm of the kinetic energy spectrum slices in the xy-plane along various values of z as a function of $\log_{10} \sqrt{k^2 + l^2}$. The red dots indicate the contribution to KE from each individual wave number, while the blue circles indicate the mean value within a given bin.

4.5.2 Filtering the Density Data

In order to isolate the large and small scale features (or, in spectral space, the low and high wave number components, respectively) of the density fields, two separate filters were applied to the two-dimensional Fourier transform of a slice of the density in the xz-plane, $\hat{\rho}(k, y, m)$. The first is a low pass filter, designed to eliminate contributions from wave numbers above a cutoff wave number k_C, and maintain the contributions from the low wave number components below the cutoff,

$$f_{\text{Low}}(r) = \frac{1}{2} - \frac{1}{2} \tanh \left(\frac{r - k_C}{dk} \right), \tag{4.9}$$

where dk sets how quickly the filter transitions from unfiltered to filtered wave numbers, and $r^2 = k^2 + m^2$. Similarly, a high pass filter,

$$f_{\text{High}}(r) = \frac{1}{2} + \frac{1}{2} \tanh \left(\frac{r - k_C}{dk} \right), \tag{4.10}$$

was designed to eliminate the contribution from wave numbers below k_C while maintaining the contribution from wave numbers above k_C. Note that $f_{\text{Low}} + f_{\text{High}} = 1$. Letting $\mathcal{F}$ and $\mathcal{F}^{-1}$ represent the Fourier transform and inverse Fourier transform operators, respectively, the Fourier transform of density can be expressed as

$$\mathcal{F}\{\rho\} = \hat{\rho} = (f_{\text{Low}} + f_{\text{High}}) \hat{\rho} = f_{\text{Low}}\hat{\rho} + f_{\text{High}}\hat{\rho}. \tag{4.11}$$

From this, and using the linearity of the Fourier transform, the density can be shown to be equal to the sum of a low frequency component $\rho_{\text{Low}} = \mathcal{F}^{-1}\{f_{\text{Low}}\hat{\rho}\}$ and high frequency component $\rho_{\text{High}} = \mathcal{F}^{-1}\{f_{\text{High}}\hat{\rho}\}$,

$$\rho = \mathcal{F}^{-1}\{\hat{\rho}\} = \mathcal{F}^{-1}\{f_{\text{Low}}\hat{\rho} + f_{\text{High}}\hat{\rho}\} = \mathcal{F}^{-1}\{f_{\text{Low}}\hat{\rho}\} + \mathcal{F}^{-1}\{f_{\text{High}}\hat{\rho}\} = \rho_{\text{Low}} + \rho_{\text{High}}. \tag{4.12}$$

As per the two-dimensional spectra of kinetic energy presented in Fig. 4.25, the most significant contributions to KE come from wave numbers below $20\,\text{cm}^{-1}$, while the two-dimensional spectra of density in Fig. 4.23 show relatively strong contributions to ρ from wave numbers above $100\,\text{cm}^{-1}$. Using the dominant wave numbers of KE as an estimate of the larger length scales, k_C was set to $10\,\text{cm}^{-1}$, with $dk = 1\,\text{cm}^{-1}$. The resulting low- and high-pass filters are presented in panels (a) and (b) of Fig. 4.34. Applying these filters to slices of density in the xz-plane along $y = 0.60\,\text{cm}$ at $t = 12\,\text{s}$, $15.75\,\text{s}$, and $19.5\,\text{s}$, gives the fields presented in Fig. 4.35, with the result of the application of the high pass filter in the
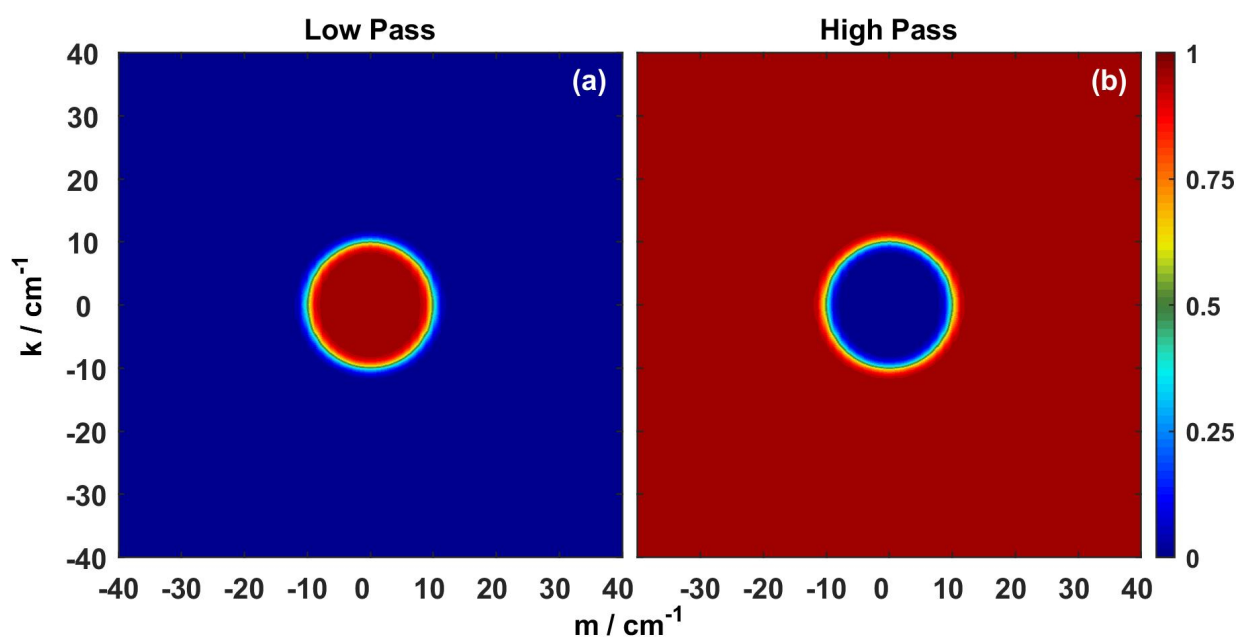
Figure 4.34:   Contour plots of the two-dimensional filters defined by (a) equation 4.9 and (b) equation 4.10.

top row, and the result of the low pass filter in the bottom row. The white contour lines indicate kinetic energy levels of $4 \times 10^{-5}\,\mathrm{m^2/s^2}$, and trace some of the larger scale features present in the low pass filtered density fields. Additionally, comparing Figs. 4.35 (b), (d), and (f) with the kinetic energy slices in Figs. 4.5 (b), (d), and (f), seems to indicate correspondence between the low pass filtered density features and the primary kinetic energy features. The low-pass density fields display density magnitudes similar to those presented in the unfiltered density fields in Fig. 4.5, and could be considered more indicative of the mean flow. The low-pass field also manages to capture regions where the density is higher (lower) than the initial maximum (minimum), which are only possible because of double-diffusion. The high-pass fields are reflective of small magnitude fluctuations resulting from double-diffusive effects, which are less than 0.25% of the magnitude of the low-pass densities. The high-pass fields could be considered a perturbation to the mean.

In the context of large-eddy simulation (LES), variables are separated into two parts

$$\rho = \tilde{\rho} + \rho', \tag{4.13}$$

where $\tilde{\rho}$ is the resolvable (or filtered) part of the density field, and ρ' is the subfilter part of the field. These would correspond to ρ_{Low} and ρ_{High} from above, respectively. When applying spatial filters to the equations of motion for LES, the filtered nonlinear advection terms are dependent on the subfilter parts of the field, through terms referred to as subfilter-scale fluxes [116]. The method of filtering DNS results examined here may be useful for the parameterization of subfilter-scale fluxes based on double-diffusive processes that may be considered subgrid-scale when modelling larger scale geophysical flows through LES.

4.6   Summary

High-resolution DNS was employed to examine the formation of double-diffusive Rayleigh-Taylor instabilities in a three-layer system. In particular, it was observed that:

1. In two-dimensional simulations of single-diffusive systems, typical RT instabilities were observed to form, with the width of the interface between the high and low density fluids set by the tracer diffusivity. In contrast, a two-dimensional simulation of a double-diffusive system experienced the formation of double layers between the high and low density fluids. This indicates that the motion was primarily due to the RT and not the double-diffusive instabilities.
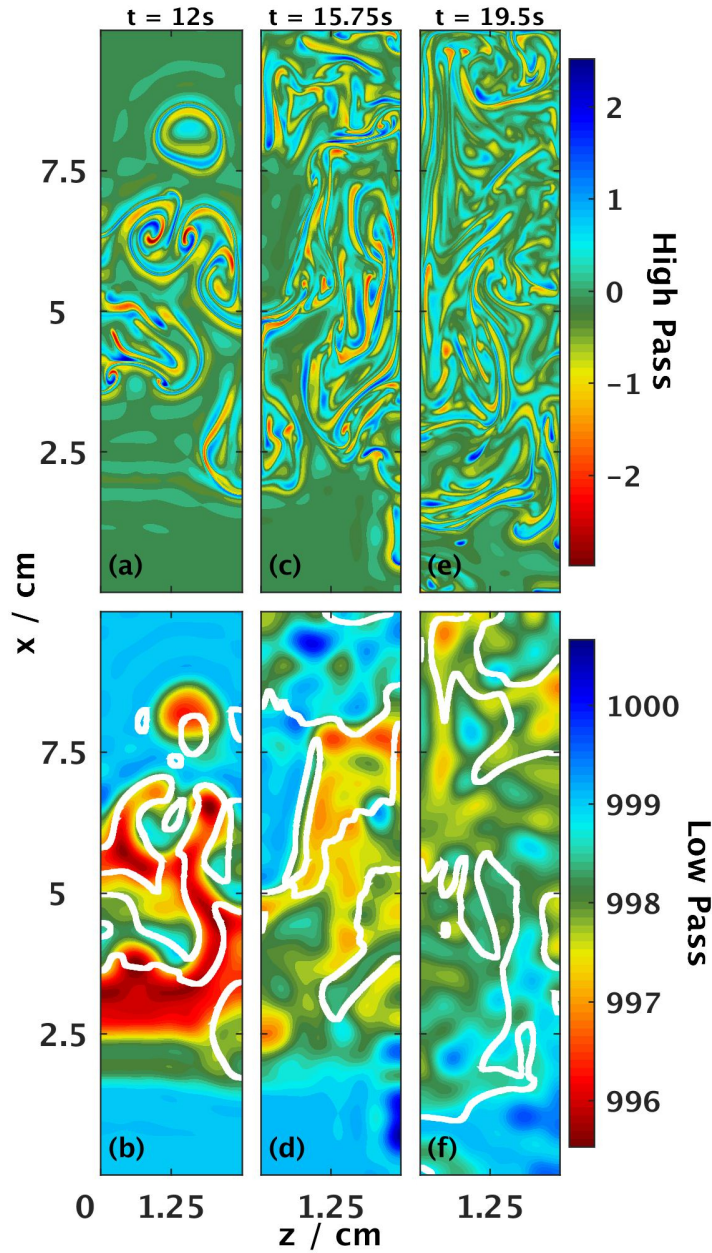
Figure 4.35: Filtered contours of density in the xz-plane along $y = 0.60\,\text{cm}$ at $t = 12\,\text{s}$, $15.75\,\text{s}$, and $19.5\,\text{s}$, with the high pass filter applied in the top row, and the low pass filter applied in the bottom row. The white lines indicate kinetic energy contours of $4 \times 10^{-5}\,\text{m}^2/\text{s}^2$. The colour bars indicate the density in kg/m^3.

121

2. In the 3D DNS of the three-layer double-diffusive RT instability, salt fingers along the lower interface were observed to form much slower than the RT instabilities along the upper interface. Several bubbles and spikes emerged from the upper pycnocline, with small-scale double-diffusive features inside. As in the gravity current simulations, the temperature and salinity fields displayed similar shapes, though there was significant smearing in the temperature field, while the salinity field maintained finer-scale features. There was strong similarity between the density fields and the salinity fields. The dominant KE features were much larger than the dominant density features, and reflected the shape of the RT instabilities.

3. On the scales examined in this simulation, an eddy diffusivity parameterization for the tracers was determined to be flawed, since the scales of the oscillating tracer gradients are much smaller than the scales of motion set by the RT instabilities.

4. Through spectral analysis, it was verified that the length scales of density were set by salinity, since the corresponding spectra agree well. Spectra of both fields showed contributions from significantly higher wave numbers than in the spectra of other fields examined. The KE spectra showed strong signals from very low wave numbers. In the spectra of horizontal slices, the KE appeared isotropic, while the density displayed different preferred wave numbers and direction that did not remain consistent between the height and time at which the spectra was examined. Density spectra along the vertical direction displayed a similar trend. Spectra of KE slices in the vertical direction showed a slight preference for higher wave number contribution in the horizontal direction.

5. Filtering of the double-diffusive features from the larger-scale density was briefly examined. The high wave number component of density was comprised of the sharp gradient features due to double-diffusion, while the low wave number component of density took the shape of more typical Rayleigh-Taylor flow. The low wave number component also contained regions where the density was higher (lower) than the initial maximum (minimum), which is only possible due to the effects of double-diffusion. It is speculated that this type of filtering may be useful in parameterizing double-diffusion as a subgrid-scale process in larger geophysical-scale LES models.

Chapter 5

Discussions and Future Work

In this thesis, high-resolution direct numerical simulation was used to model surface gravity currents that resulted in salt fingering, and a three-layer double-diffusive system was set up so that Rayleigh-Taylor instabilities developed. In order to adequately resolve the small-scale features characteristic of double-diffusion, the dimensions of the domain used were chosen to be even smaller than typical laboratory tanks, with relatively large numbers of grid points. Considering the computational expense involved in simulating such a small domain, double-diffusion is an entirely sub-grid scale process for many geophysical models [119]. As a result, the simulation data presented here may be useful in parameterizing larger-scale phenomena using large-eddy simulation (LES) analysis methods, such as the techniques using stratified turbulence DNS to calculate effective eddy viscosity presented by Khani and Waite [42]. Initial investigations into determining an eddy diffusivity parameterization in Chapter 4, however, were unsuccessful, suggesting that perhaps such a parameterization is not appropriate for the Rayleigh-Taylor simulation examined here, or that the approach may need to be altered. Taking the horizontal mean did not appear to adequately smooth the vertical tracer gradients and fluxes, giving local eddy diffusivities that rapidly oscillated with time. By examining a larger ensemble of these simulations, a more meaningful parameterization may be developed.

The results of these simulations have the potential to explain flow patterns that arise during thermohaline interleaving, where lateral intrusions are formed due to buoyancy differences at the interface of water masses of different temperature and salinity. Across these layers, the resulting thermohaline gradients may cause salt fingering, while shear is induced by the interleaving [59, 78, 75]. In numerical simulations, Kimura and Smyth [43] imposed fixed background shear, salinity and temperature profiles in a smoothed two-layer salt fingering system. They did so in order to encourage the growth of prominent salt

123

sheets, which may be reflective of the behaviour along the interfaces away from the intrusion fronts, where the interleaving layers and associated shear are already well-developed. In contrast, in the gravity current simulations presented here, buoyancy effects give way to a lateral intrusion, and any shear along the thermohaline interface is due to the resulting gravity current, and hence develops naturally. Therefore, these results may be valuable in the explanation of the early development of thermohaline intrusions. The three-layer simulation may have use in explaining the late-time behaviour of a warm, salty intrusion between cool, fresh layers, when shear effects are no longer important.

Provided that typical assumptions for suspended particles are satisfied by the system (e.g., the size of the particles is smaller than the smallest scale motion of the fluid [61]) and that the continuity hypothesis remains satisfied with the inclusion of particles, the model used in these simulations could be adapted to examine double-diffusive systems involving suspended sediment or other material. This would, however, involve the addition of a number of physical mechanisms to the model, such as settling velocities and particle-particle interactions (see Ozdemir et al. [63] and the references therein). The Boussinesq approximation would also need to be relaxed to allow for larger density differences.

Although the small-scale of the the simulations presented in this thesis would require an appropriate scaling for more useful comparisons with environmental flows, there is a more direct comparison to be made with laboratory or small-scale industrial processes. For example, consider a hypothetical flow where fluid containing one reactant is delivered into fluid containing a different reactant along a channel, similar to the gravity current setup used in Chapter 3. Based on the results of Chapter 3, to encourage more mixing of the reactants, the faster onset of instability in the no-slip cases can be exploited, with a sudden introduction of a solid upper boundary yielding a more rapid three-dimensionalization and local mixing. In the event one wanted to delay the mixing of the reactants, the results of Chapter 3 would suggest ensuring the upper boundary is made as close to free-slip as possible. A rather straightforward extension of this research would then be to investigate flows containing reactive tracers. SPINS would be well-suited to modelling these types of flows, since it was designed to be able to model up to ten tracer fields at a time. There have been a number of numerical [117, 14, 48] and experimental [16, 48] studies that examine the development of different buoyancy and diffusion-based instabilities along reactive interfaces on scales similar to the simulations presented here. Such experiments are commonly performed using Hele-Shaw cells, with two-dimensional simulations giving reasonable flow representations. It could therefore be beneficial to examine similar reactions with high-resolution 3D DNS, for a more detailed analysis of reactions in more standard containers.
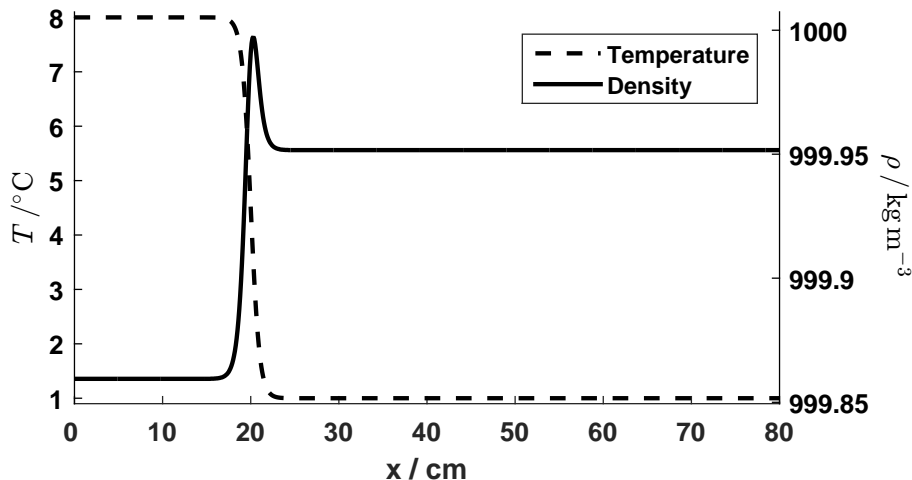
Figure 5.1: Initial horizontal temperature (dashed line) and density (solid line) distributions for the gravity current presented in Fig. 5.3.

Future Work: Flows near the Density Maximum

In Chapter 2, it was noted that the density of water behaves non-monotonically with temperature, reaching a maximum at 3.98°C [24]. Although the simulations presented in the previous chapters occur in a regime where the density changes monotonically with temperature, the use of equation (2.3) allows for simulations of colder flows that behave differently than those that use a linear equation of state. In this section, simulations of flows with temperatures in the non-monotonic regime are examined, as precursors to possible future work that builds on the results examined in detail in this thesis.

As a preliminary investigation, a fresh gravity current with an initial horizontal temperature distribution defined by equation 3.1, with $T_0 = 1\,°\text{C}$, $\Delta T = 7\,°\text{C}$, and $\Delta x = 1\,\text{cm}$ was considered. This results in a layer of lighter, $8\,°\text{C}$ fluid to the left of x_0, and heavier, $1\,°\text{C}$ fluid to the right. The temperature distribution as a function of horizontal position x is given by the dashed line in Fig. 5.1, with $x_0 = 20\,\text{cm}$. The resulting density profile has two distinct regions of constant density, to the left of x_0, where $\rho = 999.86\,\text{kg/m}^3$, and to the right of x_0, where $\rho = 999.95\,\text{kg/m}^3$. However, there is a local density maximum of $\rho = 1000\,\text{kg/m}^3$ at $x = 20.3\,\text{cm}$, where $\Delta T = 3.53\,°\text{C}$ (the temperature value which gives a density maximum for fresh water as defined by equation (2.3)). Two simulations were performed, one with a lower volume current ($x_0 = 10\,\text{cm}$, Fig. 5.2), and
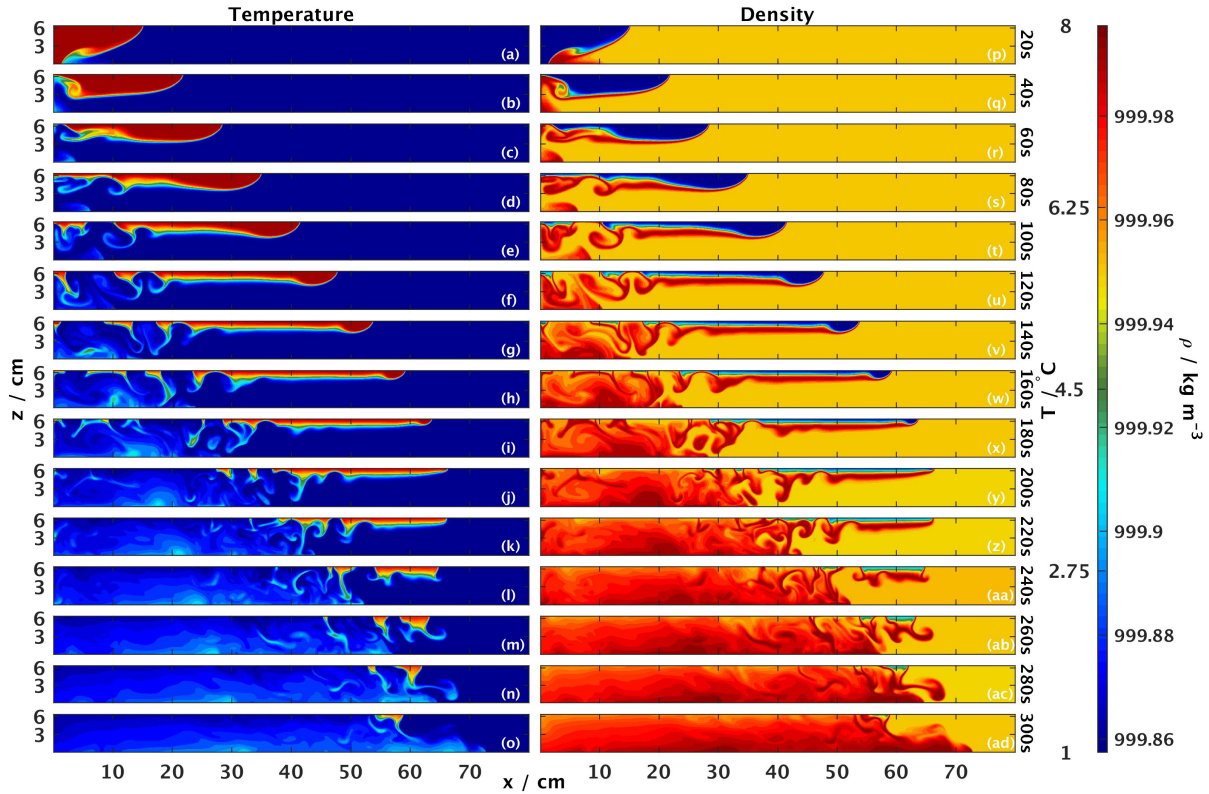
Figure 5.2: Temperature ((a)-(o)) and density ((p)-(ad)) contours for the smaller temperature-only gravity current ($x_0 = 10\,\mathrm{cm}$) from $t = 20\,\mathrm{s}$ to $300\,\mathrm{s}$ along $y = 3.17\,\mathrm{cm}$. The colour bar indicates the density in $\mathrm{kg/m^3}$.

one with a larger volume current ($x_0 = 20\,\mathrm{cm}$, Fig. 5.3). The domain in both cases was $80\,\mathrm{cm} \times 6.4\,\mathrm{cm} \times 6.4\,\mathrm{cm}$, on a $1024 \times 96 \times 96$ grid, with free-slip boundaries in all directions. Additionally, the kinematic viscosity and thermal diffusivity were set to $\nu = 10^{-6}\,\mathrm{m^2/s}$ and $\kappa_T = 1.7 \times 10^{-7}\,\mathrm{m^2/s}$.

The resulting currents display head shapes similar to the free-slip currents presented in Chapter 3. Because of the much smaller density difference between the two layers, these currents travel much more slowly than the double-diffusive currents. In both cases, there is a thin layer of high density between the current and the surrounding fluid. At $t = 40\,\mathrm{s}$, both currents have formed billows towards the back. Both currents then start to exhibit a fingering-like mechanism near the back of the current as the higher density fluid

126
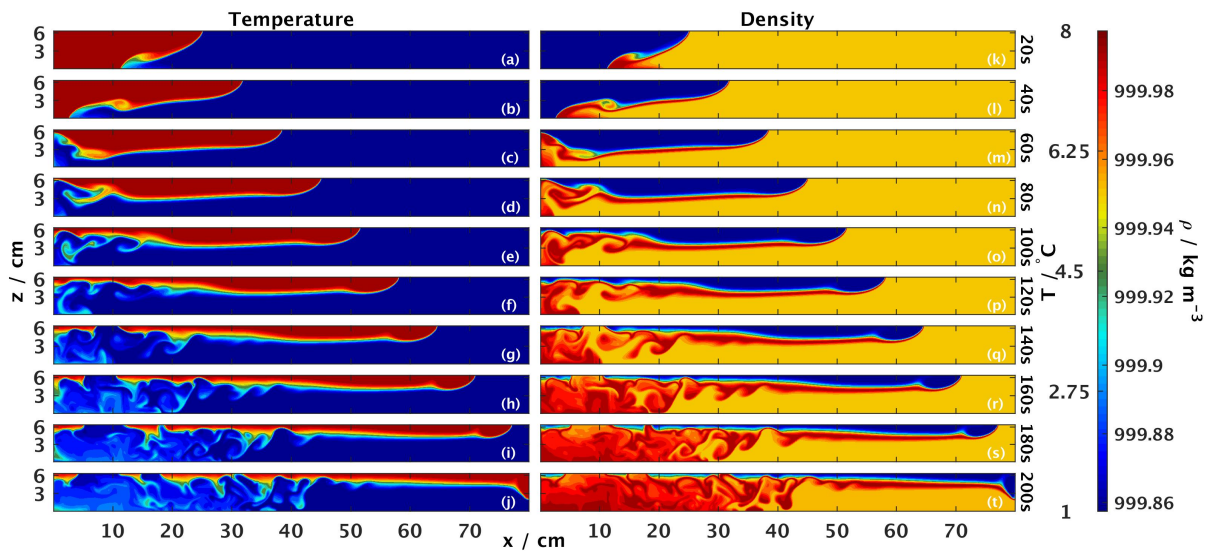
Figure 5.3: Temperature ((a)-(j)) and density ((k)-(t)) contours for the larger temperature-only gravity current ($x_0 = 20$ cm) from $t = 20$ s to 200 s along $y = 3.17$ cm. The colour bar indicates the density in kg/m^3.

begins to sink out, while the current bellies and heads stay relatively smooth. The lower volume current loses a significant portion of its mass via this mechanism, which completely destroys the surface current. The accumulated mass along the bottom of the domain is heavier than the surrounding fluid, forming a gravity current along the bottom. The larger current retains enough of its mass that it manages to reach the right-hand wall, although it becomes progressively thinner as it travels the length of the domain. The head and belly of the gravity currents are mostly two-dimensional during the flows, as was the case with the free-slip double-diffusive currents. Any three-dimensionalization occurs at the back of the currents, as presented in Fig. 5.4. The high density finger-like structures that trail from the back of the current are initially two-dimensional, but separate into three-dimensional features.

The process through which to water masses of similar densities combine to give a mass of higher density is known as cabbeling [4]. Cabbeling is responsible for the formation of thermal bars in lakes, where warmer water from the shallower edges or river inflows meet the colder water of the inner regions of lakes, resulting in sinking plumes of denser water [30]. As with the double-diffusive simulations presented in this thesis, the scales of the simulations discussed in this section are much smaller than limnological scales. There is, however, potential for these simulations to help quantify the distance travelled by the denser underflow, which would have repercussions for understanding nutrient distribution in lakes.

A possible future direction for this work would be to examine double-diffusion in this temperature regime, are it is possible for density increases to occur due to the nonlinearity with respect to temperature and due to double-diffusive effects. It may also be worth examining systems in which both active tracers behave nonlinearly. Ruddick and Shirtcliffe [77] provide a number of empirically determined equations of state that are nonlinear in heat, salt, and sugar.
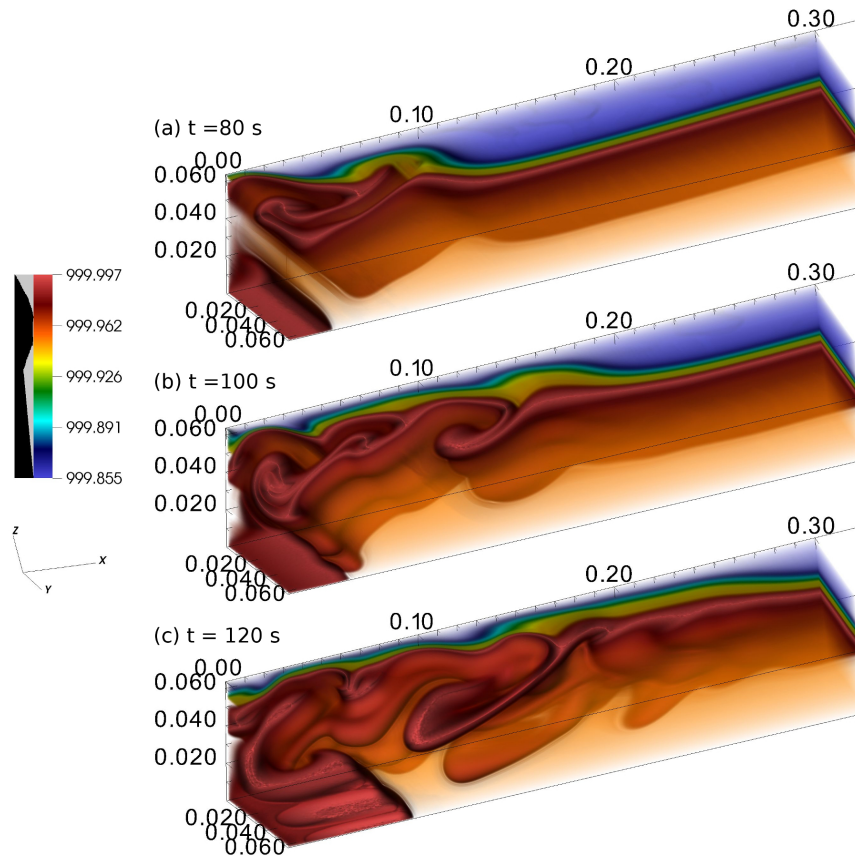
Figure 5.4: Density volume plots of the back of the larger temperature-only gravity current from $x = 0$ to $x = 30$ cm. The colour bar indicates the density in kg/m^3.

References

[1] VisIt User's Manual. Technical report, 2005.

[2] M. H. Alford and R. Pinkel. Patterns of Turbulent and Double-Diffusive Phenomena: Observations from a Rapid-Profiling Microconductivity Probe. *Journal of Physical Oceanography*, 30(5):833–854, 2000.

[3] M. J. Andrews and S. B. Dalziel. Small Atwood number Rayleigh-Taylor experiments. *Philosophical Transactions of the Royal Society A: Mathematical, Physical and Engineering Sciences*, 368(1916):1663–1679, 2010.

[4] T. Beer. *Environmental Oceanography*. CRC Marine Science. Taylor & Francis, 2nd edition, 1996.

[5] T. B. Benjamin. Gravity currents and related phenomena. *Journal of Fluid Mechanics*, 31(2):209–248, 1968.

[6] R. W. Bilger and R. W. Dibble. Differential Molecular Diffusion Effects in Turbulent Mixing. *Combustion Science and Technology*, 28(3-4):161–172, 1982.

[7] R. E. Britter and J. E. Simpson. Experiments on the dynamics of a gravity current head. *Journal of Fluid Mechanics*, 88:223, 1978.

[8] D. Brydon, S. Sun, and R. Bleck. A new approximation of the equation of state for seawater, suitable for numerical ocean models. *Journal of Geophysical Research*, 104 (C1):2156–2202, 1999.

[9] P. Burns and E. Meiburg. Sediment-laden fresh water above salt water: linear stability analysis. *Journal of Fluid Mechanics*, 691:279–314, 2012.

[10] P. Burns and E. Meiburg. Sediment-laden fresh water above salt water: nonlinear simulations. *Journal of Fluid Mechanics*, 762:156–195, 2015.

[11] J. R. Carpenter, T. Sommer, and A. Wüest. Simulations of a double-diffusive interface in the diffusive convection regime. *Journal of Fluid Mechanics*, 711:411–436, 2012.

[12] H. Childs, E. Brugger, B. Whitlock, J. Meredith, S. Ahern, D. Pugmire, K. Biagas, M. Miller, C. Harrison, G. H. Weber, H. Krishnan, T. Fogal, A. Sanderson, C. Garth, E. W. Bethel, D. Camp, O. Rübel, M. Durant, J. M. Favre, and P. Navrátil. VisIt: An End-User Tool For Visualizing and Analyzing Very Large Data. In *High Performance Visualization–Enabling Extreme-Scale Scientific Insight*, pages 357–372. CRC Press, 2012.

[13] S. Davarpanah Jazi and M. G. Wells. Enhanced sedimentation beneath particle-laden flows in lakes and the ocean due to double-diffusive convection. *Geophysical Research Letters*, 43(20):10883–10890, 2016.

[14] J. D'Hernoncourt, J. H. Merkin, and A. De Wit. Interaction between buoyancy and diffusion-driven instabilities of propagating autocatalytic reaction fronts. II. Nonlinear simulations. *Journal of Chemical Physics*, 130(11), 2009.

[15] C. Eckart. An analysis of the stirring and mixing processes in incompressible fluids. *Journal of Marine Research*, 7(3):265–275, 1948.

[16] K. Eckert and A. Grahn. Plume and finger regimes driven by an exothermic interfacial reaction. *Physical Review Letters*, 82(22):4436–4439, 1999.

[17] A. J. Elliott, M. R. Howe, and R. I. Tait. The lateral coherence of a system of thermo-haline layers in the deep ocean. *Deep-Sea Research*, 21:95–107, 1974.

[18] S. Emerson and J. Hedges. *Chemical Oceanography and the Marine Carbon Cycle*. Cambridge University Press, 2008.

[19] A. M. Fernandes and R. Krishnamurti. Salt finger fluxes in a laminar shear flow. *Journal of Fluid Mechanics*, 658:148–165, 2010.

[20] H. J. S. Fernando. Buoyancy transfer across a diffusive interface. *Journal of Fluid Mechanics*, 209(1989):1–34, 1989.

[21] A. E. Gargett and R. W. Schmitt. Observations of salt fingers in the central waters of the eastern North Pacific. *Journal of Geophysical Research*, 87(C10):8017, 1982.

[22] A. E. Gargett, W. J. Merryfield, and G. Holloway. Direct Numerical Simulation of Differential Scalar Diffusion in Three-Dimensional Stratified Turbulence. *Journal of Physical Oceanography*, 33:1758–1782, 2003.

[23] T. Green. The importance of double diffusion to the settling of suspended material. *Sedimentology*, 34(2):319–331, 1987.

[24] N. Greenwood and A. Earnshaw. *Chemistry of the Elements*. Elsevier, 2nd edition, 1997.

[25] M. C. Gregg and T. B. Sanford. Shear and turbulence in thermohaline staircases. *Deep Sea Research Part A, Oceanographic Research Papers*, 34(10):1689–1696, 1987.

[26] H. Hanazaki and K. Konishi. Differential diffusion in double-diffusive stratified turbulence. In J. Palma and A. S. Lopes, editors, *Advances in Turbulence XI: Proceedings of the 11th EUROMECH European Turbulance Conference, June 25-28, 2007 Porto, Portugal*, pages 615–617. Springer Berlin Heidelberg, Berlin, Heidelberg, 2007.

[27] C. Härtel, F. Carlsson, and M. Thunblom. Analysis and direct numerical simulation of the flow at a gravity-current head. Part 2. The lobe-and-cleft instability. *Journal of Fluid Mechanics*, 418:213–229, 2000.

[28] C. Härtel, E. Meiburg, and F. Necker. Analysis and direct numerical simulation of the flow at a gravity-current head. Part 1. Flow topology and front speed for slip and no-slip boundaries. *Journal of Fluid Mechanics*, 418:189–212, 2000.

[29] R. A. Hoare. Problems of Heat Transfer in Lake Vanda, a Density Stratified Antarctic Lake. *Nature*, 210:787 – 789, 1966.

[30] P. R. Holland, A. Kay, and V. Botte. A Numerical Study of the Dynamics of the Riverine Thermal Bar in a Deep Lake. *Environmental Fluid Mechanics*, 1(3):311–332, 2001.

[31] D. Houk and T. Green. Descent rates of suspension fingers. *Deep Sea Research*, 20: 757–761, 1973.

[32] D. C. J. D. Hoyal, M. I. Bursik, and J. F. Atkinson. The influence of diffusive convection on sedimentation from buoyant plumes. *Marine Geology*, 159(1-4):205–220, 1999.

[33] H. E. Huppert and P. C. Manins. Limiting conditions for salt-fingering at an interface. *Deep-Sea Research and Oceanographic Abstracts*, 20(4):315–323, 1973.

[34] D. M. Imboden. The Influence of Biogeochemical Processes on the Physics of Lakes. In *Physical Processes in Lakes and Oceans*, chapter 39, pages 591–612. American Geophysical Union, 2013.

[35] M. C. Ingham. *The Salinity Extrema of the World Ocean*. PhD thesis, Oregon State University, 1966.

[36] J. W. Jacobs and S. B. Dalziel. Rayleigh-Taylor instability in complex stratifications. *J. Fluid Mech.*, 542:251–279, 2005.

[37] W. S. Jevons. II. On the cirrous form of cloud. *Philosophical Magazine Series 4*, 14 (90):22–35, 1857.

[38] JSR-08-142. Data Analysis Challenges, 2008.

[39] E. Jurjen Kranenborg and H. A. Dijkstra. On the evolution of double-diffusive intrusions into a stably stratified liquid: a study of the layer merging process. *International Journal of Heat and Mass Transfer*, 41(18):2743–2756, 1998.

[40] Y. Kamotani, L. Wang, S. Ostrach, and H. Jiang. Experimental study of natural convection in shallow enclosures with horizontal temperature and concentration gradients. *International Journal of Heat and Mass Transfer*, 28(1):165–173, 1985.

[41] A. R. Kerstein, M. A. Cremer, and P. A. McMurtry. Scaling properties of differential molecular diffusion effects in turbulence. *Physics of Fluids*, 7(8):1999, 1995.

[42] S. Khani and M. L. Waite. Effective eddy viscosity in stratified turbulence. *Journal of Turbulence*, 14(7):49–70, 2013.

[43] S. Kimura and W. Smyth. Direct numerical simulation of salt sheets and turbulence in a double-diffusive shear layer. *Geophysical Research Letters*, 34(21):L21610, 2007.

[44] S. Kimura, W. Smyth, and E. Kunze. Turbulence in a Sheared, Salt-Fingering-Favorable Environment: Anisotropy and Effective Diffusivities. *Journal of Physical Oceanography*, 41(6):1144–1159, 2011.

[45] N. Konopliv and E. Meiburg. Double-diffusive lock-exchange gravity currents. *Journal of Fluid Mechanics*, 797:729–764, 2016.

[46] P. K. Kundu and I. M. Cohen. *Fluid Mechanics*. Academic Press, 2008.

[47] E. Kunze. Limits on growing, finite-length salt fingers: A Richardson number constraint. *Journal of Marine Research*, 45(3):533–556, 1987.

[48] L. Lemaigre, M. A. Budroni, L. A. Riolfo, P. Grosfils, and A. De Wit. Asymmetric Rayleigh-Taylor and double-diffusive fingers in reactive systems. *Physics of Fluids*, 25(1), 2013.

[49] D. J. Lewis. The Instability of Liquid Surfaces when Accelerated in a Direction Perpendicular to their Planes. II. *Proceedings of the Royal Society of London. Series A. Mathematical and Physical Sciences*, 202(1068):81 – 96, Jun 1950.

[50] P. F. Linden. Salt fingers in a steady shear flow. *Geophysical Fluid Dynamics*, 6(1): 1–27, 1974.

[51] P. F. Linden and T. G. L. Shirtcliffe. The diffusive interface in double-diffusive convection. *Journal of Fluid Mechanics*, 87(03):417, 1978.

[52] Lord Rayleigh. Investigation of the Character of the Equilibrium of an Incompressible Heavy Fluid of Variable Density. *Proceedings of the London Mathematical Society*, s1-14(1):170–177, Nov 1883.

[53] G. O. Marmorino. Intrusions and diffusive interfaces in a salt-finger staircase. *Deep Sea Research Part A, Oceanographic Research Papers*, 38(11):1431–1454, 1991.

[54] G. O. Marmorino, W. K. Brown, and W. D. Morris. Two-dimensional temperature structure in the C-SALT thermohaline staircase. *Deep Sea Research Part A, Oceanographic Research Papers*, 34(10):1667–1676, 1987.

[55] T. Maxworthy. Dynamics of Double-Diffusive Gravity Currents. *Journal of Fluid Mechanics*, 128:259–282, 1983.

[56] T. Maxworthy. The dynamics of sedimenting surface gravity currents. *Journal of Fluid Mechanics*, 392:27–44, 1999.

[57] T. J. McDougall and J. R. Taylor. Flux measurements across a finger interface at low values of the stability ratio. *Journal of Marine Research*, 42(1):1–14, 1984.

[58] W. J. Merryfield. Origin of Thermohaline Staircases. *Journal of Physical Oceanography*, 30(5):1046–1068, 2000.

[59] R. D. Mueller, W. D. Smyth, and B. Ruddick. Shear and convective turbulence in a model of thermohaline intrusions. *Journal of Physical Oceanography*, 37(10): 2534–2549, 2007.

[60] H. Nagashima and J. Yoshida. Numerical Experiments on Double Diffusively Induced Gravity Currents. In L. Oxley, editor, *MODSIM 1999 International Congress on Modelling and Simulation. Modelling and Simulation Society of Australia and New Zealand*, pages 243–248, 1999.

[61] F. Necker, C. Härtel, L. Kleiser, and E. Meiburg. High-resolution simulations of particle-driven gravity currents. *International Journal of Multiphase Flow*, 28:279–300, 2002.

[62] F. Necker, C. Härtel, L. Kleiser, and E. Meiburg. Mixing and dissipation in particle-driven gravity currents. *Journal of Fluid Mechanics*, 545:339–372, 2005.

[63] C. E. Ozdemir, T. J. Hsu, and S. Balachandar. A numerical investigation of lutocline dynamics and saturation of fine sediment in the oscillatory boundary layer. *Journal of Geophysical Research: Oceans*, 116(9):1–21, 2011.

[64] T. M. Özgökmen and O. E. Esenkov. Asymmetric salt fingers induced by a nonlinear equation of state. *Physics of Fluids*, 10(8):1882–1890, 1998.

[65] T. M. Özgökmen, O. E. Esenkov, and D. B. Olson. A numerical study of layer formation due to fingers in double-diffusive convection in a vertically-bounded domain. *Journal of Marine Research*, 56(2):463–487, 1998.

[66] J. D. Parsons and M. H. García. Enhanced Sediment Scavenging Due to Double-Diffusive Convection. *Journal of Sedimentary Research*, 70(1):47–52, 2000.

[67] J. D. Parsons, J. W. M. Bush, and J. P. M. Syvitski. Hyperpycnal plume formation from riverine outflows with small sediment concentrations. *Sedimentology*, 48(2): 465–478, 2001.

[68] J. Penney and M. Stastna. Direct numerical simulation of double-diffusive gravity currents. *Physics of Fluids*, 28:086602, 2016.

[69] S. A. Piacsek and J. Toomre. Nonlinear evolution and structure of salt fingers. In J. C. Nihoul, editor, *Marine Turbulence, Elsevier Oceanography Series*, volume 28, pages 193–219. Elsevier, New York, 1980.

[70] S. A. Piacsek, N. H. Brummel, and B. E. McDonald. Numerical experiments on thermohaline convective motions across interfaces of intrusions. In J. C. J. Nihoul and B. M. Jamart, editors, *Small-scale Turbulence and Mixing in the Ocean, Elsevier Oceanography Series*, volume 46, pages 503–516. Elsevier, New York, 1988.

[71] T. Radko. A mechanism for layer formation in a double-diffusive fluid. *Journal of Fluid Mechanics*, 497(2003):365–380, 2003.

[72] M. Rieutord and F. Espinosa Lara. Studying Stellar Rotation and Convection. *Studying Stellar Rotation and Convection*, 865:219–237, 2013.

[73] B. Ruddick. Laboratory studies of interleaving. *Progress in Oceanography*, 56(3-4): 529–547, 2003.

[74] B. Ruddick and A. E. Gargett. Oceanic double-diffusion: introduction. *Progress in Oceanography*, 56(3-4):381–393, 2003.

[75] B. Ruddick and O. Kerr. Oceanic thermohaline intrusions: theory. *Progress in Oceanography*, 56(3-4):483–497, 2003.

[76] B. Ruddick, D. Walsh, and N. Oakey. Variations in Apparent Mixing Efficiency in the North Atlantic Central Water. *Journal of Physical Oceanography*, 27:2589–2605, 1997.

[77] B. R. Ruddick and T. G. L. Shirtcliffe. Data for double diffusers: Physical properties of aqueous salt-sugar solutions. *Deep Sea Research Part A, Oceanographic Research Papers*, 26(7):775–787, 1979.

[78] B. R. Ruddick, O. M. Phillips, and J. S. Turner. A laboratory and quantitative model of finite-amplitude thermohaline intrusions. *Dynamics of Atmospheres and Oceans*, 30(2-4):71–99, 1999.

[79] R. Salmon. *Lectures on Geophysical Fluid Dynamics*. Oxford University Press, USA, 1998.

[80] B. Scheifele, R. Pawlowicz, T. Sommer, and A. Wüest. Double Diffusion in Saline Powell Lake, British Columbia. *Journal of Physical Oceanography*, 44(11):2893–2908, 2014.

[81] M. Schmid, A. Lorke, C. Dinkel, G. Tanyileke, and A. Wüest. Double-diffusive convection in Lake Nyos, Cameroon. *Deep-Sea Research Part I: Oceanographic Research Papers*, 51(8):1097–1111, 2004.

[82] M. Schmid, M. Busbridge, and A. Wüest. Double-diffusive convection in Lake Kivu. *Limnology and Oceanography*, 55(1):225–238, 2010.

[83] R. Schmitt. Double Diffusion in Oceanography. *Annual Review of Fluid Mechanics*, 26(1):255–285, 1994.

[84] R. W. Schmitt. Form of the Temperature-Salinity Relationship in the Central Water: Evidence for Double-Diffusive Mixing. *Journal of Physical Oceanography*, 11(7):1015–1026, 1981.

[85] R. W. Schmitt. The salt finger experiments of Jevons (1857) and Rayleigh (1880). *Journal of Physical Oceanography*, 25(1):8–17, 1995.

[86] R. W. Schmitt and D. L. Evans. An estimate of the vertical mixing due to salt fingers based on observations in the North Atlantic central water. *Journal of Geophysical Research*, 83 (C6)(8):2913–2919, 1978.

[87] R. W. Schmitt, H. Perkins, J. D. Boyd, and M. C. Stalcup. C-SALT: An investigation of the thermohaline staircase in the western tropical North Atlantic. *Deep Sea Research Part A, Oceanographic Research Papers*, 34(10):1655–1665, 1987.

[88] C. Y. Shen and G. Veronis. Numerical simulation of two-dimensional salt fingers. *Journal of Geophysical Research*, 102(C10):23131–23143, 1997.

[89] J. E. Simpson. Effects of the lower boundary on the head of a gravity current. *Journal of Fluid Mechanics*, 53(04):759–768, 1972.

[90] J. E. Simpson. Gravity Currents in the Laboratory, Atmosphere, and Ocean. *Annual Review of Fluid Mechanics*, 14:213–234, 1982.

[91] J. E. Simpson. *Gravity Currents: In the Environment and the Laboratory*. In the Environment and the Laboratory. Cambridge University Press, 1997.

[92] W. D. Smyth and S. Kimura. Mixing in a Moderately Sheared Salt-Fingering Layer. *Journal of Physical Oceanography*, 41(7):1364–1384, 2011.

[93] W. D. Smyth, J. D. Nash, and J. N. Moum. Differential Diffusion in Breaking Kelvin-Helmholtz Billows. *Journal of Physical Oceanography*, 35(6):1004–1022, 2005.

[94] L. St. Laurent and R. W. Schmitt. The Contribution of Salt Fingers to Vertical Mixing in the North Atlantic Tracer Release Experiment*. *Journal of Physical Oceanography*, 29(7):1404–1424, 1999.

[95] M. E. Stern. Lateral mixing of water masses. *Deep-Sea Research and Oceanographic Abstracts*, 14(6):747–753, 1967.

[96] M. E. Stern and J. S. Turner. Salt fingers and convecting layers. *Deep Sea Research and Oceanographic Abstracts*, 16(March):497–511, 1969.

[97] C. J. Subich, K. G. Lamb, and M. Stastna. Simulation of the Navier-Stokes equations in three dimensions with a spectral collocation method. *International Journal for Numerical Methods in Fluids*, 73:103–129, 2013.

[98] R. I. Tait and M. R. Howe. Thermohaline staircase. *Nature*, 231(5299):178–179, 1971.

[99] G. Taylor. The Instability of Liquid Surfaces when Accelerated in a Direction Perpendicular to their Planes. I. *Proceedings of the Royal Society of London. Series A, Mathematical and Physical Sciences*, 201(1065):192–196, 1950.

[100] H. Tennekes and J. L. Lumley. *A First Course in Turbulence*. MIT Press, 1972.

[101] S. Thangam and C. F. Chen. Salt-Finger convection in the surface discharge of heated saline jets. *Geophysical & Astrophysical Fluid Dynamics*, 18(1-2):111–146, 1981.

[102] M.-L. Timmermans, J. Toole, R. Krishfield, and P. Winsor. Ice-Tethered Profiler observations of the double-diffusive staircase in the Canada Basin thermocline. *Journal of Geophysical Research*, 113:1–10, 2008.

[103] J. S. Turner. The coupled turbulent transport of salt and heat across a sharp density interface. *International Journal of Heat and Mass Transfer*, 8(5):759–767, 1965.

[104] J. S. Turner. Salt fingers across a density interface. *Deep Sea Research and Oceanographic Abstracts*, 14(5):599–611, 1967.

[105] J. S. Turner. *Buoyancy effects in fluids*. Cambridge University Press, London, 1973.

[106] J. S. Turner. Double-diffusive intrusions into a density gradient. *Journal of Geophysical Research*, 83(C6):2887, 1978.

[107] J. S. Turner and C. F. Chen. Two-dimensional effects in double-diffusive convection. *Journal of Fluid Mechanics*, 63(3):577–592, 1974.

[108] T. von Kármán. The engineer grapples with nonlinear problems. *Bulletin of the American Mathematical Society*, 46(8):615–684, 1940.

[109] C. von Rohden, B. Boehrer, and J. Ilmberger. Evidence for double diffusion in temperate meromictic lakes. *Hydrology and Earth System Sciences*, 14(4):667–674, 2010.

[110] M. G. Wells. Interaction of salt finger convection with intermittent turbulence. *Journal of Geophysical Research*, 108(C3):1–12, 2003.

[111] M. G. Wells and R. W. Griffiths. Localized stirring in a field of salt-fingers. *Dynamics of Atmospheres and Oceans*, 35(4):327–350, 2002.

[112] M. G. Wells, R. W. Griffiths, and J. S. Turner. Generation of density fine structure by salt fingers in a spatially periodic shear. *Journal of Geophysical Research*, 106: 7027–7036, 2001.

[113] B. Whitlock, J. van Bethlehem, and H. Childs. VisIt Python Interface Manual, 2011.

[114] A. J. Williams. Salt fingers observed in the Mediterranean outflow. *Science*, 185: 941–943, 1974.

[115] A. J. Williams. Images of ocean microstructure. *Deep-Sea Research and Oceanographic Abstracts*, 22(12):811–829, 1975.

[116] J. C. Wyngaard. *Turbulence in the Atmosphere.* Cambridge University Press, 1st edition, 2010.

[117] J. Yang, A. D'Onofrio, S. Kalliadasis, and A. De Wit. Rayleigh-Taylor instability of reaction-diffusion acidity fronts. *Journal of Chemical Physics*, 117(20):9395–9408, 2002.

[118] P. K. Yeung and S. B. Pope. Differential diffusion of passive scalars in isotropic turbulence. *Physics of Fluids A: Fluid Dynamics*, 5(10):2467, 1993.

[119] J. Yoshida and H. Nagashima. Numerical experiments on salt-finger convection. *Progress in Oceanography*, 56(3-4):435–459, 2003.

[120] J. Yoshida and H. Nagashima. Numerical experiments on double-diffusive intrusions in the ocean and their relation to laboratory experiments. *Progress in Oceanography*, 56(3-4):549–557, 2003.

[121] J. Yoshida, H. Nagashima, and W.-J. Ma. A double diffusive lock-exchange flow with small density difference. *Fluid Dynamics Research*, 205(2):205–215, 1987.

[122] D. L. Youngs. Numerical simulation of turbulent mixing by Rayleigh-Taylor instability. *Physica D: Nonlinear Phenomena*, 12(1-3):32–44, 1984.